

A Study of Two-Prong Two-Photon Events at the Z^0 Resonance

Lee Anne Kowalski

Stanford Linear Accelerator Center
Stanford University
Stanford, CA 94309

SLAC-Report-731

Prepared for the Department of Energy
under contract number DE-AC03-76SF00515

Printed in the United States of America. Available from the National Technical Information Service, U.S. Department of Commerce, 5285 Port Royal Road, Springfield, VA 22161.

A STUDY OF TWO-PRONG TWO-PHOTON EVENTS
AT THE Z^0 RESONANCE

A DISSERTATION
SUBMITTED TO THE DEPARTMENT OF PHYSICS
AND THE COMMITTEE ON GRADUATE STUDIES
OF STANFORD UNIVERSITY
IN PARTIAL FULFILLMENT OF THE REQUIREMENTS
FOR THE DEGREE OF
DOCTOR OF PHILOSOPHY


By
Lee Anne Kowalski
September 1992

© Copyright 1992

by

Lee Anne Kowalski

I certify that I have read this thesis and that in my opinion it is fully adequate, in scope and in quality, as a dissertation for the degree of Doctor of Philosophy.



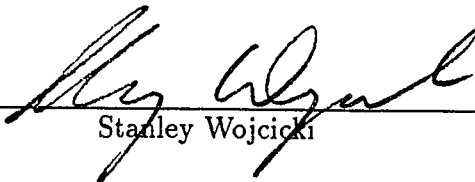
Martin Perl
(Principal Adviser)

I certify that I have read this thesis and that in my opinion it is fully adequate, in scope and in quality, as a dissertation for the degree of Doctor of Philosophy.



David Burke

I certify that I have read this thesis and that in my opinion it is fully adequate, in scope and in quality, as a dissertation for the degree of Doctor of Philosophy.



Stanley Wojcicki

Approved for the University Committee on Graduate Studies:



Judith I. Malster

Abstract

A study of electron-positron scattering leading to two electron-positron pairs via a two-photon interaction has been carried out at the Stanford Linear Accelerator Center (SLAC). The case where one pair is observed in the detector was investigated. These events were produced at the SLAC Linear Collider (SLC) operating in the center-of-mass energy range from 89.2 to 93.0 GeV. The data was collected using the Mark II detector.

Two-photon interactions are described by the theory of quantum electrodynamics (QED). Such processes can be a significant background to new particle searches; consequently, an understanding of their production is imperative. A deviation from the event rate predicted by QED might indicate the existence of new particles. The event rate may also be useful as a luminosity monitor during data collection.

The data sample from the Mark II is searched for events which have a features indicative of two-photon events. For comparison with theory, the Berends, Daverveldt, and Keiss Monte Carlo event generator is used to simulate events according to QED theory. The data is compared to the theoretical predictions. Given the low event statistics from the SLC data run, the results are consistent with the QED theoretical prediction. However, due to the low statistics, this measurement cannot be used to indicate non-deviation from QED predictions.

Acknowledgments

I thank my advisor, Martin Perl, for his support and encouragement during my years at SLAC. I also thank the Mark II collaboration. So many people in the collaboration inspired me with their enthusiasm and dedication, especially David Burke and Walt Innes. Special mention goes to Kathy O'Shaughnessy for putting up with my constant questions!

I also thank the members of the Drift Chamber Vertex Detector group for the valuable lessons in detector construction (and epoxy mixing!) they've given me. I am especially grateful to Charles Munger, Mike Hildreth, Max Dresden, and Ron Stickley for their sparkling wit and humor. Their conversations brightened those times when I couldn't stand to look at my computer screen!

As for those persons outside of SLAC who brightened and enlivened my years here at Stanford, you are many. Thanks to the Stanford Newman Choir, Menlo Players Guild, and Hoover for keeping my insanity level high. Thanks to my friends back home whose letters greatly entertained me. A very special thank you to David McCaleb, whose late-night discussions have kept me on track this last year.

I especially thank my dear friends Robin Wright and Dave Fernandes, without whom I would never have ventured into the wilds of high energy physics.

*I dedicate this thesis to my parents, whose love and support have been never ending:
to my father, who taught me to love science, and to my mother, who taught me to
love everything else.*

Contents

Abstract	iv
Acknowledgments	v
1 Introduction	1
2 Theory	4
2.1 Lepton production in e^+e^- collisions	4
2.1.1 Bhabha scattering	4
2.1.2 e^+e^- annihilation into lepton pairs	11
2.1.3 Two-photon production of leptons	15
2.1.4 $e^+e^- \rightarrow l^+l^-$ at the Z^0 mass	22
2.2 Hadron production in e^+e^- collisions	27
2.2.1 $e^+e^- \rightarrow hadrons$ via a virtual photon	27
2.2.2 $e^+e^- \rightarrow e^+e^-hadrons$ via two-photon interaction	32
2.2.3 $e^+e^- \rightarrow hadrons$ at the Z^0 mass	33
3 Experimental Apparatus	36
3.1 The SLAC Linear Collider	36
3.2 The Mark II Detector	39

3.2.1	Overview	39
3.2.2	Central Drift Chamber (CDC)	46
3.2.3	Time-of-Flight (TOF)	51
3.2.4	Luminosity Monitors	57
3.2.5	Trigger	61
3.2.6	Data Acquisition	64
3.3	Extraction Line Spectrometer	66
4	Kinematics of Two-Photon Reactions	67
4.1	The kinematics of $e^+e^- \rightarrow e^+e^-l^+l^-$	69
4.2	Cross sections (the general case)	72
4.3	The photon luminosity function	75
4.4	Approximations	75
4.5	QED cross sections	77
4.6	Experimental acceptances	79
5	Two-Photon Monte Carlo Simulation	82
5.1	Calculation of the two-photon cross section	82
5.2	Event generation	85
5.3	Monte Carlo signal generation	88
6	Event Selection and Analysis	93
6.1	Event topology	95
6.1.1	Charged track criteria	97
6.2	Particle identification	98
6.3	Results after selection cuts	101
6.4	Estimated backgrounds	104

6.4.1	Backgrounds from $e^+e^- \rightarrow Z^0$ processes	105
6.4.2	Backgrounds from two-photon processes	105
6.4.3	Backgrounds from beam-beam processes	107
6.5	Systematic errors	112
6.6	Monte Carlo event selection and comparison with data	116
6.7	Summary	116
7	Conclusions	120
A	Experimental Acceptance Function	122
	Bibliography	125

List of Tables

1	Theoretically calculated Bhabha cross sections for several center-of-mass energies. The cross section was integrated over angles between 0.015 and $\pi - 0.015$ radians. These cross sections do not include the Z^0 exchange diagrams.	9
2	The number of contributing diagrams in each of the six two-photon processes.	20
3	Theoretical cross sections $\sigma_{ee \rightarrow ee\mu\mu}$ and σ_o of the two-photon process $e^+e^- \rightarrow e^+e^-\mu^+\mu^-$ and the photon annihilation process $e^+e^- \rightarrow \mu^+\mu^-$, respectively, calculated at different center-of-mass energies. † includes electroweak contribution from the Z^0 boson.	23
4	Cross sections for $e^+e^- \rightarrow hadrons$, $\sigma_{ee \rightarrow ee\mu\mu}^{tot}$ and $\sigma_{ee \rightarrow ee\mu\mu}^{det}$ for different beam energies. At $E_{beam} = 0.5$ GeV (†), only the u and d quarks contribute. At $E_{beam} = 45.5$ GeV (‡), the Z^0 contribution is included.	32
5	Theoretical cross sections for $e^+e^- \rightarrow e^+e^-\pi^+\pi^-$ and $e^+e^- \rightarrow e^+e^-\mu^+\mu^-$ calculated at several beam energies.	34
6	Predicted detectable cross sections for pion and muon pair production from two-photon interactions, calculated for several beam energies using Equations 33 and 57.	34

7	The axial and vector couplings for each quark assuming $\sin^2 \theta_W = 0.232$.	35
8	SLC operational parameters.	38
9	Design parameters for the central drift chamber.	47
10	The total two-photon production cross section for the different leptons (e, μ, τ).	78
11	Statistics for Monte Carlo runs MC89 and MC90.	90
12	Integrated luminosity at each energy scan point for the 1989 data run.	94
13	The effect of selection cuts on the two data sets. The number of events in each row is the number that remains after that cut has been applied. For the 1990 data run, the numbers for the first two cuts are not available (N.A.).	102
14	Cross sections for two-photon processes as determined by Monte Carlo. Only the multiperipheral diagrams are taken into account.	106
15	The different contributions to the total systematic error.	115
16	The results of cuts C1-7 on Monte Carlo data.	117

List of Figures

1	The scattering and annihilation diagrams for Bhabha scattering. . . .	5
2	Center-of-mass kinematics for Bhabha scattering.	7
3	Differential cross section for Bhabha scattering, at a center-of-mass energy of 34 GeV,[After H.J.Behrend <i>et al.</i> , Phys. Lett. 103B (1981) 148.] The dots are experimental data; the curve is the QED cross section formula (18).	10
4	e^+e^- annihilation into two leptons (via photon exchange).	11
5	Kinematics for the process $e^+e^- \rightarrow l^+l^-$ in the center-of-mass frame. .	13
6	The total cross sections (in nb) for the processes $e^+e^- \rightarrow \mu^+\mu^-$ and $e^+e^- \rightarrow \tau^+\tau^-$ as a function of (relativistic) center-of-mass energies. [After D.P.Barber <i>et al.</i> , Phys. Rev. Lett. 43, (1979) 1915.] The dots are experimental data; the curves are the theoretical cross section formula (28).	14
7	The multiperipheral diagrams for $e^+e^- \rightarrow e^+e^-e^+e^-$. The last two diagrams may also be $e^+e^- \rightarrow e^+e^-\mu^+\mu^-$ and $e^+e^- \rightarrow e^+e^-\tau^+\tau^-$. (From Ref. [1]).	16
8	Diagram for photon-photon pair production of leptons.	17

9	The bremsstrahlung group of diagrams for $e^+e^- \rightarrow e^+e^-e^+e^-$. The diagrams in the last row may also be $e^+e^- \rightarrow e^+e^-\mu^+\mu^-$ or $e^+e^- \rightarrow e^+e^-\tau^+\tau^-$. (From Ref. [1]).	18
10	The annihilation group of diagrams for $e^+e^- \rightarrow e^+e^-e^+e^-$, as well as process (5) and (6). The diagrams in the last row may also be processes (2), (3), and (4). (From Ref. [1]).	19
11	The conversion group of diagrams for processes (1), (5), and (6). The first two diagrams may also contribute to processes (2),(3), and (4). (From Ref. [1]).	19
12	Diagrams contributing to $e^+e^- \rightarrow l^+l^-$ at the Z^0 resonance.	24
13	The two t-channel diagrams contributing to $e^+e^- \rightarrow e^+e^-$ at the Z^0 resonance.	25
14	Conceptual picture of hadron production from e^+e^- annihilation. . .	29
15	Ratio R as a function of E_{cm} . The sharp peaks correspond to the production of various resonances. (From Ref. [11]).	31
16	A schematic outline of the SLC.	37
17	The Mark II detector	40
18	Layout of the SSVD layers.	41
19	The drift chamber vertex detector.	42
20	Wire configuration for the DCVD.	43
21	Wire layout for the central drift chamber (CDC).	47
22	Measured (Data) and calculated (MC) CDC track reconstruction efficiency as a function of $\cos \theta$ [13].	49

23	Charged track multiplicity at large polar angles in the central drift chamber. [19] The data used (points) are from the 1989 run. The Monte Carlo simulation (line) is normalized to the total number of events.	49
24	Charged track multiplicity at low momentum in the central drift chamber. [19] The data used (points) are from the 1989 run. The Monte Carlo simulation (line) is normalized to the total number of events.	50
25	dE/dx values at PEP as a function of momentum.	52
26	Electron-pion separation at PEP.	52
27	Fit of the dE/dx theory curve to the SLC data. The solid curve is the fit obtained from the SLC data. The dotted line is the theory curve before the e^+e^- and $\mu^+\mu^-$ data were included in the fit. The data selected are: (a) protons, (b) minimum ionizing pions, (c) cosmic rays, (d) $\mu^+\mu^-$ pairs, and (e) e^+e^- pairs.	53
28	Time resolution for the Time of Flight system as measured at PEP.	55
29	The $\pi/K/p$ separation as measured at PEP using the TOF.	55
30	TOF resolution as measured at the SLC.	56
31	Schematic view of the SAM and Mini-SAM.	57
32	Side and front views of the Small Angle Monitor.	59
33	Geometry of the Mini-Small Angle Monitor.	60
34	Block diagram of the charged track trigger.	62
35	FASTBUS and CAMAC system of the Mark II data acquisition system.	65
36	Layout of the extraction line spectrometer system.	66
37	Quantum fluctuation of a photon into a pair of charged particles.	68
38	Box diagram for elastic $\gamma\gamma$ scattering.	68

39	Kinematics of the general two-photon process.	70
40	Feynman electron-photon vertex.	73
41	The multiperipheral diagrams.	84
42	The bremsstrahlung diagrams.	85
43	The conversion diagrams.	86
44	The annihilation diagrams.	86
45	Track multiplicity for MC89 events.	91
46	Track multiplicity for MC90 events.	91
47	Invariant pair mass distribution for MC89 events.	92
48	Invariant pair mass distribution for MC90 events.	92
49	Distribution in z (after r cut) of all 1989 two-track events.	96
50	Distribution in z (after r cut) of all 1990 two-track events. These are the events after cuts C2-C3 are applied.	97
51	Electron weights for 1989 data set. These are the weights after cuts C1-C6 are imposed.	99
52	Electron weights for 1990 data set. These are the weights after cuts C1-C6 are imposed.	100
53	Electron weights for MC89 events. These are the weights after cuts C1-C6 are imposed.	100
54	Electron weights for MC90 events. These are the weights after cuts C1-C6 are imposed.	101
55	A typical multiperipheral two-photon event seen in the Mark II detec- tor: (a) side view ($x-z$), (b) side view ($y-z$), (c) beam view ($x-y$). . .	103
56	Distribution in z of the event vertex for the 1989 data run. The plot is made after the particle identification cut, but with no cut in z . . .	107

57	Distribution in z of the event vertex for the 1990 data run. The plot is made after the particle identification cut, but with no cut in z . . .	108
58	Distribution of total p_t^2 for MC89 after all analysis cuts are made except for the z cut.	109
59	Two-dimensional plot of total p_t^2 and z for MC89 after all analysis cuts are made except for the z cut.	110
60	Distribution of total p_t^2 for the 1989 data run after all analysis cuts are made, except for the z cut.	110
61	Two-dimensional plot of total p_t^2 and z for the 1989 data run after all analysis cuts are made, except for the z cut.	111
62	Distribution of total p_t^2 for the 1990 data run after all analysis cuts are made, except for the z cut.	111
63	Two-dimensional plot of total p_t^2 and z for the 1990 data run after all analysis cuts are made except for the z cut.	112
64	Invariant pair mass distribution for 1989 data (points). Histogram is the theoretical prediction from Monte Carlo.	118
65	Invariant pair mass distribution for 1990 data (points). Histogram is the theoretical prediction from Monte Carlo.	118

Chapter 1

Introduction

Overview

This is a report on the production of two-photon events in e^+e^- collisions using the Mark II detector at the Stanford Linear Accelerator Center. In this experiment, the Stanford Linear Collider (SLC) ran at a center-of-mass energy of approximately 91 GeV. The process studied is:

$$e^+e^- \longrightarrow e^+e^-e^+e^-$$

in the case where only two leptons are observed in the detector while the colliding electron and positron are scattered through small angles and are not detected. The Feynman diagrams which account for most of the total cross section in this case are the multiperipheral, or t-channel, diagrams. Because two space-like virtual photons are emitted along the beam direction and interact, these events are also called two-photon processes.

The data are compared with QED predictions of order α^4 . A Monte Carlo program written by Berends *et al.* [1] is used to obtain the predictions for the above interactions.

Two-photon physics at the Z^0 resonance

The SLC was designed specifically to create the Z^0 boson by electron-positron annihilation. It is also important to study the two-photon processes which can occur. One reason is that two-photon processes can be a significant background to new particle searches. Suppose there exists a sequential lepton (L^\pm) such that [2]:

$$\begin{aligned} e^+e^- &\longrightarrow Z^0 \longrightarrow L^+ + L^- \\ L^+ &\longrightarrow l^+ + \nu_l + \bar{\nu}_L \\ L^- &\longrightarrow l^- + \bar{\nu}_l + \nu_L \end{aligned}$$

or a supersymmetric scalar lepton (\tilde{l}^\pm):

$$\begin{aligned} e^+e^- &\longrightarrow Z^0 \longrightarrow \tilde{l}^+ + \tilde{l}^- \\ \tilde{l}^+ &\longrightarrow l^+ + \tilde{\gamma} \\ \tilde{l}^- &\longrightarrow l^- + \tilde{\gamma} \end{aligned}$$

for masses

$$\begin{aligned} m_L &\gg m_l, \quad m_L \approx m_{\nu_L} \\ m_{\tilde{l}} &\gg m_l, \quad m_{\tilde{l}} \approx m_{\tilde{\gamma}} \end{aligned}$$

where l denotes an e or μ , ν is a neutrino, and $\tilde{\gamma}$ is a photino. If $m_L - m_{\nu_L}$ or $m_{\tilde{l}} - m_{\tilde{\gamma}}$ is small, ($\approx 1 \text{ GeV}/c^2$), these events appear as two leptons with low energies. Thus,

two-photon processes of this type can be a troublesome background for new particle searches unless the cross-sections are known exactly.

Two-photon events may also be used to measure the luminosity, if the cross section and the detector acceptance is known, and the detection rates are reasonable. The two-photon event count would provide a measurement of the luminosity independent of Bhabha scattering measurements. It is also important to study two-photon events at high center-of-mass energies as an investigation of QED at these energies.

In the past, the two-photon leptonic reaction $e^+e^- \rightarrow e^+e^-e^+e^-$ has been found to be in excellent agreement with the QED prediction, for energies in the range of 14–41 GeV [3, 38]. In a search for excited leptons, the AMY collaboration also found agreement with QED up to an energy of 56 GeV [4]. Unfortunately, because of the limited integrated luminosities of the Mark II data runs (19.3 nb⁻¹ for 1989 and 10.1 nb⁻¹ for 1990), the measurement here cannot improve on previous results.

Thesis outline

Chapter 2 describes the general theory of electron-positron interactions. Chapter 3 describes the SLC and the Mark II detector. Chapter 4 describes the theory of two-photon interactions in detail and the Monte Carlo program for simulating these interactions. Chapter 5 lists the parameters used in the Monte Carlo for this analysis and presents the Monte Carlo results. Chapter 6 compares the data with the Monte Carlo predictions, and the conclusions are discussed in Chapter 7.

Chapter 2

Theory

2.1 Lepton production in e^+e^- collisions

In this section, cross sections for lepton production in e^+e^- collisions are presented and discussed. A working knowledge of Feynman rules for calculating cross sections in QED will be assumed. These rules may be found in Appendix B of Ref. [5].

2.1.1 Bhabha scattering

The process

$$e^+(\mathbf{p}_1) + e^-(\mathbf{p}_2) \longrightarrow e^+(\mathbf{p}'_1) + e^-(\mathbf{p}'_2) \quad (1)$$

is called *Bhabha* scattering. The two lowest order diagrams contributing to Bhabha scattering are shown in Figure 1. The one on the left is called the *t-channel* diagram; the other is the *s-channel* diagram. The Feynman amplitude for this process is simply $\mathcal{M} = \mathcal{M}_t + \mathcal{M}_s$ where \mathcal{M}_t and \mathcal{M}_s correspond to the t-channel and s-channel diagrams

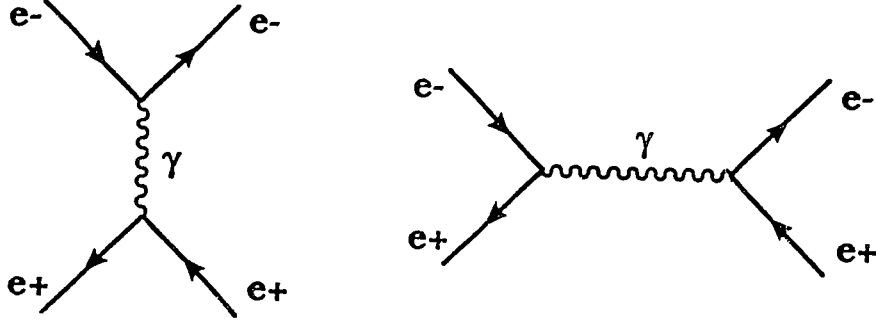


Figure 1: The scattering and annihilation diagrams for Bhabha scattering.

respectively. The full expressions for these two matrix elements are

$$\mathcal{M}_t = -ie^2[\bar{u}(p_2')\gamma_\alpha u(p_2)]\frac{1}{(p_1 - p_1')^2}[\bar{v}(p_1)\gamma^\alpha v(p_1')] \quad (2)$$

$$\mathcal{M}_s = ie^2[\bar{u}(p_2')\gamma_\alpha v(p_1')]\frac{1}{(p_1 + p_2)^2}[\bar{v}(p_1)\gamma^\alpha u(p_2)]. \quad (3)$$

The $u(p)$ and the $v(p)$ are the momentum-space spinors for a free electron and free positron respectively, with momentum p . The denominators of these matrix elements come from the photon propagator; according to the Feynman rules, each photon gives a factor $\frac{1}{q^2}$, where q is the photon four-momentum. In these expressions, the spin indices on the electron and positron spinors have been suppressed.

Following the Feynman rules for calculating cross sections (see Ref. [6]) gives

$$\left(\frac{d\sigma}{d\Omega}\right) = \frac{m^4\hbar^2c^2}{16\pi^2E^2}(X_{tt} + X_{ss} + X_{ts} + X_{ts}^*), \quad (4)$$

where

$$X_{tt} = \frac{1}{4} \sum_{\text{spins}} |\mathcal{M}_t|^2 \quad (5)$$

$$X_{ss} = \frac{1}{4} \sum_{\text{spins}} |\mathcal{M}_s|^2 \quad (6)$$

$$X_{ts} = \frac{1}{4} \sum_{\text{spins}} \mathcal{M}_t \mathcal{M}_s^*, \quad (7)$$

with the sums running over the spins of all four fermions. Using the energy projection operators and trace identities found in Ref. [5], the first term in the cross section becomes

$$X_{tt} = \frac{e^4}{2m^4[(p_1 - p'_1)^2]^2} (p_1 p_2)(p'_1 p'_2) + (p_1 p'_2)(p_2 p'_1) + O(E^2 m^2), \quad (8)$$

where $m \equiv m_e$, and E is the center-of-mass energy. The second term becomes

$$X_{ss} = \frac{e^4}{2m^4[(p_1 + p_2)^2]^2} (p_1 p'_1)(p_2 p'_2) + (p_1 p'_2)(p_2 p'_1 - 1) + O(E^2 m^2). \quad (9)$$

The interference term X_{ts} becomes

$$X_{ts} = \frac{e^4}{2m^4(p_1 - p'_1)^2(p_1 + p_2)^2} [(p_1 p'_2)(p_2 p'_1) + O(E^2 m^2)]. \quad (10)$$

Because X_{ts} is real, $X_{ts} = X_{ts}^*$. As written above, these terms are valid in any frame of reference. For simplicity, they can be evaluated in the center-of-mass frame. In experiments involving colliding beams of electrons and positrons at equal beam energies, this is the same as the laboratory frame. Figure 2 shows the kinematics in the center-of-mass frame. In this frame, we have

$$p_1 p'_1 = p_2 p'_2 = E^2 - p p' \cos \theta, \quad p_1 p'_2 = p_2 p'_1 = E^2 + p p' \cos \theta \quad (11)$$

$$p_1 p_2 = E^2 + p^2 \quad p'_1 p'_2 = E^2 + p'^2 \quad (12)$$

$$(p_1 + p_2)^2 = 4E^2 \quad (13)$$

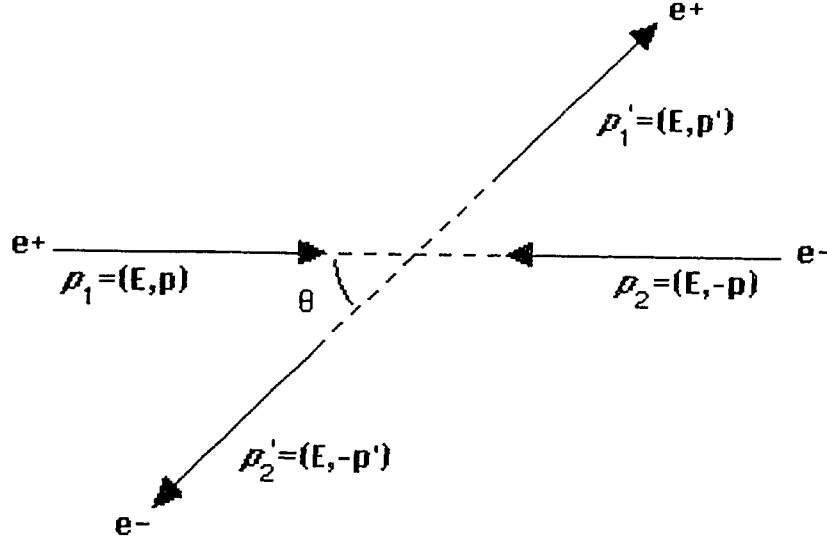


Figure 2: Center-of-mass kinematics for Bhabha scattering.

with

$$p \equiv |p|, \quad p' \equiv |p'|. \quad (14)$$

Also, for $E \gg m_e$, p is approximately equal to E , and terms $O(E^2 m^2)$ can be dropped.

The four matrix terms then become

$$X_{tt} = \frac{e^4}{8m^4 \sin^4(\frac{\theta}{2})} [1 + \cos^4 \frac{\theta}{2}] \quad (15)$$

$$X_{ss} = \frac{e^4}{16m^4} [1 + \cos^2 \theta] \quad (16)$$

$$X_{ts} = X_{ts}^* = \frac{-e^4}{8m^4 \sin^2(\frac{\theta}{2})} [\cos^4 \frac{\theta}{2}]. \quad (17)$$

Substituting these into the expression for $\frac{d\sigma}{d\Omega}$, results in

$$\frac{d\sigma}{d\Omega} = \frac{\alpha^2 \hbar^2 c^2}{2s} \left[\frac{1 + \cos^4(\theta/2)}{\sin^4(\theta/2)} + \frac{1 + \cos^2 \theta}{2} - \frac{2 \cos^4(\theta/2)}{\sin^2(\theta/2)} \right] \quad (18)$$

where s is the Mandelstam variable, $s = (2E)^2$.

The first term in this cross section comes from the t-channel diagram (a) in Figure 1. The second term comes from the s-channel diagram, and the third term arises from the interference between the two diagrams. At small angles, the t-channel term dominates, and the differential cross section becomes infinite. This is a consequence of the massless photon. If the photon had a mass ϵ , the $\frac{1}{(p_1 - p'_1)^2}$ term in \mathcal{M}_t would instead be $\frac{1}{(p_1 - p'_1)^2 + i\epsilon}$. The four-momentum of the photon is $q^2 \equiv (p_1 - p'_1)^2$. As listed in the kinematical equations above, in the center-of-mass frame, $q^2 = (p_1 - p'_1)^2 = 2p^2(\cos\theta - 1)$; therefore, $q^2 \rightarrow 0$ implies $\theta \rightarrow 0$. If the photon had a small mass, then \mathcal{M}_t would not diverge as q^2 approached zero. However, because the photon has zero mass, the amplitude from the photon exchange term diverges, and the total cross section ($\sigma = \int \frac{d\sigma}{d\Omega} d\Omega$) blows up.

In order to evaluate the total cross section, the differential cross section must be integrated between chosen angular cuts. The Mark II detector at the SLC had monitors that would detect tracks from Bhabha events down to $\theta = 15$ mrad on either side of the interaction point. Integrating the bracketed piece in Equation 18 over this angular region gives for the total cross section

$$\sigma = \frac{\alpha^2 \hbar^2 c^2}{2s} \times [(2\pi) \times (7.1 \times 10^4)]. \quad (19)$$

In “natural” units, $\hbar = c = 1$, $\alpha = \frac{1}{137}$, and this cross section becomes

$$\sigma = \frac{4.625 \times 10^6}{s(\text{GeV}^2)} \text{nanobarns}. \quad (20)$$

These total cross sections do not include the electroweak interference effects from Z^0 boson exchange. Using this cross section as a “typical” value, Table 1 lists the total Bhabha cross section for several energies between $\theta = 0.015$ and $\pi - 0.015$ radians. Figure 3 shows the angular distribution of the differential cross section at center-of-mass energy 34 GeV.

	E_{cm} (GeV)				
	5	10	50	91	200
s (GeV ²)	25	100	2500	8,281	40,000
σ ($\times 10^4$ nb)	185	46	1.85	0.56	0.116

Table 1: Theoretically calculated Bhabha cross sections for several center-of-mass energies. The cross section was integrated over angles between 0.015 and $\pi - 0.015$ radians. These cross sections do not include the Z^0 exchange diagrams.

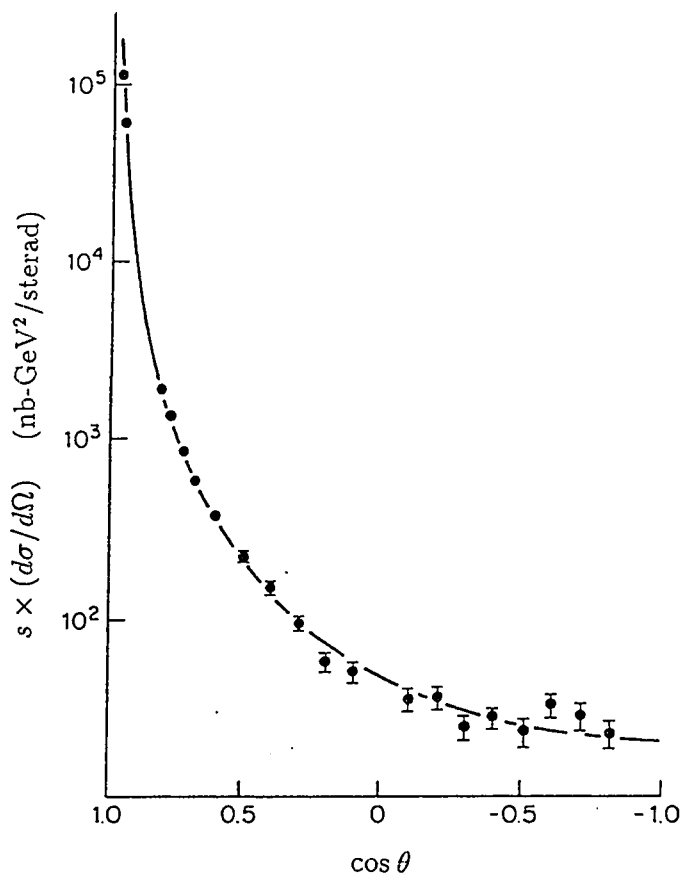


Figure 3: Differential cross section for Bhabha scattering, at a center-of-mass energy of 34 GeV, [After H.J.Behrend *et al.*, Phys. Lett. 103B (1981) 148.] The dots are experimental data; the curve is the QED cross section formula (18).

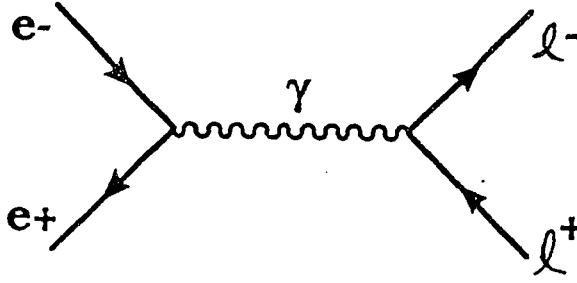


Figure 4: e^+e^- annihilation into two leptons (via photon exchange).

2.1.2 e^+e^- annihilation into lepton pairs

The three possible processes are:

$$e^+e^- \longrightarrow e^+e^-$$

$$e^+e^- \longrightarrow \mu^+\mu^-$$

$$e^+e^- \longrightarrow \tau^+\tau^-$$

The first process was discussed in Section 2.1.1. For the general process

$$e^+(p_1) + e^-(p_2) \longrightarrow l^+(p'_1) + l^-(p'_2) \quad (21)$$

where $l = \mu, \tau$, the leading order diagram is the annihilation (s-channel) diagram, shown in Figure 4. Its Feynman amplitude is \mathcal{M} , where

$$\mathcal{M} = ie^2 [\bar{u}(p'_2) \gamma_\alpha v(p'_1)]_{(l)} \frac{1}{(p_1 + p_2)^2} [\bar{v}(p_1) \gamma^\alpha u(p_2)]_{(e)}. \quad (22)$$

The labels (*l*) and (*e*) refer to leptons and electrons. Following the Feynman rules for calculating cross sections (see Ref. [6]) gives

$$\left(\frac{d\sigma}{d\Omega}\right) = \frac{m^4 \hbar^2 c^2}{16\pi^2 E^2} X \quad (23)$$

where

$$X = \frac{1}{4} \sum_{\text{spins}} |\mathcal{M}|^2. \quad (24)$$

Using the energy projection operator and trace identities from Ref. [6], one gets

$$X = \frac{e^4}{2m_e^2 m_l^2 [(p_1 + p_2)^2]^2} \{ (p_1 p'_1)(p_2 p'_2) + (p_1 p'_2)(p_2 p'_1) + m_e^2 (p'_1 p'_2) + m_l^2 (p_1 p_2) + 2m_e^2 m_l^2 \}. \quad (25)$$

Again, this formula is valid in any reference frame. As in Section 2.1.1, X may be evaluated in the center-of-mass frame. Figure 5 depicts the kinematics for this process in the center-of-mass frame. In this frame, the kinematic variables become

$$\begin{aligned} p_1 p'_1 = p_2 p'_2 &= E^2 - pp' \cos \theta, & p_1 p'_2 = p_2 p'_1 &= E^2 + pp' \cos \theta \\ p_1 p_2 &= E^2 + p^2 & p'_1 p'_2 &= E^2 + p'^2 \\ (p_1 + p_2)^2 &= 4E^2 \end{aligned}$$

with

$$p \equiv |\mathbf{p}|, \quad p' \equiv |\mathbf{p}'|.$$

Also, for $E \geq m_\mu \approx 207m_e$, p is approximately equal to E , and terms $O(m_e^2)$ are dropped. Making the appropriate substitutions, the differential cross section becomes

$$\frac{d\sigma}{d\Omega} = \frac{\alpha^2 \hbar^2 c^2}{4s} \beta [1 + \cos^2 \theta + (1 - \beta^2) \sin^2 \theta] \quad (26)$$

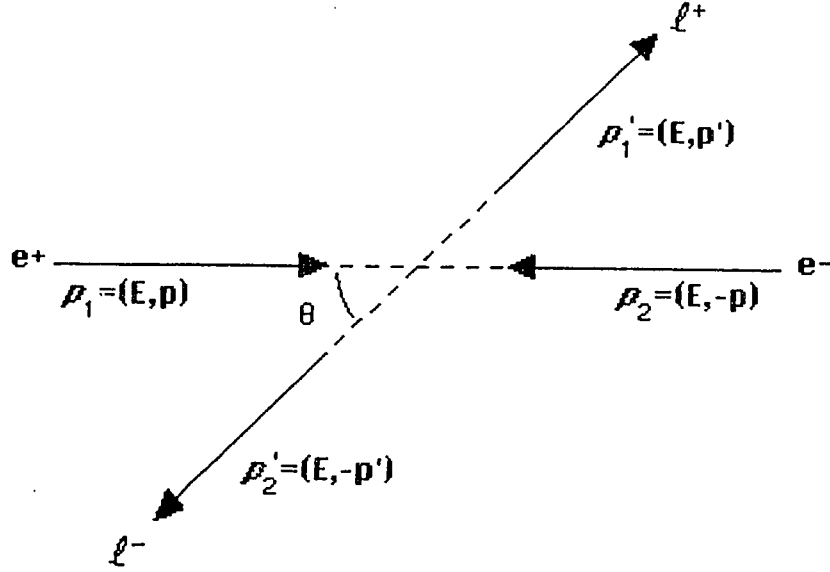


Figure 5: Kinematics for the process $e^+e^- \rightarrow l^+l^-$ in the center-of-mass frame.

where $s = E_{cm}^2$, β is the velocity of the lepton, and $E = \frac{m_l}{\sqrt{1-\beta^2}}$. Integrating over all angles gives the total cross section

$$\sigma = \frac{4\pi\alpha^2\hbar^2c^2}{3s} \frac{\beta(3-\beta^2)}{2}. \quad (27)$$

Both the differential cross section and the total cross section are always finite. Also, as the energy increases, the cross section decreases. For $E \gg m_l$, the differential and total cross sections become

$$\begin{aligned} \frac{d\sigma}{d\Omega}_{E \gg m_l} &= \frac{\alpha^2\hbar^2c^2}{4s}(1 + \cos^2\theta) \\ \sigma_{E \gg m_l} &= \frac{4\pi\alpha^2\hbar^2c^2}{3s}. \end{aligned} \quad (28)$$

These are the cross sections excluding electroweak corrections (i.e., Z^0 boson exchange). Therefore, the total cross section has a $1/E^2$ dependence at high energies (below the mass of the Z^0 boson). In “natural” units ($\hbar = c = 1$, $\alpha = \frac{1}{137}$), this cross

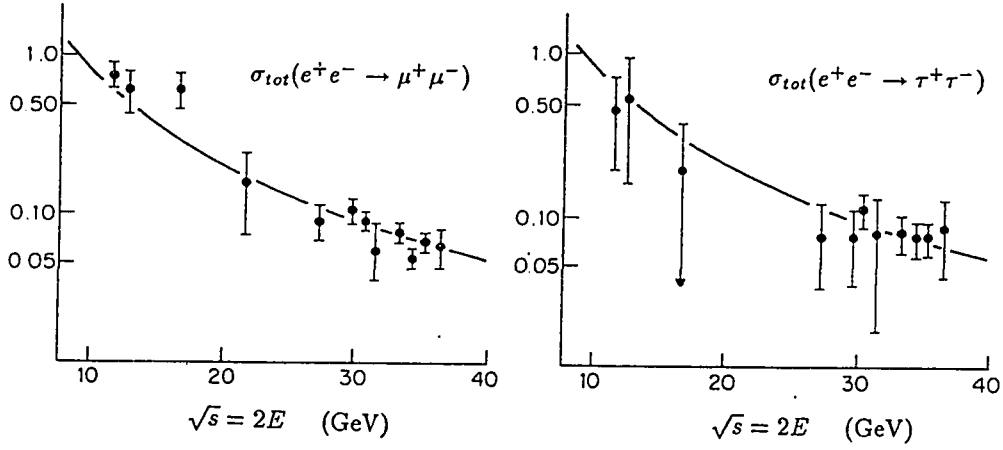


Figure 6: The total cross sections (in nb) for the processes $e^+e^- \rightarrow \mu^+\mu^-$ and $e^+e^- \rightarrow \tau^+\tau^-$ as a function of (relativistic) center-of-mass energies. [After D.P.Barber *et al.*, Phys. Rev. Lett. 43, (1979) 1915.] The dots are experimental data; the curves are the theoretical cross section formula (28).

section becomes

$$\sigma = \frac{86.8}{s(\text{GeV}^2)} \quad \text{nanobarns.} \quad (29)$$

where s is the square of the center-of-mass energy. This cross section is roughly a factor of 10^5 smaller than the Bhabha cross section. Figure 6 shows the total cross section for the two processes as a function of center-of-mass energy.

Because the cross section for electron-positron annihilation into muon pairs is often used in comparisons with cross sections for other processes, this cross section will be defined as

$$\sigma_o \equiv \frac{4\pi\alpha^2}{3s} \quad (30)$$

where $s = (2E_{beam})^2$. The \hbar and c factors have been dropped so that σ_0 is written in natural units. In the following discussions, formulae for cross sections will be written in natural units ($\hbar = c = 1$).

2.1.3 Two-photon production of leptons

There are six processes which can produce leptons from two-photon interactions:

$$e^+e^- \longrightarrow e^+e^-e^+e^- \quad (1)$$

$$e^+e^- \longrightarrow e^+e^-\mu^+\mu^- \quad (2)$$

$$e^+e^- \longrightarrow e^+e^-\tau^+\tau^- \quad (3)$$

$$e^+e^- \longrightarrow \mu^+\mu^-\tau^+\tau^- \quad (4)$$

$$e^+e^- \longrightarrow \mu^+\mu^-\mu^+\mu^- \quad (5)$$

$$e^+e^- \longrightarrow \tau^+\tau^-\tau^+\tau^- \quad (6)$$

The first three of these interactions are similar in that they each have an electron-positron pair among the final state particles. These are the interactions which are significant to this study. The cross sections for the last three interactions are much smaller than those for the first three, since fewer Feynman diagrams contribute in these processes, than do in processes (1) through (3), as explained below.

There are four types of diagrams that may contribute in two-photon interactions. The first group consists of the “multiperipheral” diagrams. These are shown in Figure 7 for process (1). The last two diagrams in the figure also contribute to the cross section for processes (2) and (3). From the diagrams, it is clear that the final state must include the original electron and positron. Therefore, these diagrams contribute in processes (1) through (3), but not in processes (4) through (6). One can see the similarity of these diagrams to those for Bhabha scattering by replacing the single exchanged photon in Figure 1 with the diagram shown in Figure 8 of two photons

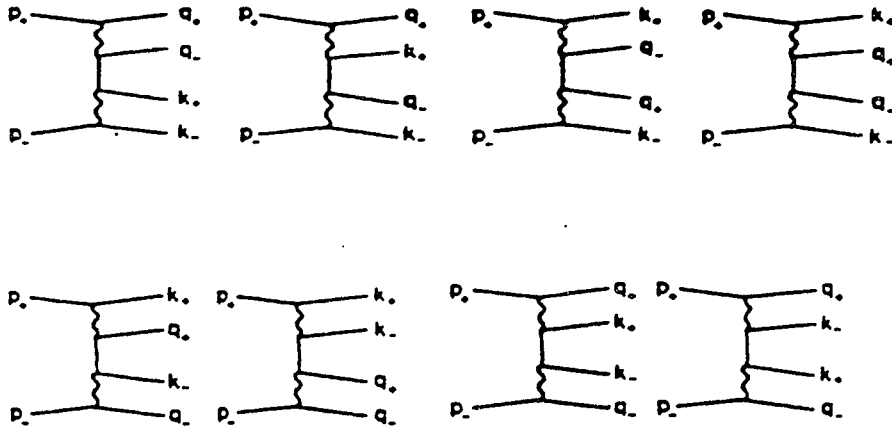


Figure 7: The multiperipheral diagrams for $e^+e^- \rightarrow e^+e^-e^+e^-$. The last two diagrams may also be $e^+e^- \rightarrow e^+e^-\mu^+\mu^-$ and $e^+e^- \rightarrow e^+e^-\tau^+\tau^-$. (From Ref. [1]).

annihilating into a lepton pair.

The second group is the “bremsstrahlung” group, shown in Fig. 9 for process (1). Four of the diagrams may also contribute to processes (2) and (3). Like the multiperipheral diagrams, these also have the original electron and positron as two of the final state particles. Thus, they cannot contribute in processes (4) through (6). This group is called the “bremsstrahlung” group because two of the final state particles are created by a photon radiating from one of the initial particles, or from either the final state electron or positron. These diagrams are also similar to the Bhabha scattering diagram (see Figure 1) where either the electron or positron in the Bhabha scattering process radiates a photon.

The third group is the “annihilation” group, shown in Figure 10. Here, the initial electron and positron are annihilated via a virtual photon, and create a new lepton

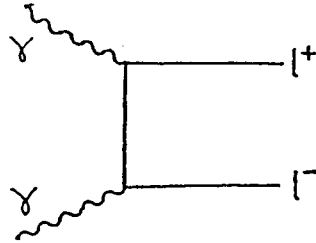


Figure 8: Diagram for photon-photon pair production of leptons.

pair. One of the created leptons radiates a photon to create a second lepton pair. Because the original electron and positron are destroyed, these diagrams contribute to all six processes listed above.

The fourth group is the “conversion” group, shown in Figure 11. Since the final state particles are created in pairs by the two photons, this group contributes to all six processes.

The number of diagrams that contribute in each of the final states, when only photon exchanges are accounted for, is shown in Table 2. The number of contributing diagrams increases by a factor of four when Z^0 exchanges are also taken into account. According to the Feynman rules for calculating cross sections, each lepton-photon vertex gives a factor $(-ie\gamma^\alpha)$ in the Feynman matrix element \mathcal{M} . In the two-photon diagrams, there are four lepton-photon vertices, resulting in $\mathcal{M} \sim \alpha^2$. The cross section σ goes as $|\mathcal{M}|^2$, and so $\sigma \sim e^8$, or α^4 (since every e^2 gives a single factor of α). Thus, the cross section for any two-photon process goes as α^4 . Recall that the

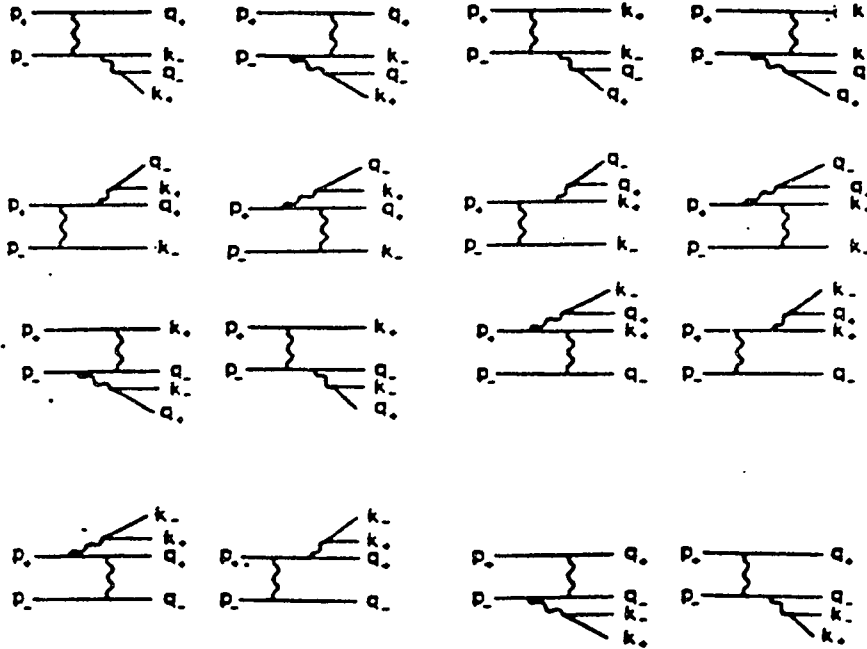


Figure 9: The bremsstrahlung group of diagrams for $e^+e^- \rightarrow e^+e^-e^+e^-$. The diagrams in the last row may also be $e^+e^- \rightarrow e^+e^-\mu^+\mu^-$ or $e^+e^- \rightarrow e^+e^-\tau^+\tau^-$. (From Ref. [1]).

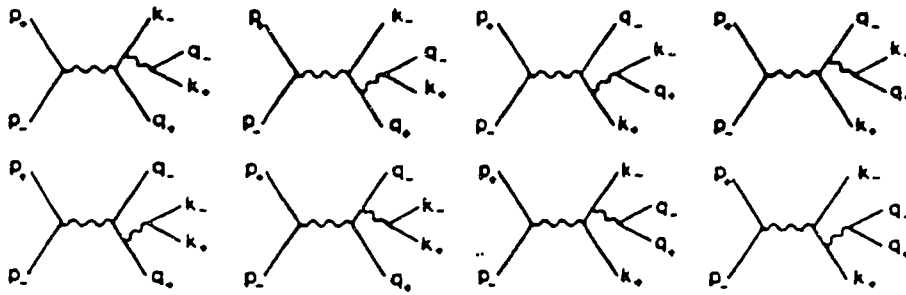


Figure 10: The annihilation group of diagrams for $e^+e^- \rightarrow e^+e^-e^+e^-$, as well as process (5) and (6). The diagrams in the last row may also be processes (2), (3), and (4). (From Ref. [1]).

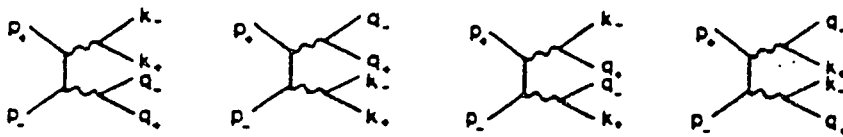


Figure 11: The conversion group of diagrams for processes (1), (5), and (6). The first two diagrams may also contribute to processes (2),(3), and (4). (From Ref. [1]).

Process	Group (I)	Group (II)	Group (III)	Group (IV)	Total
(1) $e^+e^-e^+e^-$	8	16	8	4	36
(2) $e^+e^-\mu^+\mu^-$	2	4	4	2	12
(3) $e^+e^-\tau^+\tau^-$	2	4	4	2	12
(4) $\mu^+\mu^-\tau^+\tau^-$	0	0	4	2	6
(5) $\mu^+\mu^-\mu^+\mu^-$	0	0	8	4	12
(6) $\tau^+\tau^-\tau^+\tau^-$	0	0	8	4	12

Table 2: The number of contributing diagrams in each of the six two-photon processes.

cross section σ_o for $e^+e^- \rightarrow \mu^+\mu^-$ discussed in Section 2.1.2 goes as α^2 . Therefore, the cross section for the two-photon process might be expected to be smaller than σ_o by $\alpha^2 = (\frac{1}{137})^2$. However, as was pointed out above, the multiperipheral diagrams are very similar to the diagram for Bhabha scattering, in that the photon propagator can go to very small momentum transfers because of the zero mass of the photon. Therefore, there is an enhancement to the two-photon cross section which is similar to that for Bhabha scattering.

For example, the total cross section for the process $e^+e^- \rightarrow e^+e^-\mu^+\mu^-$ (for large E_b/m_e) is given by [7]

$$\sigma_{ee \rightarrow ee\mu\mu} \simeq \left(\frac{112\alpha^4}{9\pi m_\mu^2}\right) \left[\ln\left(\frac{E_b}{m_e}\right)\right]^2 \ln\left(\frac{E_b}{m_\mu}\right) \quad (31)$$

where m_μ is the mass of the muon and m_e is the mass of the electron. In terms of $s = (2E_{beam})^2$, this cross section can be written as

$$\sigma_{ee \rightarrow ee\mu\mu} \simeq \left(\frac{112\alpha^4}{9\pi m_\mu^2}\right) \left[\ln\left(\frac{s^{1/2}}{4m_e}\right)\right]^2 \ln\left(\frac{s^{1/2}}{4m_\mu}\right). \quad (32)$$

Recall that σ_o is given by (see Equation 30)

$$\sigma_o = \frac{4\pi\alpha^2}{3s}$$

at high energies (much greater than m_μ). Table 3 lists the cross sections for beam energies from 0.5 GeV to 50 GeV. Below $E = 1$ GeV, the cross section for the virtual photon process dominates the two-photon process. However, above 1 GeV, even with the extra factors of α , the cross section of the two-photon process is much greater than that of the virtual photon process.

It must be stressed that these total cross sections include contributions at small angles. Most of the two-photon cross section comes from these small angle contributions, as in the Bhabha scattering cross section. However, since most experimental

set-ups do not completely cover the entire (4π) solid angle of the interaction region, final particles escaping at small angles may go undetected. Also, the routine used to trigger the experiment may limit the minimum invariant mass W_{min} of the lepton pair that can be observed. Thus, the measured cross sections are reduced by a) integrating the differential cross section from this threshold energy to $W = 2E_{beam}$, and b) integrating the differential cross section over an angular range less than 4π .

When only the two tracks of the muons are observed in the detector, the *detectable* cross section for $e^+e^- \rightarrow e^+e^-\mu^+\mu^-$ will be of the order (for muon energies greater than 1 GeV) [8]

$$\sigma_{ee \rightarrow ee\mu\mu}^{det} \sim \frac{112}{9\pi} \frac{4\alpha^4}{W_{min}^2} \left[\ln\left(\frac{E}{m_e}\right)^2 \{2[\ln^2(\tan \psi/2) + \ln(\sin \psi)]\} \right] \quad (33)$$

where ψ is the minimum polar angle at which the muons can be seen in the detector. For the Mark II detector at the SLC, $W_{min}^2 = 0.09 \text{ GeV}^2$, $\psi = 42^\circ$, and $E \sim 45 \text{ GeV}$. Therefore, substituting these values, the expected detectable cross section is

$$\sigma_{ee \rightarrow ee\mu\mu}^{det} \sim 26 \quad \text{nanobarns.} \quad (34)$$

This cross section is much smaller than the theoretical cross section. More of the theory of two-photon processes will be discussed in Chapter 4.

2.1.4 $e^+e^- \rightarrow l^+l^-$ at the Z^0 mass

The production of lepton pairs from e^+e^- collisions via Z^0 boson exchange is not studied here, but because these interactions contribute to estimates of backgrounds, the basic theory is discussed below.

According to electroweak theory, electrons and positrons can interact not only by virtual photons, but also via the Z^0 boson. When the center-of-mass energy is near or at the Z^0 mass, any lepton which has a mass less than half of the Z^0 mass

E_{beam} (GeV)	0.5	2	5	15	25	35	45	45.5 [†]	50
σ_o (nb)	86.8	5.4	0.87	0.096	0.035	0.018	0.011	1.4	0.009
$\sigma_{ee \rightarrow ee\mu\mu}^{tot}$ (nb)	28.9	78.8	127.6	205.5	249.7	281.9	307.5	308.7	318.7

Table 3: Theoretical cross sections $\sigma_{ee \rightarrow ee\mu\mu}$ and σ_o of the two-photon process $e^+e^- \rightarrow e^+e^-\mu^+\mu^-$ and the photon annihilation process $e^+e^- \rightarrow \mu^+\mu^-$, respectively, calculated at different center-of-mass energies. [†] includes electroweak contribution from the Z^0 boson.

(e, μ, τ and their respective neutrinos) will be produced in pairs. For the case where $l = \mu, \tau$, the lowest order contributing diagrams are shown in Figure 12. When $l = e$, there are two other diagrams which contribute (see Figure 13) to the cross section, in addition to those in Figure 12. These two diagrams are the t-channel diagram for the photon exchange, as described in Section 2.1.1 for Bhabha scattering, and the t-channel diagram for the Z^0 exchange. Because these diagrams contribute primarily at small angles (as was discussed in Section 2.1.1), and because a study of these interactions in detail is beyond the scope of this paper, the simpler case of $l = \mu, \tau$ will be discussed only.

The Feynman amplitude corresponding to the diagrams in Fig. 12 is given by

$$\mathcal{M} = \mathcal{M}_\gamma + \mathcal{M}_Z \quad (35)$$

Following the Feynman rules for calculating cross sections gives the total cross section

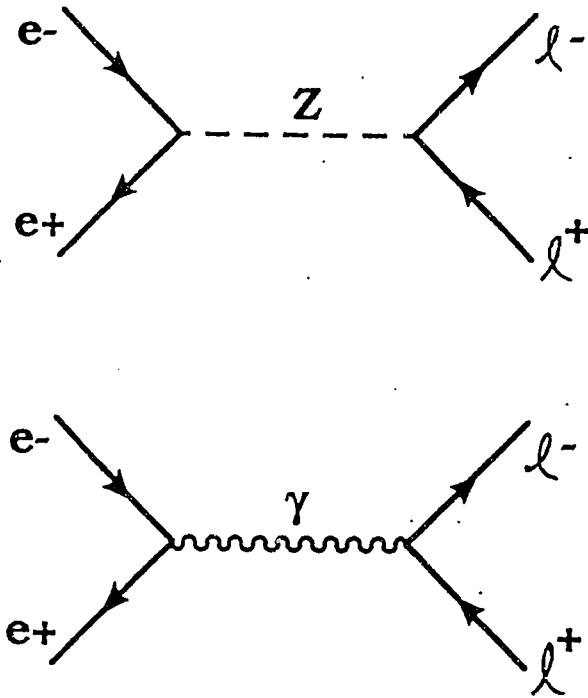


Figure 12: Diagrams contributing to $e^+e^- \rightarrow l^+l^-$ at the Z^0 resonance.

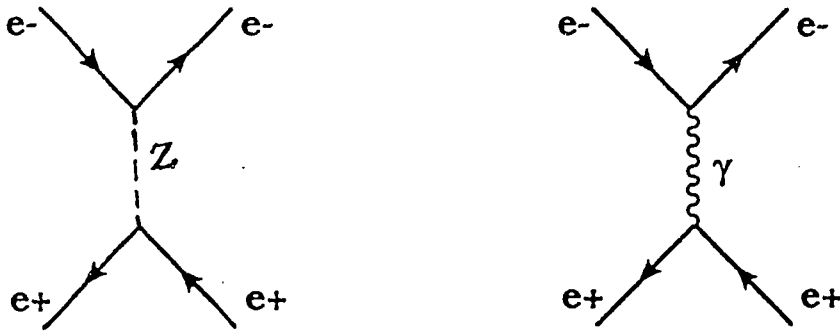


Figure 13: The two t-channel diagrams contributing to $e^+e^- \rightarrow e^+e^-$ at the Z^0 resonance.

$$\sigma = \frac{4\pi\alpha^2}{3s} [1 + 2v_e v_l \text{Re}\chi + (v_e^2 + a_e^2)(v_l^2 + a_l^2)|\chi|^2] \quad (36)$$

where v , a , and χ are given by

$$a_e = a_l = -1 \quad (37)$$

$$v_e = v_l = -1 + 4 \sin^2 \theta_W \quad (38)$$

$$\chi = \left(\frac{G_F}{8\sqrt{2}\pi\alpha} \right) \frac{sm_Z^2}{(s - m_Z^2) + im_Z\Gamma_Z} \quad (39)$$

The angle θ_W is the Weinberg angle, m_Z is the mass of the Z^0 , and Γ_Z is the width of the Z^0 . Current values for these are (from Ref. [9])

$$\sin^2 \theta_W = 0.2324 \pm 0.0033 \quad (40)$$

$$m_Z = 91.175 \pm 0.021 \text{ GeV} \quad (41)$$

$$\Gamma_Z = 2.497 \pm 0.007 \text{ GeV} \quad (42)$$

The first term of Equation 36 is simply the QED term (see Equation 30); the second term comes from the interference between the two diagrams in Figure 12, and the third term is the contribution from the Z^0 exchange diagram. Notice that $\text{Re}\chi$ and $|\chi|^2$ are given by

$$\text{Re}\chi = \left(\frac{G_F}{8\sqrt{2}\pi\alpha} \right) \frac{sm_Z^2(s - m_Z^2)}{(s - m_Z^2)^2 + m_Z^2\Gamma_Z^2} \quad (43)$$

$$|\chi| = \left(\frac{G_F}{8\sqrt{2}\pi\alpha} \right) \frac{sm_Z^3\Gamma_Z}{(s - m_Z^2)^2 + m_Z^2\Gamma_Z^2} \quad (44)$$

At $s \approx m_Z^2$, $\text{Re}\chi$ vanishes, and $|\chi|$ becomes

$$|\chi| = \left(\frac{G_F}{8\sqrt{2}\pi\alpha} \right) \frac{m_Z^3}{\Gamma_Z} = 13.4 \quad (45)$$

(ignoring radiative corrections). Substituting $a_e = a_l = -1$, and $v_e = v_l = -0.1$ as well as the above value for $|\chi|$ into the expression for the total cross section (36) gives

$$\sigma_{s=m_Z^2} = \frac{4\pi\alpha^2}{3m_Z^2} [1 + 183.2] \quad (46)$$

Obviously, the second term, which is due to the Z^0 exchange diagram, dominates the QED term at a center-of-mass energy equal to the mass of the Z^0 . The total cross section (in nanobarns) is

$$\sigma_{s=m_Z^2} = 1.92 \text{ nb.} \quad (47)$$

When radiative corrections are included [10], this total cross section becomes

$$\sigma_{s=m_Z^2} \approx 1.4 \text{ nb.} \quad (48)$$

For all three leptons (e, μ, τ), the total cross section at the Z^0 mass is $3 \times (1.4)$ or 4.2 nanobarns. This is a quarter of the two-photon cross section (see Equation 34) at this energy. Thus, it might be expected that this would be a significant background to a study of two-track two-photon events. However, the lepton pairs arising from Z^0 exchange will have a visible energy approximately equal to the center-of-mass energy; the lepton pair from the two-photon process will not. Therefore, events from these two processes may be easily distinguished from one another.

2.2 Hadron production in e^+e^- collisions

Production of hadrons from e^+e^- collisions is not studied here, but since it contributes to estimates of backgrounds, it will be discussed.

2.2.1 $e^+e^- \rightarrow \text{hadrons}$ via a virtual photon

Hadrons are made up of quarks held together by the strong force. The theory which describes the interactions of quarks is called Quantum Chromodynamics (QCD). While in QED there is an electric charge, in QCD there is a color charge carried by the quarks, eg., red, green, or blue. In QED, the mediating particle is the photon;

in QCD, it is the gluon. Although the photon does not carry an electric charge, the gluon does carry a color charge; therefore, the gluons can interact with each other, as well as with quarks.

Because of this gluon self-interaction, the force between the quarks is very strong, and increases linearly with distance. As two quarks are pulled apart, the strong field between them increases with energy and this energy can produce new $q\bar{q}$ pairs. Thus, quarks are never observed singly, but only in their combinations as hadrons. However, at very high energies, the strong interaction between quarks and gluons becomes negligible (a condition known as “asymptotic freedom”). Therefore, a high energy e^+e^- collision creates a quark and anti-quark pair; then, as the quarks try to pull apart, they “fragment” into hadrons.

The process can be described as

$$e^+e^- \rightarrow q\bar{q} \quad , \quad q\bar{q} \rightarrow \text{hadrons}$$

where q is a quark (u, d, s, c, b). This process is conceptually pictured in Figure 14. The oval in the diagram represents the QCD processes that produce the hadrons which are actually seen. At high energies, and neglecting QCD corrections, the cross section for $e^+e^- \rightarrow q\bar{q}$ can be derived from that for the process $e^+e^- \rightarrow l^+l^-$, which was discussed in Section 2.1.2. Recall that for $e^+e^- \rightarrow \mu^+\mu^-$, the cross section (see Equation 30) is

$$\sigma_0 = \frac{4\pi\alpha^2}{3s}$$

where $s = 4E_{beam}^2$, for energies above the muon mass. The cross section for $e^+e^- \rightarrow q\bar{q}$ is then [47]

$$\sigma_{e^+e^- \rightarrow q\bar{q}} = 3e_q^2\sigma_0 \quad (49)$$

The factor e_q is the fractional charge of the quark q in units of e , the electron charge. The factor of 3 is included to account for the diagrams from each quark color (red,

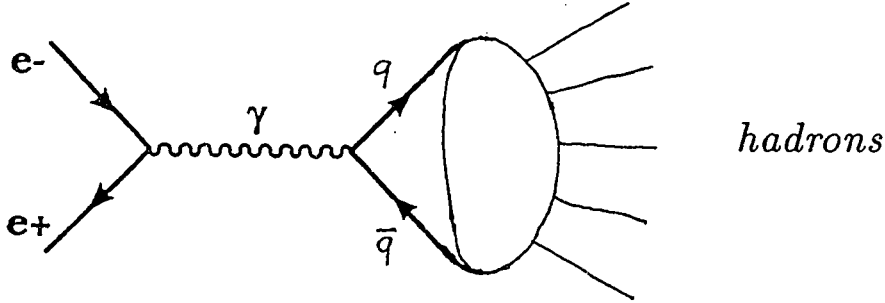


Figure 14: Conceptual picture of hadron production from e^+e^- annihilation.

blue, and green). The cross section for producing all types of hadrons is obtained by summing over all quark flavors $q = u, d, s, \dots$ that can be produced at the center-of-mass energy $E_{cm} = 2E_{beam}$. Therefore,

$$\sigma_{e^+e^- \rightarrow \text{hadrons}} = \sum_q \sigma_{e^+e^- \rightarrow q\bar{q}} \quad (50)$$

$$= 3 \sum_q \sigma_0 \quad (51)$$

or

$$\sigma_{e^+e^- \rightarrow \text{hadrons}} = 3 \sum_q \frac{4\pi\alpha^2 e_q^2}{3s} \quad (52)$$

This can be written in the standard form

$$R \equiv \frac{\sigma_{e^+e^- \rightarrow \text{hadrons}}}{\sigma_0} = 3 \sum_q e_q^2$$

Therefore, depending on how many quarks have masses below the center-of-mass

energy, R can take on the values

$$\begin{aligned}
 R &= 3\left[\left(\frac{2}{3}\right)^2 + \left(\frac{1}{3}\right)^2 + \left(\frac{1}{3}\right)^2\right] = 2 \quad \text{for } u, d, s \\
 &= 2 + 3\left(\frac{2}{3}\right)^2 = \frac{10}{3} \quad \text{for } u, d, s, c \\
 &= \frac{10}{3} + 3\left(\frac{1}{3}\right)^2 = \frac{11}{3} \quad \text{for } u, d, s, c, b
 \end{aligned}$$

Figure 15 shows these predicted values of R compared to experimentally measured values. The sharp peaks correspond to the production of resonances just below or near the thresholds for creating the higher mass quark flavors. For example, $R \simeq 2$ below the threshold for creating hadrons which have the charm quark as a constituent ($Q = 2(m_c + m_u) \simeq 3.7$ GeV). Above the threshold for creating a hadron with two b quarks ($Q > 2m_b \simeq 10$ GeV), $R \simeq \frac{11}{3}$ as predicted. This is used as proof of the existence of color charge, since if there was only one color, R would be reduced by a factor of 3 (see Equation 49).

Recalling the cross section for $e^+e^- \rightarrow l^+l^-$, $\sigma_0 = 86.8/s$ (GeV^2) nanobarns (Equation 29), and using the definition of R above, the cross sections can be written as

$$\sigma_{e^+e^- \rightarrow \text{hadrons}} = 2(86.8/s) = 173.6/s \quad \text{for } u, d, s \quad (53)$$

$$= \frac{10}{3}(86.8/s) = 289.3/s \quad \text{for } u, d, s, c \quad (54)$$

$$= \frac{11}{3}(86.8/s) = 318.3/s \quad \text{for } u, d, s, c, b \quad (55)$$

where s is in GeV^2 and σ is in nanobarns.

Table 4 lists the $\sigma_{e^+e^- \rightarrow \text{hadrons}}$ cross section calculated for several energies. Also listed are the total and detectable cross sections for $\sigma_{ee \rightarrow ee\mu\mu}$ from Section 2.1.3 at these energies. Below $E_{\text{beam}} = 5$ GeV, the hadronic cross section is larger than the two-photon cross section; the situation is reversed for the higher energies. Even the detectable two-photon cross section is many orders of magnitude higher than the hadronic cross section at the higher energies. Notice however, that these cross

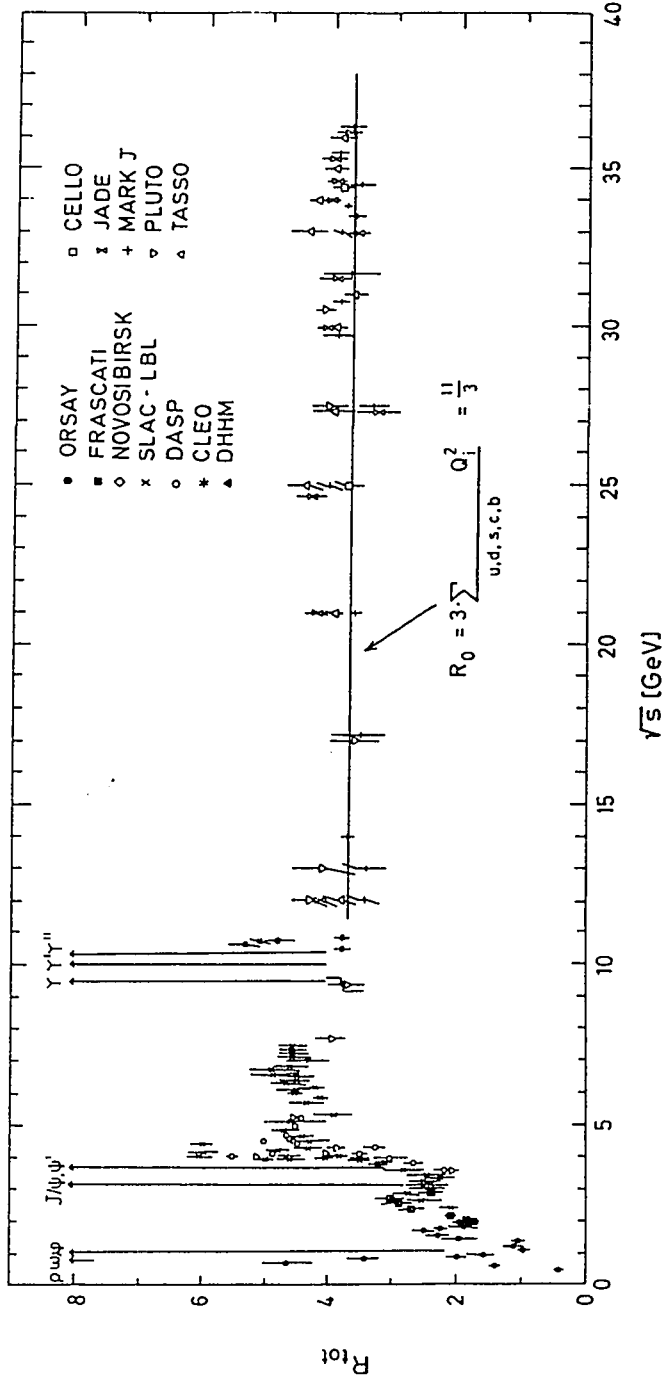


Figure 15: Ratio R as a function of E_{cm} . The sharp peaks correspond to the production of various resonances. (From Ref. [11]).

E_{beam} (GeV)	0.5 †	2	25	35	45	45.5 ‡	50
$\sigma_{e^+e^- \rightarrow hadrons}$ (nb)	147.6	18.08	0.13	0.06	0.04	32.8	0.03
$\sigma_{ee \rightarrow ee\mu\mu}^{tot}$ (nb)	28.9	78.8	249.7	281.9	307.5	308.7	318.7
$\sigma_{ee \rightarrow ee\mu\mu}^{det}$ (nb)	9.5	13.7	23.3	24.8	25.9	26.0	26.4

Table 4: Cross sections for $e^+e^- \rightarrow hadrons$, $\sigma_{ee \rightarrow ee\mu\mu}^{tot}$ and $\sigma_{ee \rightarrow ee\mu\mu}^{det}$ for different beam energies. At $E_{beam} = 0.5$ GeV (†), only the u and d quarks contribute. At $E_{beam} = 45.5$ GeV (‡), the Z^0 contribution is included.

sections do not take into account the electroweak contribution from $Z^0 \rightarrow hadrons$; this will be covered in Section 2.2.3.

2.2.2 $e^+e^- \rightarrow e^+e^-hadrons$ via two-photon interaction

Another possible background comes from events created by the two-photon process $e^+e^- \rightarrow e^+e^-hadrons$, primarily $e^+e^- \rightarrow e^+e^-\pi^+\pi^-$. As shown in Sections 2.1.2 and 2.2.1, this is a two-photon process where the l^\pm in the process $e^+e^- \rightarrow e^+e^-l^+l^-$ of Section 2.1.2 are replaced by a $q\bar{q}$ pair, and the quarks subsequently fragment into hadrons. For simplicity, the case where the hadrons are two pions (π^\pm) will be considered here only.

The evaluation of the total cross section for pion pair production is not as simple as the muon case because of the QCD corrections (as was pointed out in Section 2.2.1 for single photon exchange). However, as a first approximation, the pions may be

treated as pointlike particles [7] and their strong interaction neglected. Then, for very large E/m_e , the cross section for $e^+e^- \rightarrow e^+e^-\pi^+\pi^-$ is given by [7]

$$\sigma_{ee \rightarrow ee\pi\pi} \simeq \frac{16\alpha^4}{9\pi} \frac{1}{m_\pi^2} \left[\ln\left(\frac{E}{m_e}\right) \right]^2 \ln\left(\frac{E}{m_\pi}\right) \quad (56)$$

where E is the beam energy and m_π is the mass of the pion. Table 5 lists this cross section, as well as $\sigma_{ee \rightarrow ee\mu\mu}$, calculated at different beam energies. The cross sections for pion pair production are much less than that for muon pairs. However, just as detector constraints affect the detectable cross section for the lepton pairs, it similarly affects the detectable cross section for pion pairs. If the triggering threshold of the detector is above the energy $W = 2m_\pi$, then the detectable cross section for pion pair production is given by

$$\sigma_{ee \rightarrow ee\pi\pi}^{det} \sim \frac{16\alpha^4}{9\pi} \frac{4}{W_{min}^2} \left[\ln\left(\frac{E}{m_e}\right) \right]^2 2 \left[\ln^2(\tan \psi/2) + \ln(\sin \psi) \right] \quad (57)$$

where W_{min} is the minimum invariant mass of the pair that will be detected and ψ is the minimum polar angle of one of the pions. Table 6 shows the detectable cross sections for pion pair production and muon pair production. Because of the factor of 16 in Equation 57 instead of 112 as in Equation 33, the detectable cross section for pion pair production is 1/7 that for muon pair production.

2.2.3 $e^+e^- \rightarrow hadrons$ at the Z^0 mass

The methods described in Sections 2.1.4 and 2.2.1 can be used to estimate cross sections for the process $e^+e^- \rightarrow hadrons$ at a center-of-energy near the Z^0 mass. As shown in section 2.2.1, this QCD process can be thought of as

$$e^+e^- \rightarrow Z^0 \rightarrow q\bar{q} \quad (58)$$

E_{beam} (GeV)	0.5	2	25	35	45	50
$\sigma_{ee \rightarrow ee\pi\pi}$ (nb)	1.96	5.9	19.6	22.2	24.2	25.1
$\sigma_{ee \rightarrow ee\mu\mu}^{tot}$ (nb)	28.9	78.8	249.7	281.8	307.5	318.7

Table 5: Theoretical cross sections for $e^+e^- \rightarrow e^+e^-\pi^+\pi^-$ and $e^+e^- \rightarrow e^+e^-\mu^+\mu^-$ calculated at several beam energies.

E_{beam} (GeV)	0.5	2	25	35	45	50
$\sigma_{ee \rightarrow ee\pi\pi}^{det}$ (nb)	1.4	1.9	3.3	3.5	3.7	3.8
$\sigma_{ee \rightarrow ee\mu\mu}^{det}$ (nb)	9.5	13.7	23.3	24.8	25.9	26.4

Table 6: Predicted detectable cross sections for pion and muon pair production from two-photon interactions, calculated for several beam energies using Equations 33 and 57.

quark	a_q	v_q	$a_q^2 + v_q^2$
u, c, t	1	0.382	1.146
d, s, b	-1	0.691	1.477

Table 7: The axial and vector couplings for each quark assuming $\sin^2 \theta_W = 0.232$.

where the quarks subsequently fragment into hadrons. For the process $e^+e^- \rightarrow q\bar{q}$ at the Z^0 mass, the cross section is dominated by the term due to the Z^0 boson exchange:

$$\sigma = \frac{C_q G_F^2 M_Z^4 s}{96\pi[(s - M_Z^2)^2 + M_Z^2 \Gamma_Z^2]} [(a_e^2 + v_e^2)(a_q^2 + v_q^2)] \quad (59)$$

where a_e and a_q are the axial couplings for the electron and quark, and v_e and v_q are the vector couplings for the electron and quark. C_q is a color factor for each quark ($C_q = 3$). Table 7 lists a_q, v_q for the different quarks.

Therefore, the cross section for producing one quark flavor is

$$\sigma = 6.52 \text{ nb.} \quad \text{for } u, c, t \quad (60)$$

$$\sigma = 8.31 \text{ nb.} \quad \text{for } d, s, b \quad (61)$$

and the total hadronic cross section is

$$\sigma = 3(6.52) + 3(8.31) = 44.5 \text{ nb.} \quad (62)$$

When radiative corrections are included [10], this total cross section becomes

$$\sigma \sim 33 \text{ nb.} \quad (63)$$

Chapter 3

Experimental Apparatus

The data were obtained using the Mark II detector at the SLAC Linear Collider (SLC) [12]. The Mark II detector was originally used at the SPEAR and PEP storage rings, and was later upgraded for use as the first detector at the SLC. In the SLC, electron and positron beams collide at a center-of-mass energy, E_{cm} , of approximately 91 GeV, the Z^0 resonance energy. This chapter describes the operation of the SLC and the detector systems.

3.1 The SLAC Linear Collider

A schematic outline of the SLC is shown in Figure 16. Electron and positron bunches are first stored in the two damping rings for approximately 3 milliseconds where their emittance is reduced. After extraction, the electron and positron bunches are simultaneously accelerated down the linear accelerator (LINAC) to their final energies. At the end of the LINAC, the bunches are separated into their respective arcs, and made to collide at the interaction point (IP). The Mark II detector, centered at the IP, detects and tracks the particles resulting from the collision. After colliding, the

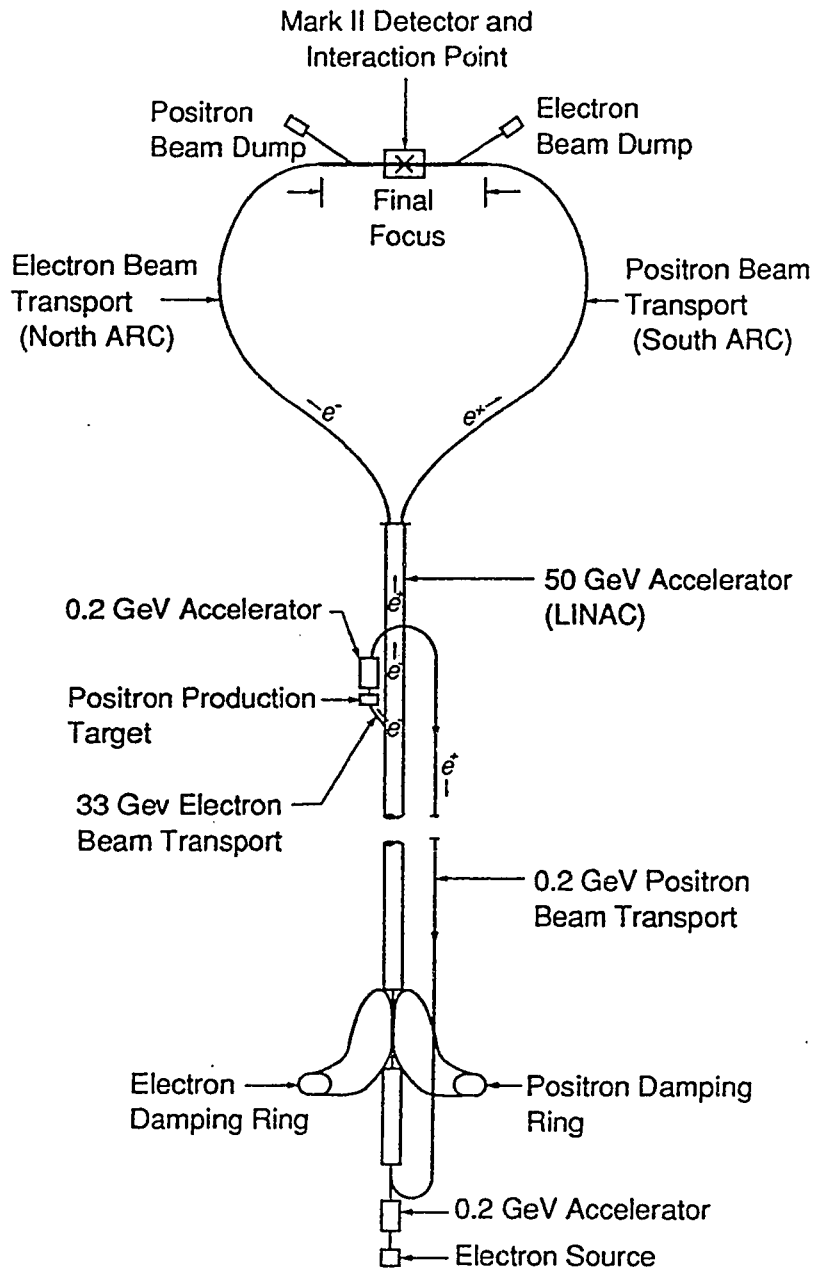


Figure 16: A schematic outline of the SLC.

bunches are sent to separate beam dumps. The beam energies are measured in the extraction lines.

The LINAC accelerates the electron and positron bunches to energies up to approximately 50 GeV. Each bunch loses approximately 1 GeV of energy due to synchrotron radiation in traveling down the arcs. Some of the achieved operational parameters are listed in Table 8. The quantities σ_x and σ_y are the transverse beam dimensions. Although the peak Z^0 rate ultimately achieved exceeded 4 Z^0 s/hr (4.87 Z^0 s/hr), this could not be sustained for long times. A luminosity of 1.5 Z^0 s/hr ($1.3 \times 10^{28} \text{ cm}^{-2}\text{sec}^{-1}$) was typical for good continuous running. The data were col-

Parameter	Achieved	Design
Repetition rate	120 Hz	120 Hz
Intensity, N^\pm /bunch	3.0×10^{10} (N^-) 1.6×10^{10} (N^+)	6×10^{10}
Spot sizes, σ_x, σ_y	$3.3 \mu\text{m}$	$1.65 \mu\text{m}$
Luminosity, \mathcal{L} ($\text{cm}^{-2}\text{sec}^{-1}$)	3.4×10^{28}	4×10^{30}
Z^0 rate	4.0/hr	470/hr

Table 8: SLC operational parameters.

lected in a run from April to October 1989 (Run 1989), and a run from July to November 1990 (Run 1990). More details on the integrated luminosities can be found in Chapter 5.

3.2 The Mark II Detector

The upgraded Mark II detector is shown in Figure 17. A detailed description of the detector can be found in Ref. [13]. This section gives an overview of the detector and describes the operation of the major detector systems.

3.2.1 Overview

In traveling radially from the interaction point, a particle would encounter (in order):

Beampipe For Run 1989, the beampipe is an aluminum cylinder with an inner radius of 3.37 cm and thickness 0.76 mm. This results in 0.0085 radiation lengths of material at normal incidence. Wire flippers were located at $z = \pm 0.18$ m. These are used to measure single beam profiles and determine the beam position to first order [14]. They add about 7.5% to the scattering thickness of the beampipe at approximately 20° from the beam axis.

For Run 1990, a new beampipe designed to fit inside the two vertex detectors is used. The new pipe is also an aluminum cylinder, but has an inner radius of 2.5 cm, and a thickness of 0.41 mm. Together with its beam wire flippers, this beampipe has 0.0063 radiation lengths of material.

Silicon Strip Vertex Detector (SSVD) The Silicon Strip Vertex Detector (SSVD) is used in Run 1990. The SSVD consists of 36 independent detector modules in two hemi-cylindrical structures [15]. They are attached to the beampipe at the IP. The silicon strips are grouped in three radial layers, as shown in Figure 18. The strips are oriented parallel to the beam axis, and provide measurements of track position in the r - ϕ plane only. The strips are $300 \mu\text{m}$ thick, have a spatial

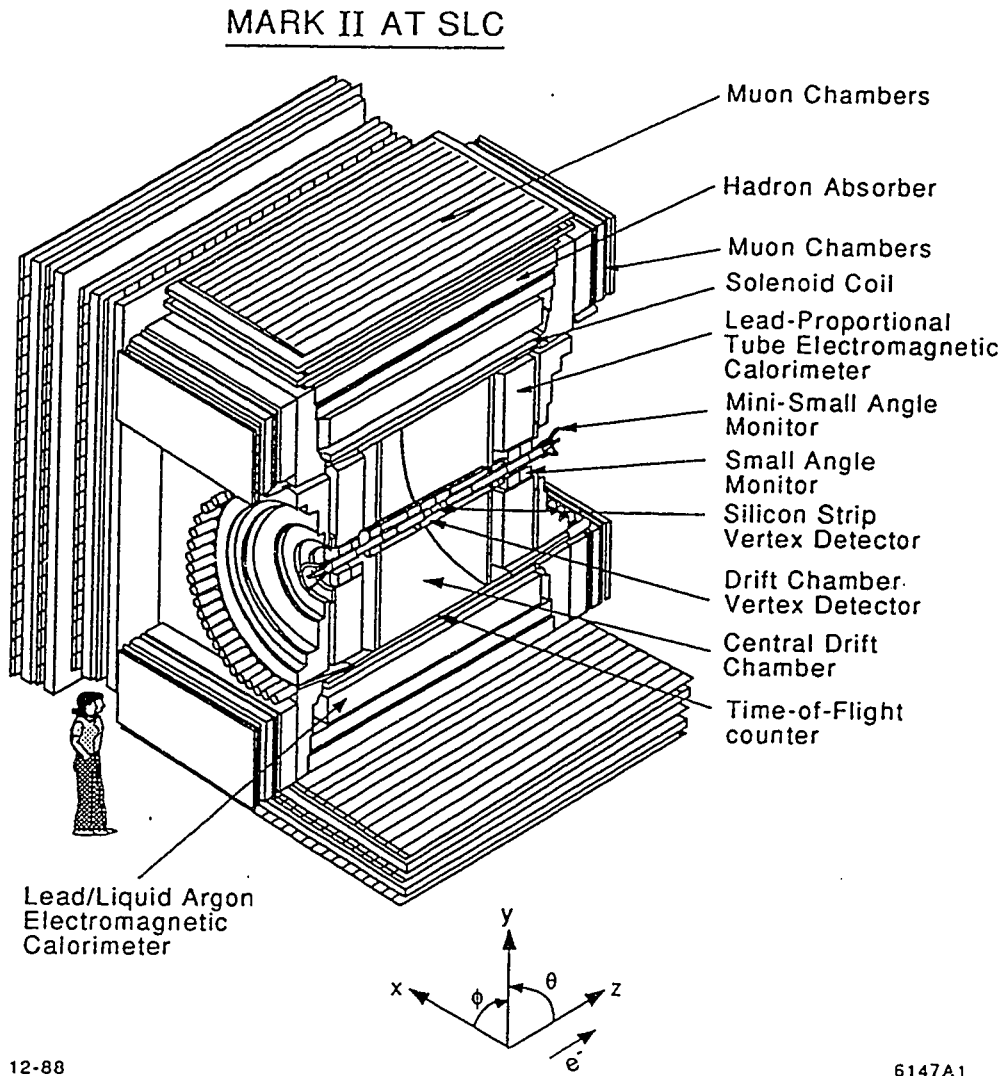


Figure 17: The Mark II detector

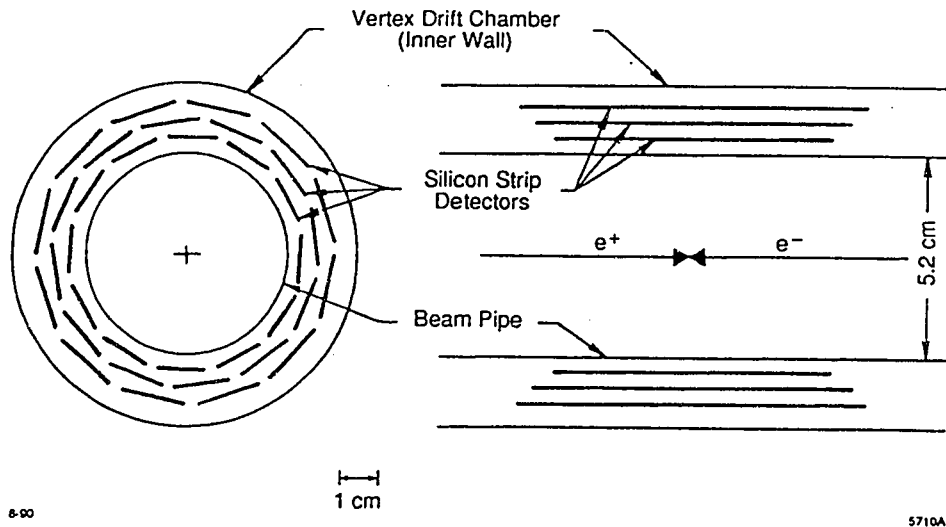


Figure 18: Layout of the SSVD layers.

resolution of about $5 \mu\text{m}$ and a two track separation resolution of approximately $150 \mu\text{m}$. Multiple scattering in the material makes this resolution worse at low momentum.

Drift Chamber Vertex Detector (DCVD) Also installed for Run 1990 is the drift chamber vertex detector (DCVD)[17]. The vertex information is independent of and complements that of the SSVD. The DCVD is a jet-type drift chamber. Its active volume extends radially from 5 cm to 17 cm, and is 55 cm long. The total amount of material is 0.010 radiation lengths thick.

The DCVD is divided into 10 axial drift cells (see Fig. 19). Each cell is tilted approximately 15° in ϕ with respect to the radial direction. This allows resolution of the left-right ambiguity and ensures that all tracks are measured along

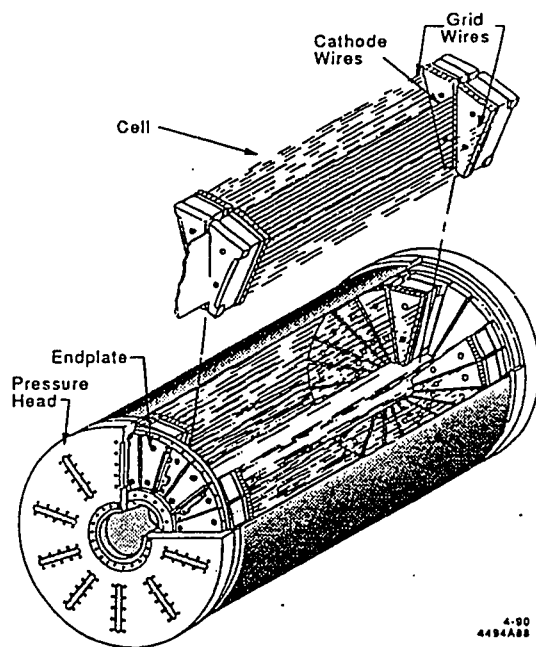


Figure 19: The drift chamber vertex detector.

their entire length. Like the SSVD, the DCVD can give track position information in the r - ϕ plane only. Each cell has a sense plane with 38 active sense (anode) wires, alternating with field wires held at ground (see Fig. 20). The drift gas (92% CO_2 , 8% ethane) runs in the unsaturated regime for low electron diffusion and a slow ($6 \mu\text{m}/\text{nsec}$) drift velocity. The impact parameter for high momentum tracks is $30 \mu\text{m}$; the two track resolution is $500 \mu\text{m}$.

Central Drift Chamber (CDC) The central drift chamber is used for analyzing charged particles. In combination with a magnetic field, it provides tracking and momentum measurements, as well as some particle identification of the charged tracks. It is further described in Section 3.2.2.

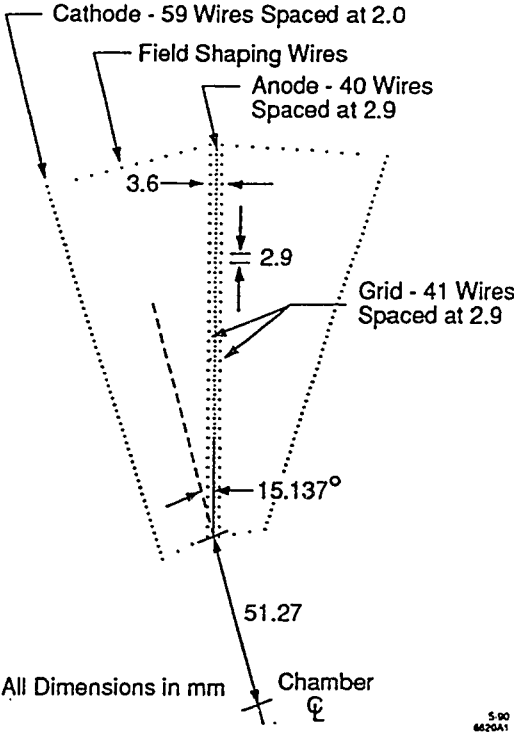


Figure 20: Wire configuration for the DCVD.

Time-of-Flight (TOF) The TOF system consists of 48 scintillator slabs located at a radius of 152.4 cm, parallel to the beam direction. It provides timing information for charged particle identification and is also used to tag cosmic rays. It is described in Section 3.2.3.

Solenoid The solenoid is constructed from an aluminum cylindrical coil which produces a magnetic field of 4.75 kG at the center of the detector. The amount of coil material and cooling water results in 1.3 radiation lengths. The solenoid is 405 cm long and has inner and outer radii of 156 cm and 171 cm respectively. The field inside the detector is measured and fit to a set of polynomials with an error of less than 0.1%. It is uniform within the tracking volume to within 3%. During data taking, Hall probes at both ends of the drift chamber are used to monitor the field.

Liquid Argon Barrel Calorimeter (LA) The LA is an electromagnetic calorimeter consisting of eight independent lead/liquid argon modules arranged in an octagonal barrel outside the magnetic coil. The modules cover a polar angle range of 47° to 133° and cover the full azimuthal angle except for 3° gaps between pairs of modules. The total solid angle coverage is 63.5%. The material in the entire system results in 16.0 radiation lengths at normal incidence.

The energy resolution, for Bhabha events at PEP, is $\sigma(E)/E = 4.6\%$. At PEP, in hadronic events, electrons were identified with an efficiency of 78% at 1 GeV/c to 93% at the highest momentum. For the low momentum particles in this analysis, the resolution of the LA calorimeter is much worse than that of the CDC, so it is not used.

Muon Chambers This system consists of four layers of hadron absorber and proportional tubes on four sides around the detector. Each wall has four alternating layers of iron and proportional tubes. It covers 45% of the solid angle, and is 7.3 radiation lengths thick. The inner layer measures the polar coordinate of a track; the outer three layers measure the azimuthal coordinate. The system has an efficiency of $> 85\%$ for identifying muons with momenta greater than 1.8 GeV/c.

At small angles, moving out in z from the IP, the systems are:

Endcap Calorimeter (ECC) Located at each end of the detector, the two endcap calorimeters provide electromagnetic calorimetry in the angular region between approximately 15° and 45° from the beam axis. They have inner and outer radii of 40 cm and 146 cm and are located at $z = \pm 1.37$ m. Each endcap has 36 layers of lead, 0.28 cm thick; each layer is separated by a plane of proportional tubes. The material in each endcap results in 18 radiation lengths. From Bhabha events measured at PEP, the ECCs are known to have an energy resolution of $\sigma(E)/E = 0.22/\sqrt{E}$ (E in GeV).

Small Angle Monitor (SAM) The small angle monitor is a luminosity monitor for the SLC. A tracking section of drift tubes and a calorimeter of lead and proportional tubes provides identification and measurement of small angle Bhabha electrons and positrons. It is described in Section 3.2.4.

Mini-Small Angle Monitor (Mini-SAM) The Mini-SAM is a tungsten/scintillator calorimeter which also acts as a luminosity monitor by identifying Bhabha electrons and positrons. It is described in Section 3.2.4.

3.2.2 Central Drift Chamber (CDC)

The central drift chamber is an assembly of twelve concentric cylindrical layers of cells; each cell has six sense wires. Layers are alternately “axial”, with the wires parallel to the beam axis, and “stereo”, where the wires are at an angle of $\pm 3.8^\circ$ to the beam axis. The stereo layers allow for position information in the z direction. The innermost layer has 26 cells; each succeeding layer has ten more cells than the preceding one.

The inner radius of the CDC is 19.2 cm, the outer radius is 151.9 cm, and the wire length is 2.3 m. The aluminum endplates are 5.1 mm thick and are held apart by a 2 mm thick beryllium inner cylinder and a 1.27 mm thick aluminum outer shell. Eight aluminum ribs (2.5 mm by 5.1 mm) are attached to the outer shell for structural support. The aluminum shell and beryllium cylinder are each lined with a layer of copper-clad Kapton. The copper layers carry voltages to produce a uniform electric field in the innermost and outermost layers. The design parameters are listed in Table 9.

The layout of wires in a cell is shown in Figure 21. The sense wires are 30 μm diameter gold-plated tungsten. To resolve the left-right ambiguity, the sense wires are staggered $\pm 380 \mu\text{m}$ from the cell axis. The average uncertainty in wire location is 35 μm .

Nineteen field wires with voltages of -4.5 kV produced the uniform electric field; potential wires with voltages of -1.5 kV and guard wires shape the electric field near the sense wires, which are at ground potential. The uniform drift field is 900 V/cm. As charged particles pass through the chamber, they ionize the gas (89% Ar, 10% CO_2 , 1% CH_4 at 1 atmosphere). The ionized electrons drift to the sense wires at a drift velocity of about 52 $\mu\text{m}/\text{ns}$; thus, measuring the drift time gives the distance of the

Layer	Radius at center (cm)	Stereo Angle (degrees)		Number of cells
		Wire 1	Wire 6	
1	27.05	0	0	26
2	38.25	3.65	4.07	36
3	48.45	0	0	46
4	59.25	-3.73	-4.00	56
5	69.45	0	0	66
6	80.15	3.76	3.96	76
7	90.35	0	0	86
8	100.95	-3.77	-3.93	96
9	111.15	0	0	106
10	121.65	3.77	3.91	116
11	131.85	0	0	126
12	142.35	-3.78	-3.89	136

Table 9: Design parameters for the central drift chamber.

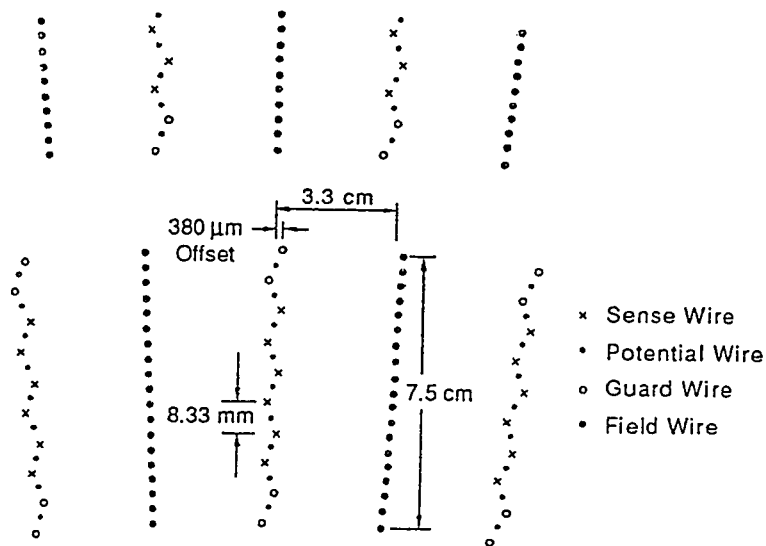


Figure 21: Wire layout for the central drift chamber (CDC).

wire from the charged track.

The sense wire signals are amplified and sent to two different systems: one for time digitization and another for pulse shape digitization. LeCroy 1979 FASTBUS TDCs provide the time digitization for track reconstruction. SLAC-designed [18] 100 MHz Flash ADCs (FADCs) digitize the pulse shapes. The pulse shapes are used to determine energy loss of the track (dE/dx) for particle identification. The FADCs also give timing information for double hit and two track separation when the TDCs cannot resolve the hits.

Tracking efficiency

Tracks are reconstructed by forming track segments when hits line up in a cell. Segments are joined together across layers to form tracks [19]. The track finding efficiency was measured at PEP and has been studied extensively in Monte Carlo simulation for the SLC. The efficiency is above 97% up to $|\cos\theta| \approx 0.8$, as determined using Bhabha events at PEP and Monte Carlo studies with SLC data. The measured (Data) and calculated (MC) efficiencies are shown in Figure 22 as a function of $\cos\theta$. It is estimated to be $> 99\%$ for isolated tracks which cross all 12 layers of the chamber. The detected charged multiplicity observed in the data is approximately flat below $|\cos\theta| \approx 0.8$, in agreement with the Monte Carlo (see Figure 23). The loss in multiplicity at low momentum is well-modeled (see Figure 24). In order to avoid regions of reduced track finding efficiency, only tracks with $|\cos\theta| \leq 0.8$ and $p_{xy} > 0.15$ GeV/c will be used.

Position and momentum resolution

The position resolution of the CDC ranges from 220 μm for the longest drift distances to 130 μm for tracks passing close to the sense wire. The momentum resolution for single tracks was measured using Bhabha scattering events at PEP (in

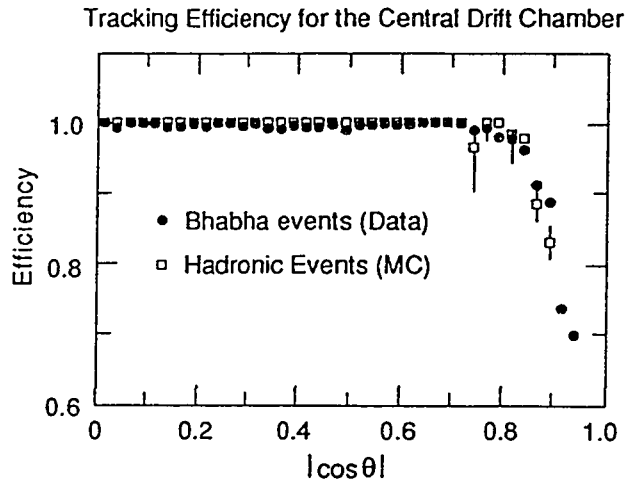


Figure 22: Measured (Data) and calculated (MC) CDC track reconstruction efficiency as a function of $\cos\theta$ [13].

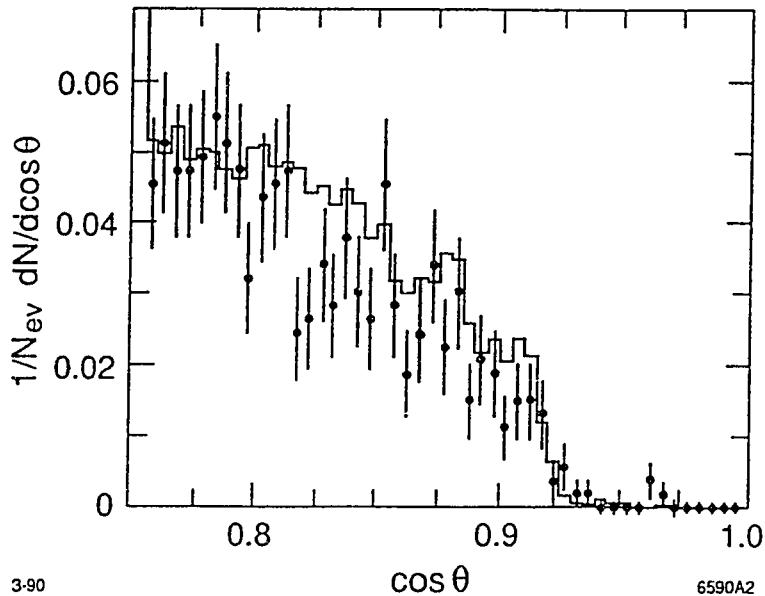


Figure 23: Charged track multiplicity at large polar angles in the central drift chamber. [19] The data used (points) are from the 1989 run. The Monte Carlo simulation (line) is normalized to the total number of events.

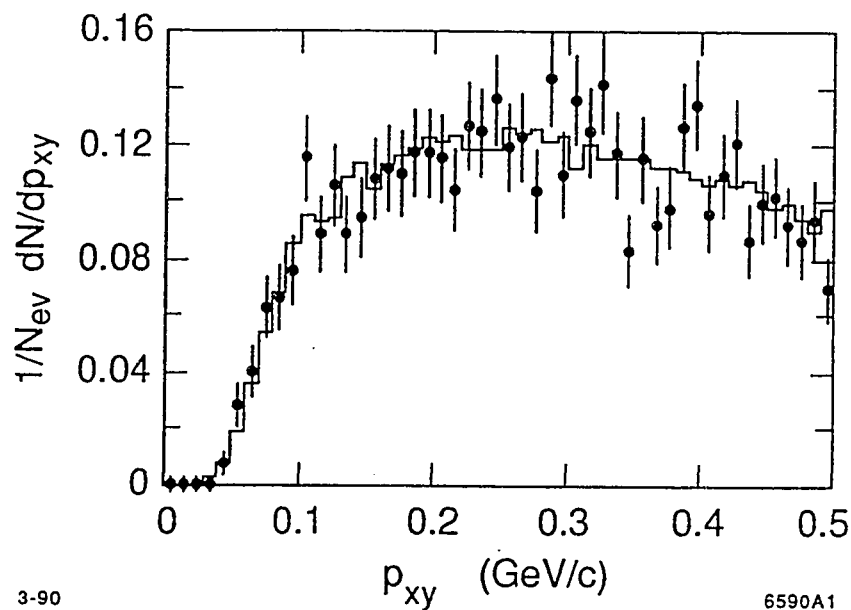


Figure 24: Charged track multiplicity at low momentum in the central drift chamber. [19] The data used (points) are from the 1989 run. The Monte Carlo simulation (line) is normalized to the total number of events.

a 4.5 kG field). This resolution is

$$\frac{\sigma(p)}{p} = \sqrt{(0.0046p)^2 + (0.019)^2} \quad (64)$$

with p in GeV/c. The first term in Equation 64 represents the intrinsic resolution of the CDC, while the second term arises from multiple scattering in material encountered before the CDC inner radius.

Particle identification

The FADC system provides a way to identify electrons, pions, kaons, and protons by measuring the charge deposited by a particle as it travels through the chamber. This charge is proportional to the particle's energy loss (dE/dx). When combined with the measured momentum, the value of dE/dx gives the particle's mass. For a track traversing all 12 layers, there are 72 ionization samples (6 wires per cell for

12 cells).

A “difference of samples” algorithm [20] scans each FADC pulse and looks for sharp changes in its shape, in order to determine the start and end of the pulse. The charge is calculated by summing the counts between the start and end of the pulse as identified by the algorithm. The charge that collects depends on the path length, the angle the track makes with the wire, the drift distance, as well as pressure and temperature differences in the gas. Each measured charge is corrected for these effects and a (75%) truncated mean of the samples is calculated, giving the dE/dx value for the track.

The dE/dx values for particles at PEP are shown as a function of momentum in Figure 25. The separation of electrons from pions for tracks ranging in momentum from 0.25 GeV to 0.60 GeV is shown in Figure 26. For particles at the SLC, Rick van Kooten has performed a fit using SLC data [21]. The $\mu^+\mu^-$ and e^+e^- data from the SLC as well as minimum ionizing pions, protons, and cosmic rays are included in the fit, shown in Figure 27. More details can be found in Reference [21]. The resolution achieved for minimum ionizing tracks at the SLC is 8.5% of the measured value. Particle identification is also provided by the time-of-flight system.

3.2.3 Time-of-Flight (TOF)

The time-of-flight system provides charged particle identification as well as timing information for cosmic rays. Forty-eight plastic scintillator counters form a barrel of inner radius 152.4 cm, just outside the central drift chamber. Each counter is 300 cm long and has a trapezoidal cross section with the smaller width measuring 19.8 cm. The counters are 4.5 cm thick, except for two counters at $\phi=0^\circ$ and two counters at $\phi=180^\circ$ which are 3.8 cm thick. At both ends of the counters are light guides which

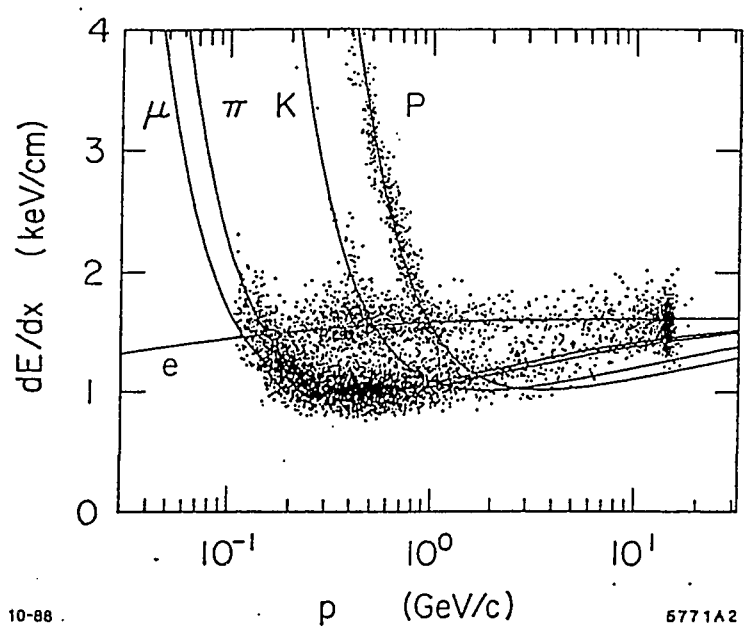


Figure 25: dE/dx values at PEP as a function of momentum.

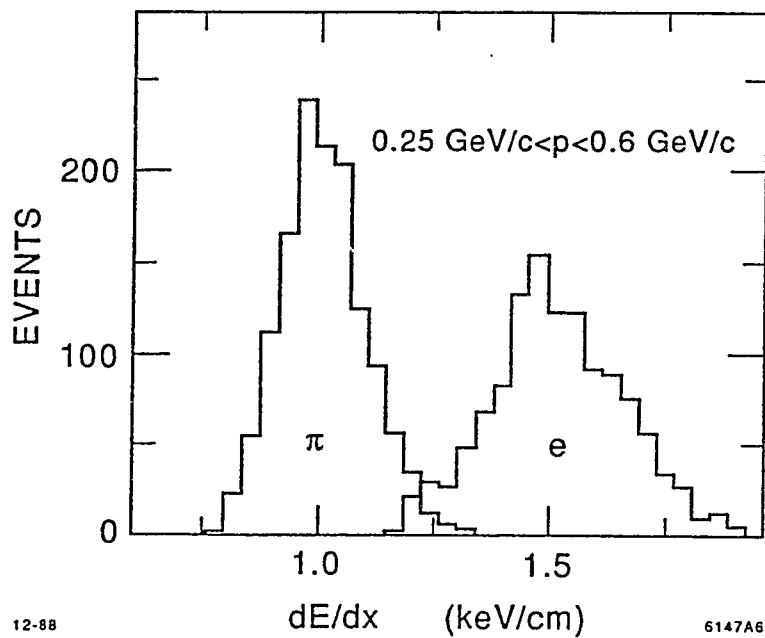


Figure 26: Electron-pion separation at PEP.

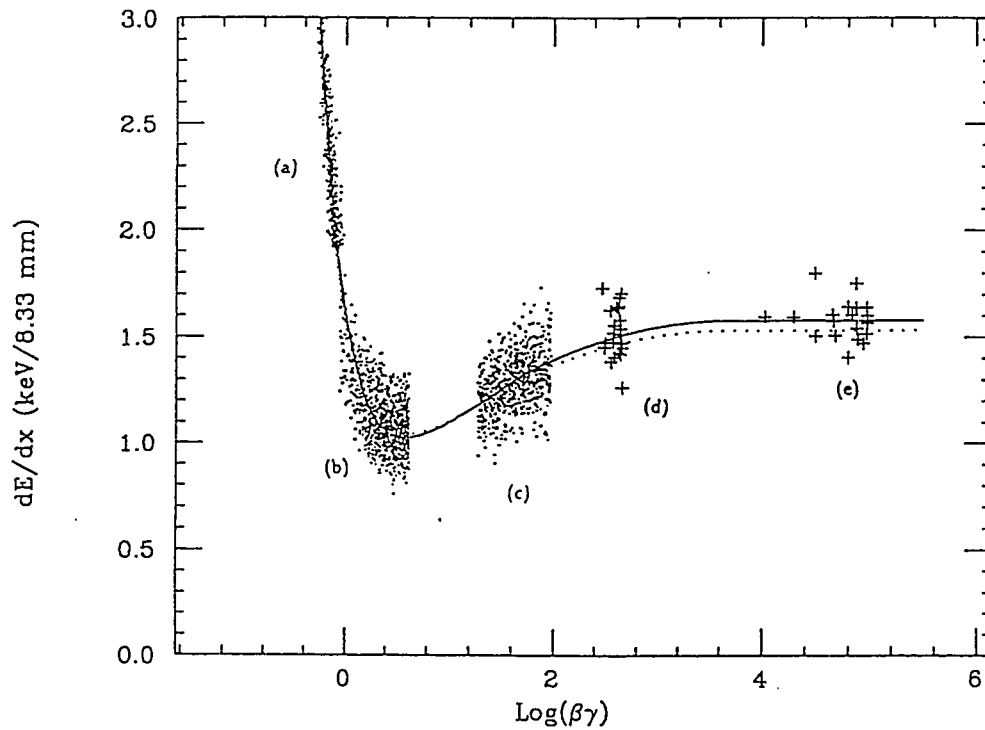


Figure 27: Fit of the dE/dx theory curve to the SLC data. The solid curve is the fit obtained from the SLC data. The dotted line is the theory curve before the e^+e^- and $\mu^+\mu^-$ data were included in the fit. The data selected are: (a) protons, (b) minimum ionizing pions, (c) cosmic rays, (d) $\mu^+\mu^-$ pairs, and (e) e^+e^- pairs.

extend out past the magnet coil. A photomultiplier tube is optically coupled to the end of each light guide.

Each phototube channel has two Time-to-Amplitude Converters (TACs) and a pulse height integrator. The analog times and pulse integrals are collected from each phototube channel and digitized. The timing acceptance window is 60 ns. The measured times from each phototube are corrected for the time the light propagates through the scintillator and for delays through the phototube. The particle's time-of-flight is obtained by taking the weighted average of the times from both phototubes.

Particle identification is determined from the velocity $\beta = L/ct$. The path length L from the IP is determined from the CDC and t is the measured time-of-flight. The squared mass of the particle is given by $m^2 = p^2[1/\beta^2 - 1]$ where p is the particle momentum measured by the CDC.

Performance

As determined from Bhabha events at PEP, the single counter resolution varies from 180 to 250 ps; averaging over all counters and data runs gives 221 psec. Figure 28 shows the difference between the expected time of arrival for the events and the time measured by the TOF system and Figure 29 shows the resulting $\pi/K/p$ separation.

At the SLC, the TOF measurement errors are non-Gaussian, due to accelerator backgrounds contributing to early times. They can be parameterized by a Gaussian distribution with an extended tail [21]. Using high momentum tracks ($\beta \simeq 1$) and minimally ionizing pions, this distribution function is fit to the data, as shown in Figure 30. More details can be found in Reference [21]. The resulting resolution is about 350 ps.

Due to the Loma Prieta earthquake, more than half of the TOF counters suffered cracked glue joints between the scintillator and light guides. As a result, the amount

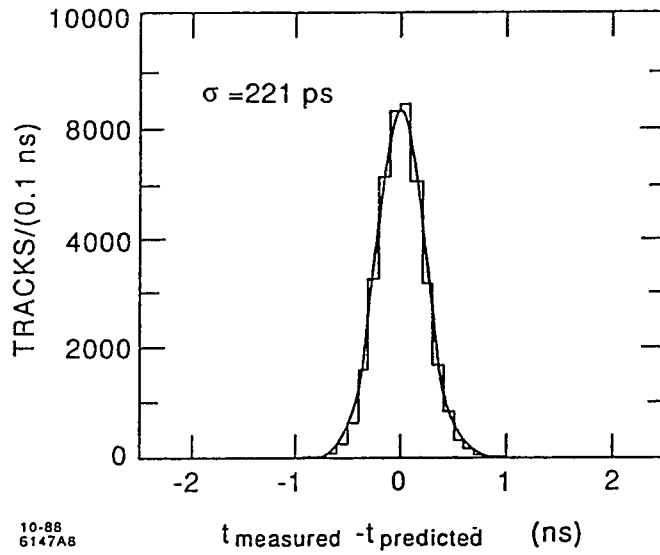


Figure 28: Time resolution for the Time of Flight system as measured at PEP.

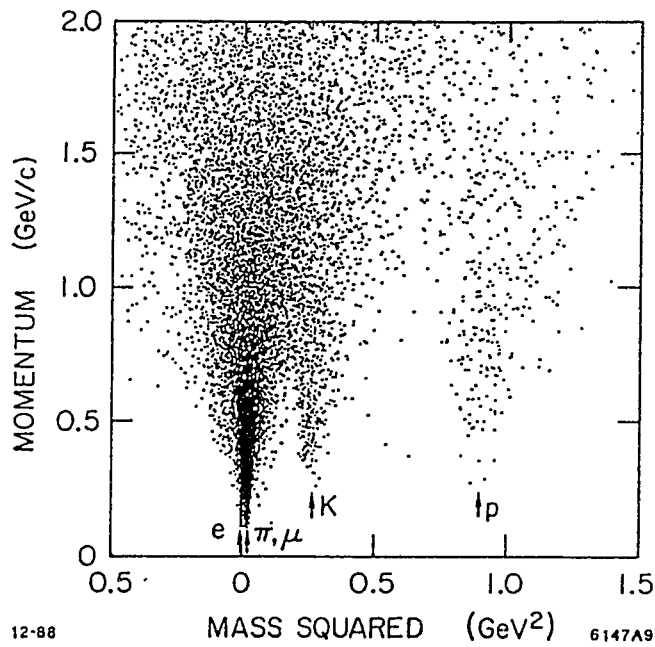
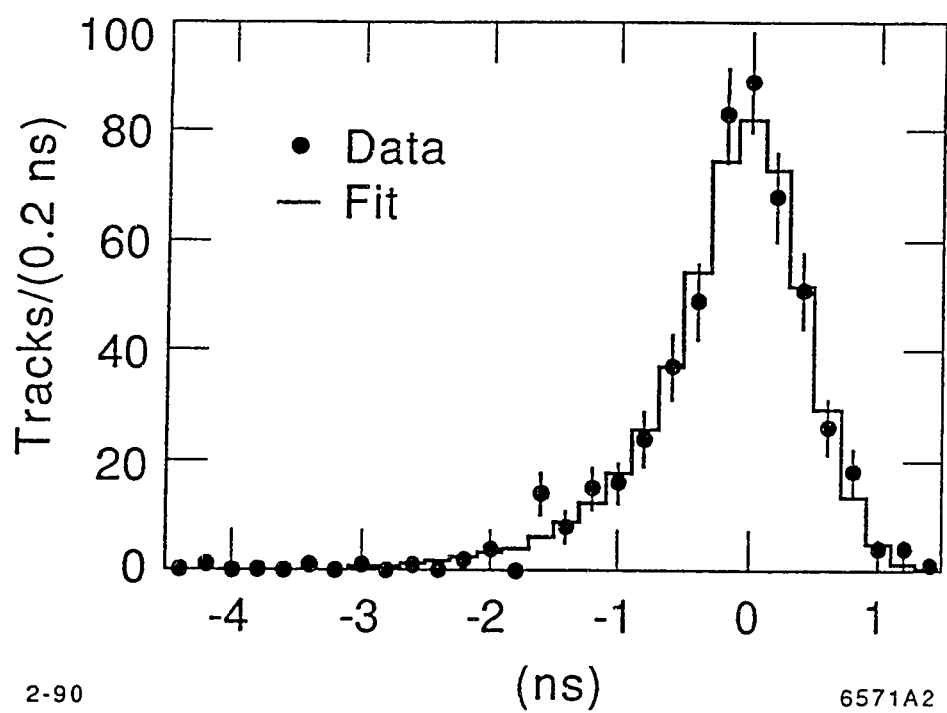


Figure 29: The $\pi/K/p$ separation as measured at PEP using the TOF.



2-90

6571A2

Figure 30: TOF resolution as measured at the SLC.

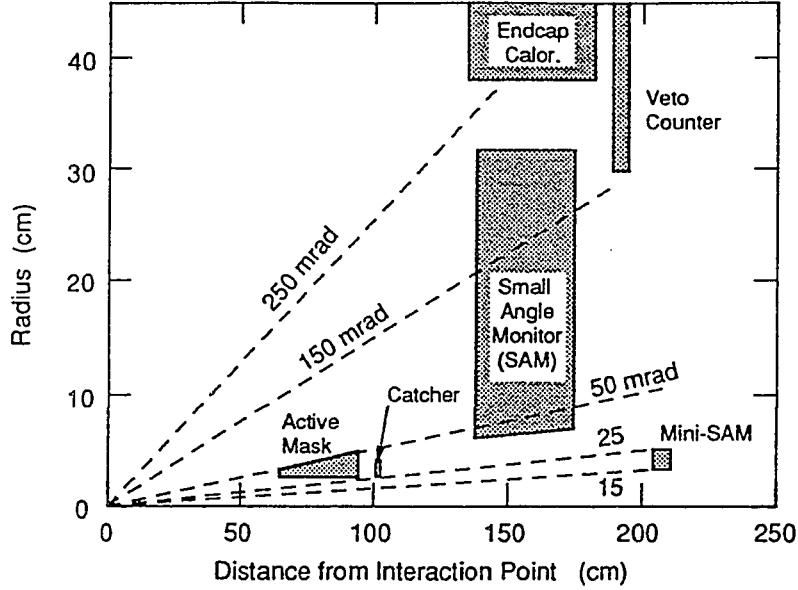


Figure 31: Schematic view of the SAM and Mini-SAM.

of light collected by the phototubes is reduced by about 25%. The resolution is degraded to about 500 ps.

3.2.4 Luminosity Monitors

The luminosity of the SLC is monitored by counting small-angle Bhabha scattering events detected by the Small Angle Monitor (SAM) and the Mini-Small Angle Monitor (Mini-SAM). The SAM covers the angular range $50 \text{ mrad} < \theta < 160 \text{ mrad}$, and the Mini-SAM covers $15 \text{ mrad} < \theta < 25 \text{ mrad}$. They are shown schematically in Figure 31.

Small Angle Monitor (SAM)

The SAM is a system of four modules, two each at $z = \pm 1.38$ m from the interaction point. Each module has a tracking section of 9 layers of drift tubes, followed by a calorimeter section of 6 layers of lead and proportional tubes (see Figure 32). A tungsten mask at 50 mrad sets precisely the low angle acceptance of the SAM.

The tracking section uses 9.5 mm square aluminum drift tubes with gas (89% Ar, 10% CO₂, 1% CH₄) at a pressure of about one atmosphere. A 38 μ m gold-plated tungsten wire is strung through the center of each tube, and carries a voltage of 1.8 kV with respect to the outer wall, which is at ground. Each layer has 30 tubes. The first layer is oriented horizontally; the next two layers are rotated $\pm 30^\circ$ with respect to the first. This pattern is repeated for the remaining layers.

The calorimeter consists of alternating layers of 13.2 mm thick lead and proportional tubes. These tubes are the same as the tracking tubes, but are held at 1.7 kV. Each SAM module has a thickness of 14.3 radiation lengths.

Performance

The system was tested in a positron beam with energies between 5 and 15 GeV [22]. The energy resolution can be parameterized by $\sigma(E)/E = 45\%/\sqrt{E}$ (E in GeV), and the tracking angular resolution is 0.2 mrad. Due to machine backgrounds from the SLC, there were times when the SAM tracking section could not be used. In this case, the calorimeter section measured the angles of the tracks with a resolution of 1 mrad. The energy resolution for Bhabhas at the SLC is measured to be 15% [23].

The cross section for SAM Bhabhas is about 20% greater than the visible Z^0 cross section. The systematic error on the luminosity measurement is approximately 2%. Details of the event selection and systematic errors for the SAM can be found in Reference [23].

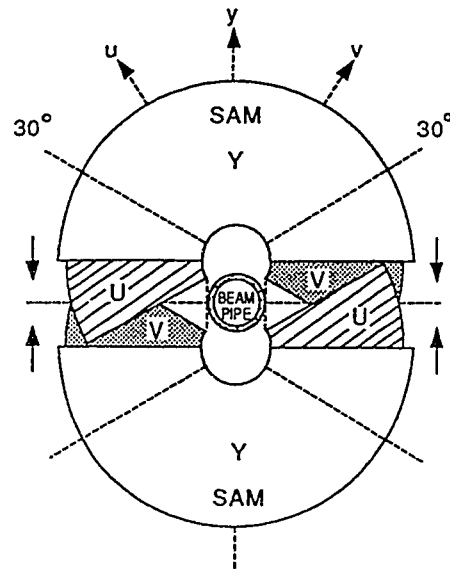
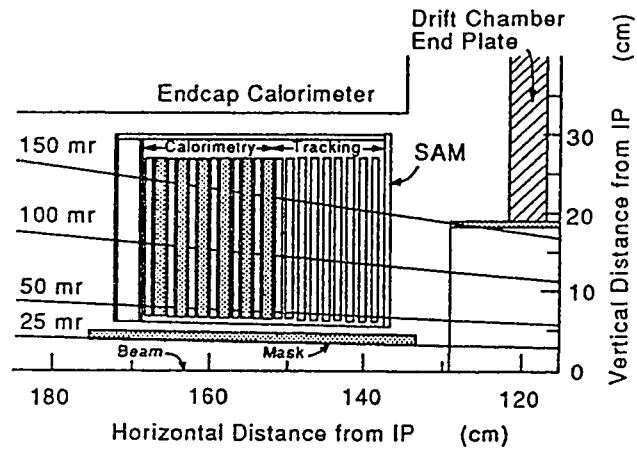


Figure 32: Side and front views of the Small Angle Monitor.

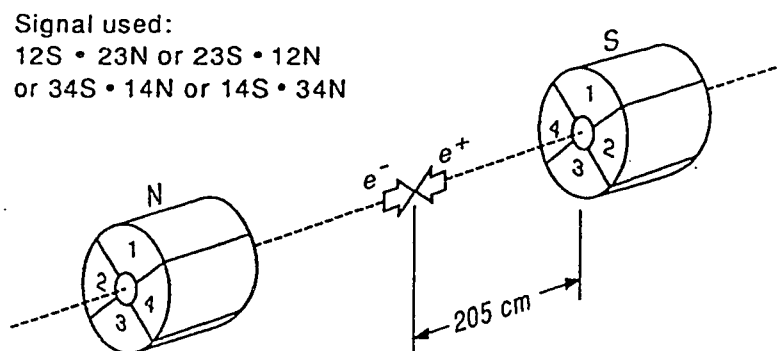


Figure 33: Geometry of the Mini-Small Angle Monitor.

Mini-Small Angle Monitor

The Mini-SAM is a system of two modules, each surrounding the beampipe at $z = \pm 2.05$ m from the IP. The modules consist of six alternating layers of 0.79 cm thick tungsten and 0.64 cm thick scintillator, totalling 15 radiation lengths. Two layers of tungsten in front of the first scintillator layer act as a pre-radiator, adding 4.5 radiation lengths of material. The modules are divided into four azimuthal sections, as shown in Figure 33. Each section is read out with a photomultiplier tube. The tube views a wavelength shifter bar which runs the length of each section.

Two conical masks of 5.08 cm thick tungsten define the angular acceptance. The masks are asymmetric, to allow for motion of the IP without losing acceptance. On one side of the IP, the angular acceptance is $15.2 \text{ mrad} < \cos \theta < 25.0 \text{ mrad}$ and $16.2 \text{ mrad} < \cos \theta < 24.5 \text{ mrad}$ on the other.

Performance

The expected energy resolution of the Mini-SAM is $\sigma(E)/E \approx 35\%/\sqrt{E}$ (E in

GeV), from test beam studies of a prototype model. The high backgrounds at the SLC decreased the Mini-SAM efficiency for identifying Bhabha events. This effect is discussed in detail in Reference [23].

Due to errors in the alignment of the acceptance masks, there are large uncertainties in the absolute cross-section of Bhabhas into the Mini-SAM. For this reason, the Mini-SAM can only be used as a relative luminosity monitor over an energy scan, whereas the SAM can measure absolute luminosity.

3.2.5 Trigger

At the SLC, the beam crossing rate is 10, 30, 60, or 120 Hz. This allows enough time between beam crossings to run the trigger logic on every crossing and decide whether that crossing has an event which is interesting enough to process and save. The trigger system receives a beam crossing signal from fast electrodes which detect the particle bunches passing them. They are situated at 13.6 m on either side of the IP. A CAMAC-based Master Interrupt Controller (MIC) module provides the interface between the trigger logic and the host VAX computer. Four separate types of events are processed and saved by the Mark II data trigger: data, luminosity, cosmic rays, and randoms.

Data trigger

The trigger for data events has two independent parts: the charged particle trigger and the SSP software trigger (SST [24]). The two triggers allows a redundancy in saving events and measurements of their relative efficiencies.

The charged particle trigger uses a fast track-finding processor [25] to find and count charged tracks in the central drift chamber (and DCVD). First, it determines which cells in the CDC have track segments. A cell is considered "hit" if four of the

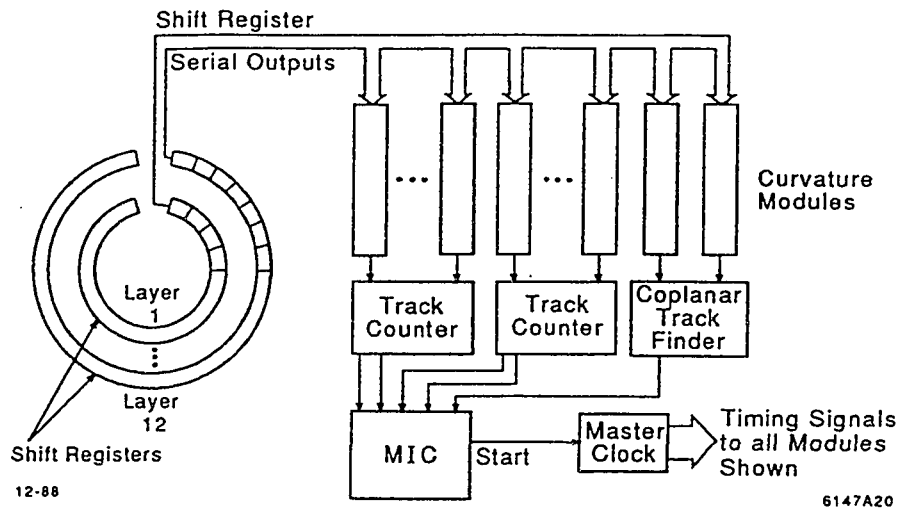


Figure 34: Block diagram of the charged track trigger.

six sense wires have TDC signals. The pattern of hits is loaded into shift registers. The registers are scanned by curve-fitting or “curvature” modules (see Figure 34). These modules are programmed to identify patterns of hits falling within a range of radii of curvature, in a “road” from the IP.

For this data set, the modules are programmed to require 8 out of the 10 first layers to have hits within a road, in order for that track to be counted as a “found” track. In order to travel 8 layers, a track must have $|\cos\theta| < 0.75$. “Found” tracks within 10° in azimuth of each other are considered to be one track. Track counters also record the total number of tracks found. The charged track trigger requires two charged tracks in order to log the event.

The SSP software trigger (SST) uses the energy depositions in the liquid argon and endcap calorimeters to determine a trigger, independent of the charged particle trigger. A SLAC scanner processor (SSP) reads the summed energy for both calorimeters and looks for clusters of energy deposition which point back to the IP.

The SST program requires at least one cluster greater than 3.3 GeV in the EC or at least one cluster greater than 2.2 GeV in the LA calorimeter.

Luminosity trigger

Bhabha scattering events in the SAM and Mini-SAM also trigger a data readout. The SAM trigger is an analog sum of the energy deposited in the SAM calorimeter layers. For each module, there is a sum for the front half, back half, and entire module. The event is triggered if there is 4 GeV in half a module, or 7 GeV in the entire module for both north and south SAM modules. This trigger is essentially 100% efficient.

Similarly, the Mini-SAM trigger makes analog sums of the total energy deposited in each of the north and south Mini-SAM modules. The trigger requires at least 20 GeV in both modules for it to log the event.

Cosmic ray trigger

Cosmic rays are used to test and evaluate the performance of the individual detector components. Cosmic rays are identified by combining the charged particle trigger system of the central drift chamber with a signal from the TOF system. This provides an absolute time measurement for the charged trigger electronics and drift chamber reconstruction software. Cosmic ray events also allow checks of the charged particle trigger performance.

Random trigger

To monitor accelerator backgrounds and noise in the detector, the Mark II is read out for a number of random beam crossings. These events are used to estimate detector response when no annihilation occurs.

3.2.6 Data Acquisition

The data acquisition system is controlled by a number of processes running on a VAX 8600 computer. These processes include: reading CAMAC and FASTBUS data; merging raw data with the results for online event tagging; logging events to tape; logging tagged events to disk; monitoring detector performance, electronics, and environmental status; performing online analysis and histogramming; and operator control of the experiment.

CAMAC and FASTBUS interfaces provide detector data to the VAX. The CAMAC interface is a VAX CAMAC channel (VCC [26]). The VCC monitors two system crates, which in turn connect with the 44 data acquisition crates (see Figure 35). It reads out the memories of the BADCs in each crate or instrumentation modules and formats the data. The VCC is capable of a data transfer rate of 1 Mbyte/sec over a UNIBUS.

The FASTBUS interface is a 32-bit parallel port connecting to the FASTBUS crate segment through a simple buffer module (BAFFO) (see Figure 19). The interface can transfer data at a rate of approximately 5.5 Mbytes/sec between the VAX and an SSP. Remote SSPs perform local data readout and processing on an event, and then report to their system SSP. A master SSP receives the data for the entire event and then interrupts the VAX to ship the event in a single block read.

At every beam crossing, a signal is generated which starts the trigger logic and BADC processing. If a trigger occurs, the CAMAC and FASTBUS systems are read out. The trigger is reset when the master SSP signals that FASTBUS is ready for the next event.

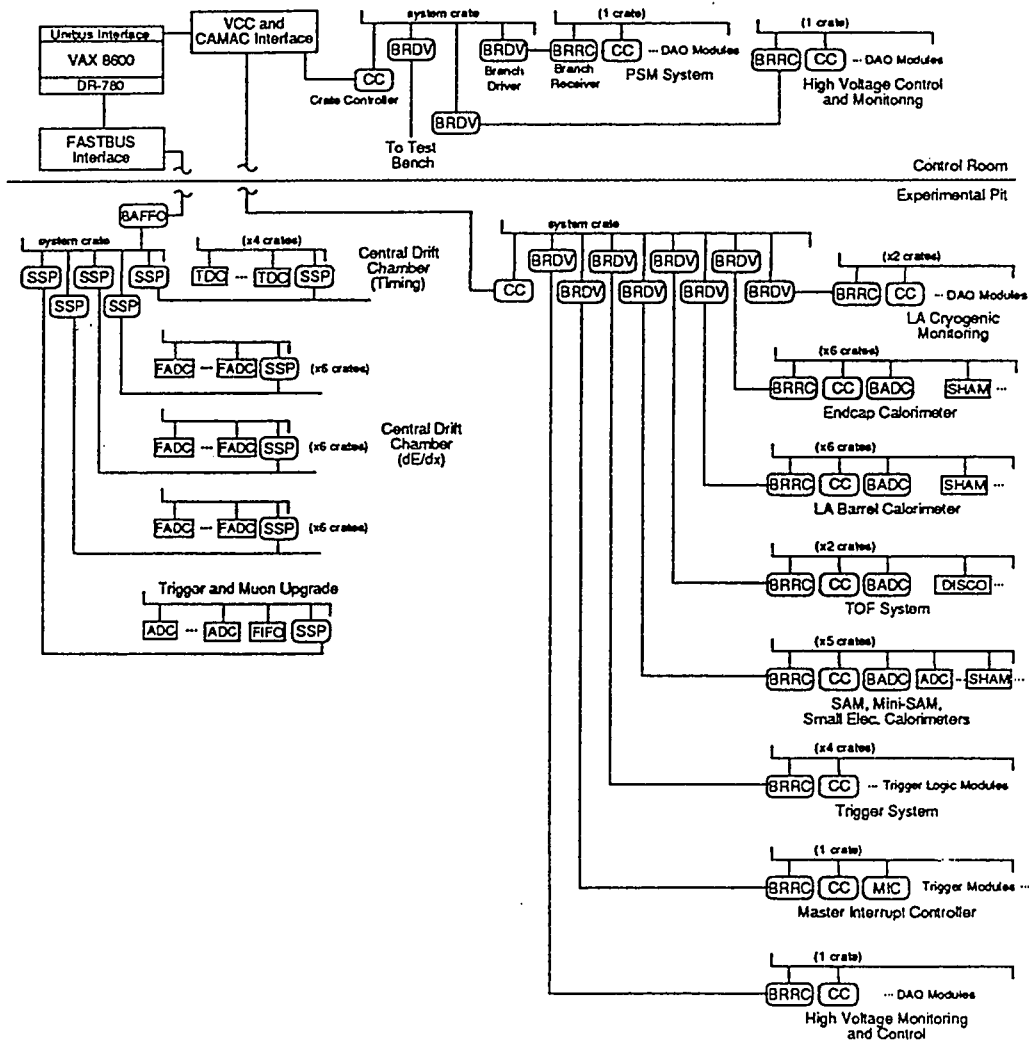


Figure 35: FASTBUS and CAMAC system of the Mark II data acquisition system.

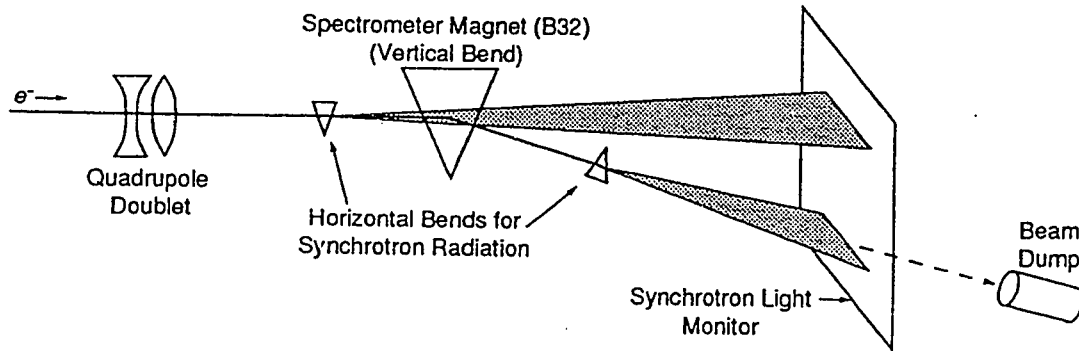


Figure 36: Layout of the extraction line spectrometer system.

3.3 Extraction Line Spectrometer

To map out the Z^0 resonance peak as a function of the center-of-mass energy, E_{cm} , the energy of each beam, E_{beam} , has to be measured precisely. A spectrometer [27] in each extraction line measures the energy of each beam before the beam dumps. A schematic layout of the extraction line energy spectrometer is shown in Figure 36.

The spectrometer gives a pulse-to-pulse measurement of E_{cm} . The beam enters the spectrometer and passes through three dipole magnets. The first magnet sweeps the beam horizontally, creating a swath of synchrotron radiation at the position of the monitor. The second magnet bends the beam vertically by an amount proportional to $\int Bdl/E_{beam}$, and the third magnet sweeps the beam horizontally again, creating a second swath of radiation. The beam energy can be calculated from the measured distance between the stripes, the distance to the second magnet, and its magnetic strength. An accuracy of 35 MeV on E_{beam} has been achieved [28].

Chapter 4

Kinematics of Two-Photon Reactions

Classically, light waves add together by superposition; they may not scatter. However, in quantum electrodynamics (QED), the uncertainty principle allows a photon of energy E_γ to create a pair of virtual charged particles (see Figure 37) with mass m_{pair} . The lifetime of this intermediate state is [29]

$$\Delta t \approx 2E_\gamma/m_{pair}^2$$

For a high photon energy, this lifetime is long, and the photons “scatter” because of the interaction of the virtual particles (see Figure 38).

This nonlinear result was first explored by Euler and Kockel [30] in 1935; Landau and Lifshitz [31] and Williams [32] studied the interaction $e^+e^- \longrightarrow e^+e^-l^+l^-$ over fifty years ago.

Since sources of high energy photon beams which can produce photon-photon

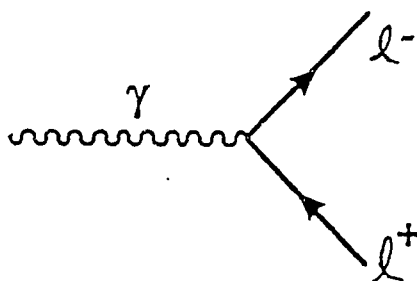


Figure 37: Quantum fluctuation of a photon into a pair of charged particles.

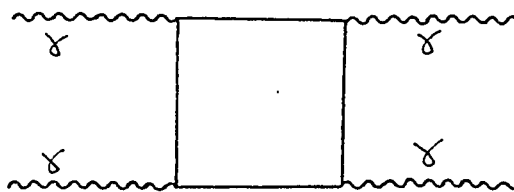


Figure 38: Box diagram for elastic $\gamma\gamma$ scattering.

collisions at the intensities needed for experimental studies do not exist, the interactions of *virtual* photons are instead studied at high energy electron-positron colliders. High energy electrons (positrons) can radiate photons with a lifetime of order $\Delta t \sim E_b/(m_e p_T)$ where E_b is the beam energy and p_T is the photon's transverse momentum relative to the beam direction. As a result of time dilation, this lifetime is longer than typical reaction times ($\sim 10^{-23}$ sec) [33]. Therefore, the photons scatter as though they were real particles. The basic diagram is shown in Figure 39.

4.1 The kinematics of $e^+e^- \rightarrow e^+e^-l^+l^-$

Particle production in two-photon collisions is shown in Figure 39. A high energy electron and positron each radiate a photon; the two photons subsequently interact. As was described in Chapter 2, this is not the only diagram contributing to this reaction; however, in the cases studied herein, where the final electron and positron are *not* tagged, it is the dominant one. When either the electron or positron are tagged, the other diagrams mentioned in Chapter 2 also contribute. However, because those cases are not studied here, and for simplicity's sake, the kinematics for the multiperipheral diagram only will be discussed below.

As was discussed in Section 2.1.3, the photon propagators in Figure 39 are similar to those arising in Bhabha scattering. The photons tend to be emitted mostly at small angles, of the order m_e/E_b with respect to the beam, resulting in small momentum transfers to the lepton pair. Also, the radiated photons are similar to bremsstrahlung radiation. Thus, the photon spectrum would be expected to behave as the bremsstrahlung spectrum ($\sim 1/E_\gamma$), peaking at low photon energies. As a result, most of the final state lepton pairs will have small invariant masses, and will be boosted along the the beam direction.

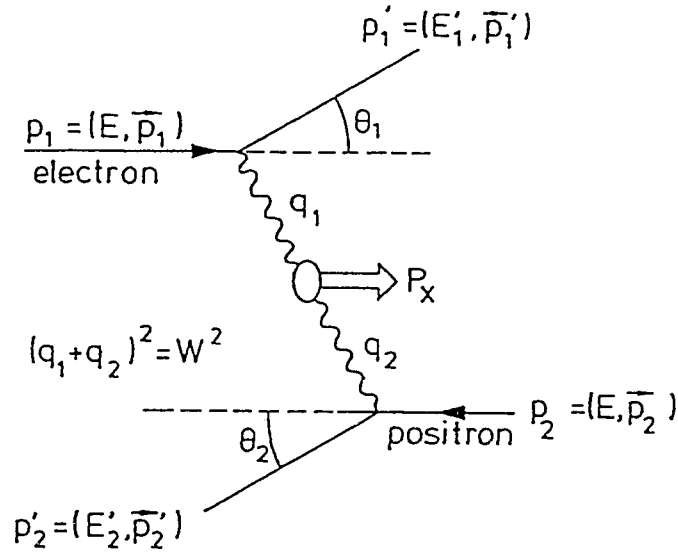


Figure 39: Kinematics of the general two-photon process.

Useful kinematic variables are defined below (see also Figure 39).

E_b	the electron (positron) beam energy.
p_i	the beam electron (positron) four-momenta ($i = 1, 2$).
p'_i	the scattered electron (positron) four-momenta.
$E'_i \equiv p'^0_i$	energies of the scattered electron (positron).
θ_i	the polar angles of the scattered electron (positron) (with respect to the beam axis).
ϕ_i	the azimuthal angles of the scattered electron (positron) (with respect to the beam axis).
$q_i = p_i - p'_i$	momenta of the virtual photons.
$E_{\gamma i} = q_i^0$	energies of the photons.
$\omega_i = E_{\gamma i}/E_b$	energies of the photons relative to the beam energy.

$$Q_i^2 \equiv -q_i^2$$

$$W_{\gamma\gamma} = \sqrt{(q_1 + q_2)^2} \quad \text{invariant mass of the final lepton pair.}$$

$$Z \equiv W_{\gamma\gamma}/2E_b$$

$$y = \tanh^{-1} \beta \quad \text{rapidity of the } \gamma\gamma \text{ system in the lab frame.}$$

The kinematics of the reaction $e^+e^- \rightarrow e^+e^-l^+l^-$ is determined by the four-momenta of the incoming, and subsequently scattered, electron and positron (p_i and p'_i). The z axis is defined by the incoming beams; at the SLC, the two incoming beams collide head-on, and the energy for each beam is roughly half the mass of the Z^0 boson ($M_Z = 91.1$ GeV). For unpolarized beams, there is no overall azimuthal dependence. In this case, only five variables are needed to determine the $\gamma\gamma$ system for the given beam energy, E_b . These five variables (as defined in the laboratory system) are:

- the energies E'_1, E'_2 of the scattered electron and positron,
- the angles θ_1, θ_2 with respect to the beam axis made by the scattered electron and positron,
- the angle Φ which subtends the planes made by the scattering electron and positron.

In terms of these variables, the energies of the virtual photons are

$$E_{\gamma i} = E - E'_i \quad (65)$$

$$\omega_i = E_{\gamma i}/E_b \quad (66)$$

and the photon invariant masses are

$$\begin{aligned}
 q_1^2 &= -Q_1^2 = (p_1 - p'_1)^2 \\
 &= 2m_e^2 - 2E_b E'_1 (1 - \sqrt{1 - (m_e/E_b)^2} \sqrt{1 - (m_e/E'_1)^2} \cos \theta_1) \\
 q_2^2 &= -Q_2^2 = (p_2 - p'_2)^2 \\
 &= 2m_e^2 - 2E_b E'_2 (1 - \sqrt{1 - (m_e/E_b)^2} \sqrt{1 - (m_e/E'_2)^2} \cos \theta_2).
 \end{aligned} \tag{67}$$

For small scattering angles (ie., no-tagging), the mass of the electron may not be neglected with respect to the energy of the beam. Letting $\theta'_i = 0$, the minimum possible value of Q_i^2 is

$$Q_{i_{\min}}^2 = m_e^2 \frac{\omega^2}{1 - \omega} + O(m_e^4). \tag{68}$$

The invariant mass of the $\gamma\gamma$ system (lepton pair l^+l^-) is

$$\begin{aligned}
 W_{\gamma\gamma}^2 &= (q_1 + q_2)^2 \\
 &= 4E_{\gamma 1} E_{\gamma 2} - 2E'_1 E'_2 (1 - \cos \theta_1 \cos \theta_2 - \sin \theta_1 \sin \theta_2 \cos \Phi)
 \end{aligned} \tag{69}$$

where $\cos \theta_1 \cos \theta_2 + \sin \theta_1 \sin \theta_2 \cos \Phi$ is the cosine of the angle between the scattered electron and positron. For untagged events, where the electron and positron are scattered into small angles, the invariant mass $W_{\gamma\gamma}$ is approximately

$$W_{\gamma\gamma} \approx 4E_{\gamma 1} E_{\gamma 2}. \tag{70}$$

4.2 Cross sections (the general case)

The reaction shown in Figure 39 can be viewed as a composite of three parts: the electron-photon vertex, the positron-photon vertex, and the $\gamma\gamma \rightarrow l^+l^-$ process. A single electron-photon vertex is shown in Figure 40. It contributes the factor $\bar{u}(p', s')(-ie\gamma_\mu)u(p, s)$ to the scattering amplitude, according to the usual QED Feynman rules (see Ref. [5]). The factor $u(p, s)$ is the momentum-space spinor for a free

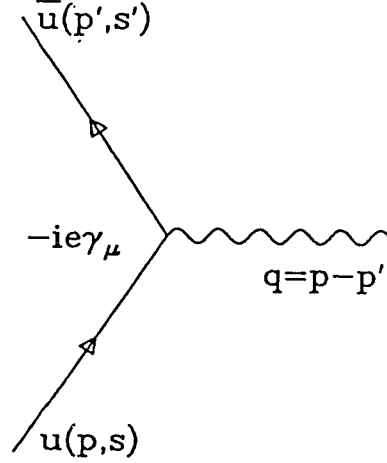


Figure 40: Feynman electron-photon vertex.

electron with momentum p and spin s . Similarly, the positron-photon vertex will contribute a factor $\bar{v}(p', s')(-ie\gamma_\nu)v(p, s)$, where the factor $v(p, s)$ is the momentum-space spinor for a free positron. The electron-photon and positron-photon vertices determine the fluxes and polarization states of the two photons. Then, the transition matrix element T for the $\gamma\gamma \rightarrow l^+l^-$ process depends on the polarization states of the two photons as determined by the polarization vectors ϵ_1 and ϵ_2 ,

$$T = \epsilon_1^\mu \epsilon_2^\nu A_{\mu\nu}^{l^+l^-} \quad (71)$$

where $A_{\mu\nu}^{l^+l^-}$ is a tensor describing the helicity structure of the process $\gamma\gamma \rightarrow l^+l^-$. Due to conservation of electromagnetic current, the photon polarization can be described by a 3-vector $\vec{\epsilon}_i$. As a result, the polarization states of a photon can be described by a 3×3 density matrix $\rho_i^{\mu\nu}$ ($i = 1, 2$ for the two photons).

Budnev *et al.* [34] have worked out the polarization density matrices to be

$$\rho_i^{\mu\nu} = -[q_i^2 g_{\mu\nu} + 2(p_i'^\mu p_i^\nu + p_i^\mu p_i'^\nu)]/q_i^2. \quad (72)$$

Then, the differential cross section for the reaction $e^+e^- \rightarrow \gamma\gamma l^+l^-$ can be written as [34]

$$d\sigma = \frac{\alpha^2}{64\pi^4 E_b^2 q_1^2 q_2^2} \rho_1^{\mu\nu} \rho^{\alpha\beta} M_{\mu\nu\alpha\beta}^{l^+l^-} \frac{d^3 p'_1 d^3 p'_2}{E'_1 E'_2}. \quad (73)$$

The tensor $M_{\mu\nu\alpha\beta}^{l^+l^-}$ is given (in general) by

$$M_{\mu\nu\alpha\beta}^{l^+l^-} = 8\pi^2 \int A_{\mu\nu}^{*l^+l^-} A_{\alpha\beta}^{l^+l^-} \delta(q_1 + q_2 - \sum_i k_i) d\Gamma_f \quad (74)$$

where $\sum_i k_i$ is the total momentum of the l^+l^- pair and Γ_f is the final state phase space.

Budnev *et al.* [34] have expressed the cross section above in terms of the cross section for photons with given helicities. Then, Equation 74 becomes (for unpolarized beams)

$$\begin{aligned} d\sigma = & \frac{\alpha^2 \sqrt{(q_1 q_2)^2 - q_1^2 q_2^2}}{16\pi^4 E_b^2 q_1^2 q_2^2} \times \frac{d^3 p'_1 d^3 p'_2}{E'_1 E'_2} \times \\ & \times 4\rho_1^{++} \rho_2^{++} \sigma_{TT} + 2\rho_1^{++} \rho_2^{00} \sigma_{TL} + 2\rho_1^{00} \rho_2^{++} \sigma_{LT} + \rho_1^{00} \rho_2^{00} \sigma_{LL} \\ & + 2|\rho_1^{+-} \rho_2^{+-}| \tau_{TT} \cos 2\tilde{\phi} - 8|\rho_1^{+0} \rho_2^{+0}| \tau_{TL} \cos 2\tilde{\phi} \end{aligned} \quad (75)$$

where $\tilde{\phi}$ is the angle between the scattering planes of the original electron and positron as seen in the $\gamma\gamma$ center-of-mass system, and the σ 's are the cross sections for interactions of unpolarized transverse photons (T) with helicities ± 1 , or for longitudinal photons (L) with helicity zero. The term τ_{ab} is a correlation between transverse and longitudinal photons; when $d\sigma$ is integrated over the azimuthal angle, these terms disappear. The density matrix elements, ρ_i^{ab} , are given in Equation (5.13) of Ref. [34]. For *untagged* events, only the factors ρ_1^{++} and ρ_2^{++} are important; they are given by

$$\rho_1^{++} = \frac{1}{2} \left[\frac{(2p_1 \cdot q_2 - q_1 \cdot q_2)^2}{(q_1 \cdot p_2)^2 - q_1^2 q_2^2} + 1 + \frac{4m_e^2}{q_1^2} \right] \quad (76)$$

$$\rho_2^{++} = \rho_1^{++} (1 \rightarrow 2). \quad (77)$$

4.3 The photon luminosity function

For most experimental situations, the complicated formula for the cross section in Equation 75 can be simplified. Due to the factors $1/q_1^2$ and $1/q_2^2$ in Equation 75, the cross section is dominated by photons which are almost real ($q_i^2 \rightarrow 0$). If the scattered electron and positron are not tagged, the *measured* cross section will be dominated by these photons. Then, an approximate form of the cross section will contain only contributions from transverse photons. This means that in Equation 75, only the terms with σ_{TT} and τ_{TT} survive. When $d\sigma$ is integrated over the azimuthal angle, the τ_{TT} term also disappears. Therefore, the cross section becomes approximately

$$d\sigma = \frac{\alpha^2 \sqrt{(q_1 q_2)^2 - q_1^2 q_2^2}}{16\pi^4 E_b^2 q_1^2 q_2^2} \frac{d^3 p'_1 d^3 p'_2}{E'_1 E'_2} 4\rho_1^{++} \rho_2^{++} \sigma_{TT}. \quad (78)$$

Defining

$$L_{TT} = 4 \frac{\alpha^2 \sqrt{(q_1 q_2)^2 - q_1^2 q_2^2}}{16\pi^4 E_b^2 q_1^2 q_2^2} \rho_1^{++} \rho_2^{++} \quad (79)$$

allows Equation 78 to be written as

$$d\sigma = \sigma_{TT} L_{TT} \frac{d^3 p'_1}{E'_1} \frac{d^3 p'_2}{E'_2}. \quad (80)$$

L_{TT} is the “transverse-transverse photon luminosity function” [35], and $\sigma_{TT} = \sigma_{\gamma\gamma}$ is the cross section for the reaction $\gamma\gamma \rightarrow l^+l^-$.

4.4 Approximations

In the general case, the ρ_i^{++} 's are functions of variables of both photons (see Equation 77). However, for $q_i^2 \rightarrow 0$, and $Q_i^2 \ll W_{\gamma\gamma}^2$, this photon luminosity function can be written as a product of two photon fluxes where each flux depends on the variables of only one photon. For small Q_i^2 , $W_{\gamma\gamma} \approx 4E_{\gamma 1} E_{\gamma 2}$ (see Equation 70). When

Equation 80 is integrated over the angles of the scattering electron and positron, the differential cross section becomes

$$d\sigma = \int_{\Omega_1 \Omega_2} L_{TT} \sigma_{TT} \frac{d^3 p'_1}{E'_1} \frac{d^3 p'_2}{E'_2} \quad (81)$$

$$d\sigma = f_{\gamma/e}(\omega_1) f_{\gamma/e}(\omega_2) d\omega_1 d\omega_2 \quad (82)$$

where ω_1 and ω_2 are as previously defined in Section 4.2, and $f_{\gamma/e}$ is given by

$$f_{\gamma/e}(\omega_i) = \frac{\alpha}{2\pi\omega_i} \{ [1 + (1 - \omega_i)^2] \ln\left(\frac{Q_{max}^2}{Q_{min}^2}\right) - 1 + \omega_i \}. \quad (83)$$

The quantity, $f_{\gamma/e}(\omega_i) d\omega_i$ is the number of almost real photons radiated from the i th vertex. Notice that the luminosity function L_{TT} is now a product of two factors, $f_{\gamma/e}(\omega_1)$ and $f_{\gamma/e}(\omega_2)$, which each contain only variables of their respective photons.

For the case where the scattered electron and positron are not detected (untagged), $Q_{min}^2 = m_e^2 \omega / (1 - \omega)$, as described in Section 4.1. Q_{max}^2 is given by Equation 67 evaluated at $\theta' = \pi$ (i.e. $Q_{max}^2 = 4E_b E'$). Substituting these values into the expression for $f_{\gamma/e}$ and keeping leading terms gives

$$f_{\gamma/e}(\omega_i) = \frac{\alpha}{\pi} \omega_i^{-1} [1 + (1 - \omega_i)^2] \ln\left(\frac{E_b}{m_e}\right) \quad (84)$$

for untagged events.

Since $W_{\gamma\gamma}^2 \approx 4E_{\gamma 1} E_{\gamma 2} = 4E_b^2 \omega_1 \omega_2$ as stated earlier, and $Z \equiv W_{\gamma\gamma} / 2E_b$ as defined in Section 4.1, then the integration over the photon energies has the additional constraint that $Z^2 = \omega_1 \omega_2$. Introducing the factors

$$\tilde{s} = Z^2 = \omega_1 \cdot \omega_2 \quad (85)$$

$$\tilde{r} = \omega_1 / \omega_2 \quad (86)$$

gives for the *total* cross section

$$\sigma = \int f_1 f_2 \frac{\partial(\omega_1, \omega_2)}{\partial(\tilde{r}, \tilde{s})} d\tilde{r} d\tilde{s} \sigma(\tilde{s}) d\tilde{s} = \int L_{\gamma\gamma}(\tilde{s}) \sigma_{\gamma\gamma}(\tilde{s}) d\tilde{s} \quad (87)$$

where $L_{\gamma\gamma}$ is defined as

$$L_{\gamma\gamma} = \int f_1(\omega_1) f_2(\omega_2) \frac{\partial(\omega_1, \omega_2)}{\partial(\tilde{r}, \tilde{s})} d\tilde{r}. \quad (88)$$

For the case where the scattered electron and positron are not detected (untagged), $L_{\gamma\gamma}$ is given by

$$L_{\gamma\gamma} = \left(\frac{2\alpha}{\pi}\right)^2 \left\{ \ln\left(\frac{E_b}{m_e}\right) \right\}^2 \frac{1}{2\tilde{s}} f(\tilde{s}) \quad (89)$$

where

$$f(\tilde{s}) = \frac{1}{2}(2 + \tilde{s})^2 \ln(1/\tilde{s}) - (1 - \tilde{s})(3 + \tilde{s}) \quad (90)$$

is the ‘‘Low function’’.

This factorization of the luminosity function is called the ‘‘equivalent photon approximation’’ (EPA) for two-photon production. Basically, the approximation replaces the incoming electron and positron beams with the appropriate equivalent fluxes of real photons.

4.5 QED cross sections

The preceding section outlined the kinematics and approximations leading to an expression for the cross section of the reaction $e^+e^- \rightarrow e^+e^-l^+l^-$ given by

$$\sigma = \int L_{\gamma\gamma}(\tilde{s}) \sigma_{\gamma\gamma}(\tilde{s}) d\tilde{s} \quad (91)$$

with the luminosity function $L_{\gamma\gamma}$ given by the equivalent photon approximation. To calculate cross sections and angular distributions, the luminosity function must be combined with the cross section for the reaction $\gamma\gamma \rightarrow l^+l^-$. The differential and total cross sections for this reaction are given by

$$d\sigma/d\cos\theta^* = \frac{2\pi\alpha^2}{W_{\gamma\gamma}^2} \beta^* [2\beta^{*2} \sin^2\theta^* - \beta^{*4} \sin^4\theta^* + 1 - \beta^{*4}] / (1 - \beta^{*2} \cos^2\theta^*)^2 \quad (92)$$

l	e	μ	τ
$\sigma_{ee \rightarrow eell}$ (nb)	26×10^6	3×10^2	6×10^{-1}

Table 10: The total two-photon production cross section for the different leptons (e, μ, τ).

and

$$\sigma = \frac{2\pi\alpha^2}{W_{\gamma\gamma}^2} [2\beta^{*3} - 4\beta^* + (3 - \beta^{*4})] \ln\left\{\frac{1 + \beta^*}{1 - \beta^*}\right\}. \quad (93)$$

The quantities β^* and θ^* are defined in the $\gamma\gamma$ center of mass system: β^* is the velocity of a lepton and θ^* is the polar angle with respect to the $\gamma\gamma$ direction. In this system, each lepton has an energy of $E_l = W_{\gamma\gamma}/2$; therefore, β^* is given by

$$\beta^* = \left[1 - \frac{4m_l^2}{W_{\gamma\gamma}^2}\right]^{1/2}. \quad (94)$$

This expression is used for β^* in Equation 93, then substituted into Equation 91, giving a formula for the total cross section as an integral over $\tilde{s} = W_{\gamma\gamma}^2/4E_b^2$. At the lower threshold, $W_{\gamma\gamma} = 2m_l$, where m_l is the mass of the lepton produced by the two-photon interaction; at the upper limit, $W_{\gamma\gamma} = 2E_b$. Therefore, \tilde{s} runs from m_l^2/E_b^2 to 1. Upon integrating, the result for the total cross section is [7]

$$\sigma = \left(\frac{112\alpha^4}{9\pi m_l^2}\right) \left[\ln\left(\frac{E_b}{m_e}\right)\right]^2 \ln\left(\frac{E_b}{m_l}\right) \quad (95)$$

as stated in Section 2.1.3. Table 10 lists this cross section for $l = e, \mu, \tau$ at $E_b = 45$ GeV.

As shown by Equation 93, the maximum cross section arises from the minimum $W_{\gamma\gamma}$. In their paper, Brodsky, Kinoshita, and Terazawa [7] also discuss the angular

spread of the two-photon reaction. The leptons from the $\gamma\gamma$ interaction come out at broad angles, while the scattered electron (positron) are boosted forward in angle, and typically go down the beam pipe. Their results show that half of the cross section comes from events which have an electron (positron) scattering angle of

$$\theta'_{1/2} \leq (m_e/E_b)^{1/2} \quad (96)$$

and three-quarters of the cross section from events with

$$\theta'_{3/4} \leq (m_e/E_b)^{1/4}. \quad (97)$$

For the SLC beam energy of approximately 45 GeV, these angles are

$$\begin{aligned} \theta'_{1/2} &\leq 3.3 \times 10^{-3} \text{ radians} \\ \theta'_{3/4} &\leq 5.8 \times 10^{-2} \text{ radians} \end{aligned}$$

Therefore, three-quarters of the total cross section comes from events which have the electron scattering at a polar angle less than 58 milliradians, or 3.3 degrees, with respect to the beam direction.

4.6 Experimental acceptances

As discussed above, two-photon events have two distinctive features:

- Most of the events have the original electron and positron scattered at extremely small angles.
- The cross section peaks at low $W_{\gamma\gamma}$; therefore, the lepton pairs tend to have low momenta.

As a function of beam energy, E_b , the total cross section given in Equation 93 goes as $\ln^3(E_b)$, while the annihilation process $ee \rightarrow \mu\mu$ goes as $1/E_b^2$. Thus, the two-photon

cross section is greater than the annihilation cross section for energies greater than approximately 1 GeV. However, the $\ln^3(E_b)$ dependence is due to the two features listed above; in general, the *observed* two-photon cross section is always smaller than the total two-photon cross section, and much smaller than the annihilation cross section.

The factor $\ln^2(E_b/m_e)$ directly arises from events where the electrons are scattered at very small angles ($\theta \sim m_e/E_b$). Small angle tagging so close to the beam line is very difficult for most high energy machines. In those machines which do have small angle taggers, Bhabha events would be tagged as well as the electron and positron from the two-photon events, making it hard to distinguish the two. Generally, tagging of the outgoing electron occurs at angles greater than m_e/E_b . Thus, the $\ln^2(E_b/m_e)$ factor is preserved under no tagging conditions. These are the conditions for this analysis.

The factor $\ln(E_b/m_l)$ is suppressed by the acceptance of the central detector [8]. This factor arises from the l^+l^- pairs whose β (in the lab frame) goes to 1, especially important for the $l = e$ case. In deriving the total cross section, β is integrated from 0 to

$$\beta_{max} = \frac{4E_b^2 - W_{\gamma\gamma}^2}{4E_b^2 + W_{\gamma\gamma}^2}. \quad (98)$$

Then integration over $W_{\gamma\gamma}^2$ from the threshold value $2m_l$ to $2E_b$ gives

$$\int_{2m_l}^{2E_b} \ln\left(\frac{2E_b}{W}\right) \cdot \frac{dW}{W^3} \sim \frac{1}{4m_l^2} \ln(E_b/m_l). \quad (99)$$

The central detector usually has a limited acceptance in the polar angle of either lepton produced: $\psi \leq \theta \leq \pi - \psi$, where ψ is the polar angle cut-off. This results in an acceptance function for β which depends on ψ ; it decreases as β increases, and becomes zero for $\beta \geq \cos \psi$. The derivation for this acceptance function is described

in Appendix A; the result is

$$\sigma \sim 2(\ln^2(\tan \psi/2) + \ln(\sin \psi))/W_0^2 \quad (100)$$

where W_0^2 is the effective pair threshold as seen in the detector.

This effective pair threshold arises from the triggering condition imposed by the detector and experiment. Typically, the trigger will require tracks to have transverse momenta greater than a momentum p_0 , set by the trigger. This results in an effective mass threshold $W_0 \geq 2\sqrt{m_l^2 + p_0^2} \gg 2m_l$. Thus, instead of a $1/m_l^2$ factor in the total cross section, there is a factor $1/(m_l^2 + p_0^2) < 1/m_l^2$.

The equivalent photon approximation has been greatly reviewed and discussed [7, 8, 34, 35]. More recently, computer programs have been written to directly integrate the exact differential cross section using Monte Carlo techniques. These programs have the ability to generate events according to the exact cross section, and then pass these events through a simulation of the detector. The Monte Carlo program used in this analysis was written by Berends, Daverveldt, and Kleiss [1], and is described in Chapter 5.

Chapter 5

Two-Photon Monte Carlo Simulation

The full leading-order calculations for these two-photon processes has been done using Monte Carlo integration by Berends, Daverveldt, and Kleiss [1]. Their program takes into account all diagrams which contribute to the cross section, as well as both photon and Z^0 exchanges to order α^4 .

5.1 Calculation of the two-photon cross section

Because the QED coupling constant α is small ($\approx 1/137$), cross sections for various QED interactions can be calculated using perturbation theory. The perturbation series can be represented by a series of Feynman diagrams which pictorially describe the interactions. “Summing” all possibly contributing diagrams gives the transition amplitude for the interaction in question. The square of the amplitude, when multiplied by the incident flux and phase space factors, summed over final spin states, and averaged over initial spin states, gives the differential cross section $d\sigma/d\omega$ for

the process. It is this theoretical cross section which is compared to that obtained experimentally.

The two-photon process $e^+e^- \rightarrow e^+e^-e^+e^-$ is described by 36 Feynman diagrams, each diagram having four electron-photon vertices. As more vertices per diagram are added, the calculation of the transition amplitudes for each diagram becomes extremely complex. Thus, Berends, Daverveldt, and Kleiss have developed numerical algorithms to calculate the amplitudes. The differential cross section for these processes is evaluated from the amplitudes according to

$$d\sigma = \frac{\alpha^4}{128\pi^4 E_{beam}^2} |M|^2 \delta^4(p_+ + p_- - q_+ - q_- - k_+ - k_-) \frac{d^3\vec{q}_+ d^3\vec{q}_- d^3\vec{k}_+ d^3\vec{k}_-}{q_+^0 q_-^0 k_+^0 k_-^0}.$$

The amplitude M of the interaction is equal to the sum of the transition amplitudes of all contributing diagrams. Here, p_+ and p_- are the incoming momenta of the positron and electron, and q_+, q_-, k_+, k_- are the momenta of the outgoing particles.

Before the spin sum and average, the transition amplitudes are calculated numerically. To streamline this calculation, the 36 contributing diagrams for the $e^+e^- \rightarrow e^+e^-e^+e^-$ process are systematically grouped. The differential cross section has many different peaks (657 in the $e^+e^- \rightarrow e^+e^-e^+e^-$ case); a set of integration variables appropriate for one peak is not necessarily appropriate for another. Berends *et al.*[1] divided the 36 diagrams into four groups.

The first group is the “multiperipheral” diagrams, shown in Figure 41. Both photons have spacelike momenta ($q^2 < 0$, where q is its four momentum). This group dominates the cross section when one of the electrons (positrons) is emitted at a small angle. These diagrams are the most important for the events considered here.

The second group is the “bremsstrahlung” group, shown in Figure 42. Here, one of the photons is timelike ($q^2 > 0$) and the other is spacelike ($q^2 < 0$). When one of the electrons is emitted at a small angle, the contribution from these events is small,

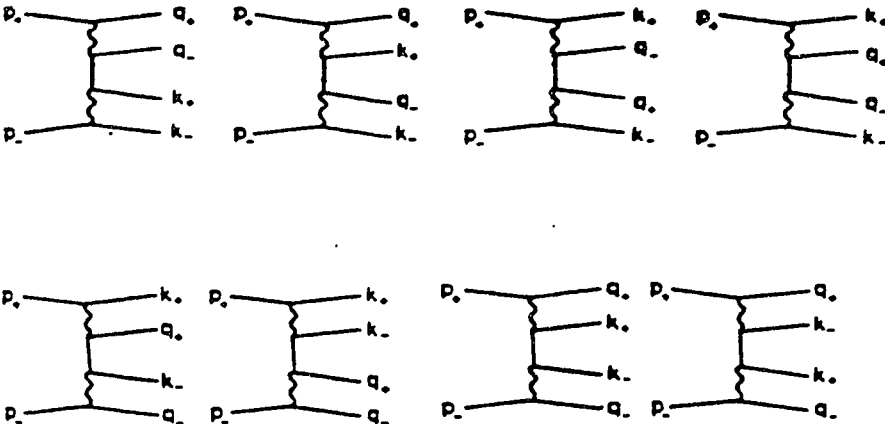


Figure 41: The multiperipheral diagrams.

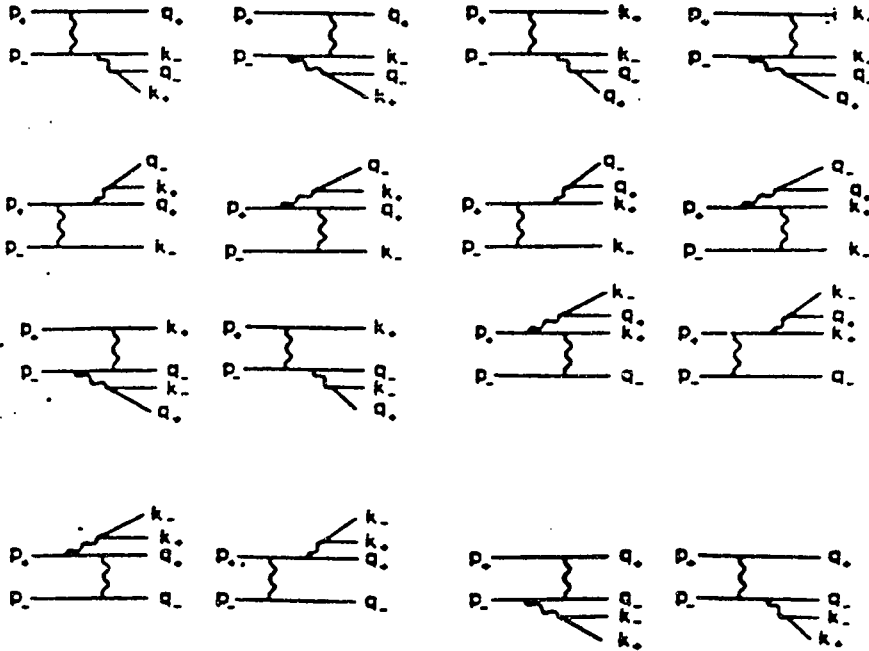


Figure 42: The bremsstrahlung diagrams.

and may be neglected compared to the multiperipheral contribution.

The third and fourth groups are the “conversion” and “annihilation” groups (shown in Figures 43 and 44). Both photons are timelike ($q^2 > 0$). They too can be neglected for the events studied herein.

5.2 Event generation

The Berends *et al.*[1] Monte Carlo program can generate events which have a distribution given by the exact differential cross section; the cross section is calculated numerically as described above. Being able to generate events is important for studying detector response and developing the criteria for event selection in a particular

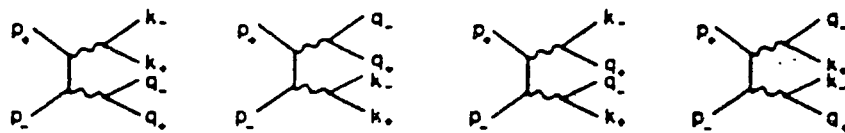


Figure 43: The conversion diagrams.

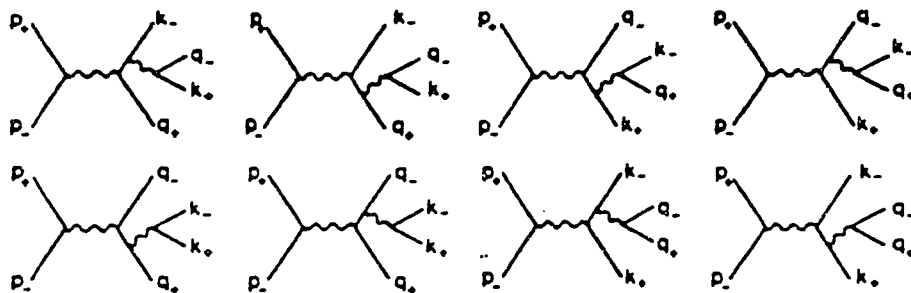


Figure 44: The annihilation diagrams.

detector and experiment.

For each of the four diagram groups (multiperipheral, bremsstrahlung, conversion, or annihilation), a function that approximates the exact differential cross section is constructed. This function is designed to be integrated analytically and to have the same peaking structure as the exact differential cross section for that group. Using the functions, the total approximate cross sections for the groups are calculated. Then, an event is generated according to one of the four groups using the calculated total approximate cross sections as weights. This initial weight, W_i , for an event generated for group i is simply the ratio of the exact differential cross section to the approximate one ($W_i = \frac{d\sigma_i}{d\tilde{\sigma}_i}$ where $d\tilde{\sigma}_i$ is the approximate differential cross section for group i).

Once an event is generated, the program decides whether to keep or reject it. A random number R between zero and one is generated. If $R \times W_{max} > W_i$, where W_{max} is the estimated maximum subgenerator weight, then the event is rejected and a new event is generated. If $R \times W_{max} < W_i$, the event is accepted.

Interferences between the four groups are then determined. The matrix element squared is

$$\sum_{spins} |M|^2 \quad M = M_m + M_b + M_c + M_a$$

where M_m is the amplitude of the multiperipheral diagrams, M_b is that of the bremsstrahlung diagrams, and so on. The events are then assigned a weight equal to

$$\frac{\sum |M|^2}{\sum \{|M_m|^2 + |M_b|^2 + |M_c|^2 + |M_a|^2\}} = FT.$$

Again, if this ratio when multiplied by a random number between zero and one is less than a predetermined maximum value, FT_{max} , then the total exact cross section is calculated.

Finally, the event is given a new weight, $W_n = \max(FT, FT_{max})$. For the events n generated by each generator i , the average of their weights $\langle W \rangle_i$ is calculated. The total exact cross section is thus given by

$$\sigma = \sum_{i=1,4} \frac{N_i}{N} \langle W \rangle_i \tilde{\sigma}$$

where $\tilde{\sigma}$ is the total approximate cross section ($\tilde{\sigma} = \sum_{i=1,4} \tilde{\sigma}_i$, i = subgenerator), N_i is the number of events created by that subgenerator, and N is the total number of events.

This event generator can be used for any experimental set-up. The user can specify such things as the beam energy, the invariant masses of the outgoing particles, and the scattering angles of the beam particles. Berends *et al* [1] found that in the experimental situation where only two of the leptons are observed in the detector, the multiperipheral diagrams totally dominate the cross section. Since that is the case studied here, only that particular subgroup of diagrams is used.

5.3 Monte Carlo signal generation

In order to accurately compare data to theoretical predictions, it is necessary to determine the effects of the detector. The particles generated by the Monte Carlo program are sent through a code which simulates the response of the detector. The simulated data is then sent through the same analysis programs used on the experimental data. This allows a determination of selection criteria appropriate for a particular detector.

Particle momenta for the process $e^+e^- \rightarrow e^+e^-e^+e^-$ were generated by the Berends, Daverveldt, and Kleiss [1] event generator as described in Section 5.2. Only the multiperipheral diagrams were used; thus, the weight for that group was set equal to one,

and the weights for the other three groups were set equal to zero. All possible virtual photon and all possible Z^0 exchanges were included to order α^4 . The kinematic range of the generated particles extended a few standard deviations beyond the final acceptance criteria. The kinematical requirements on the generated events were:

- One of the final state electrons had a scattering angle, θ_{e-} , in the range $0^\circ \leq \theta_{e-} \leq 180^\circ$.
- One of the final state positrons had a scattering angle, θ_{e+} , in the range $0^\circ \leq \theta_{e+} \leq 180^\circ$.
- One of the other two particles was required to have a scattering angle of 32° or greater.
- The invariant mass, M_{pair} , of the two low-energy particles was required to be at least $200 \text{ MeV}/c^2$.

The beam energy for the Monte Carlo was set at 45.6 GeV , resulting in a center-of-mass energy of 91.2 GeV . Since the two-photon cross section is proportional to $[\ln(E_b)]^3$ (see Equation 95), the cross section changes very little over the SLC energy scan in the 1989 data run. For the 1990 data run, the center-of-mass energy was 91.2 GeV .

The generated events consist of the charges, particle types, and four-vectors of the final state particles. The four-vectors were “tracked” through the subsystems of the detector, including the effect of the magnetic field. This simulation included effects of multiple scattering, photon conversions, bremsstrahlung, nuclear interactions, electromagnetic interactions, and energy loss (dE/dx) of the particles, each according to the amount of material encountered by the particles. Known defects in the detector such as dead wires and cell inefficiencies in the central drift chamber, and hadronic

	Lum (nb^{-1})	# Events
MC89	1257.3	41970
MC90	714.2	23842

Table 11: Statistics for Monte Carlo runs MC89 and MC90.

punch-through in the muon system were included. The Monte Carlo event record was written to tape in a format identical to that for the experimental data.

The addition of the smaller beampipe and vertex detectors required generating events for this new detector configuration. The events statistics and integrated luminosities for each Monte Carlo run (MC89 for the 1989 configuration and MC90 for the 1990 configuration) are summarized in Table 11.

The track multiplicity distributions for MC89 and MC90 events are shown in Figure 45 and Figure 46. As shown, the events typically have one or two tracks. The pair mass distributions are shown in Figures 47 and 48. They are peaked at low energies, illustrating that this process occurs at low momentum transfer, with virtual photons.

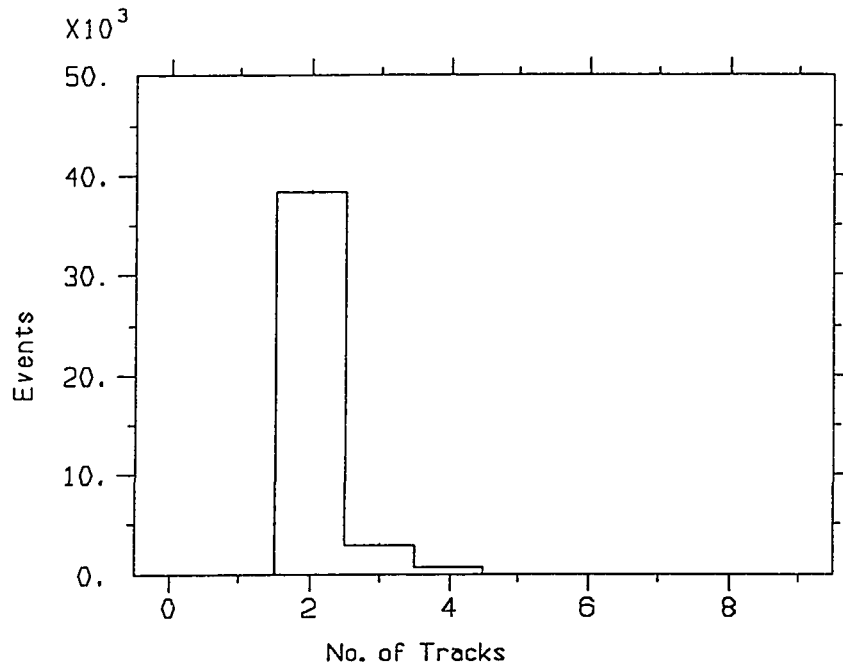


Figure 45: Track multiplicity for MC89 events.

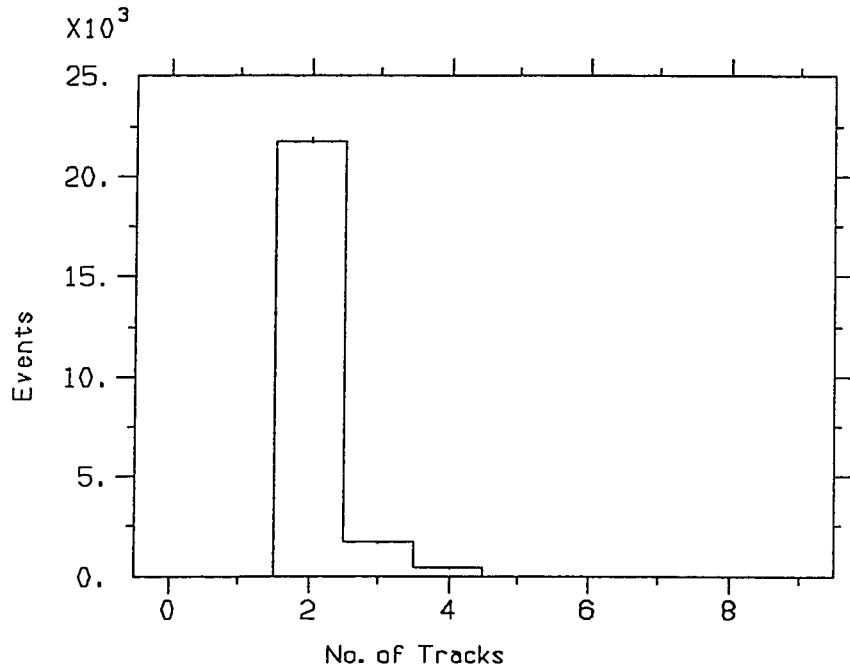


Figure 46: Track multiplicity for MC90 events.

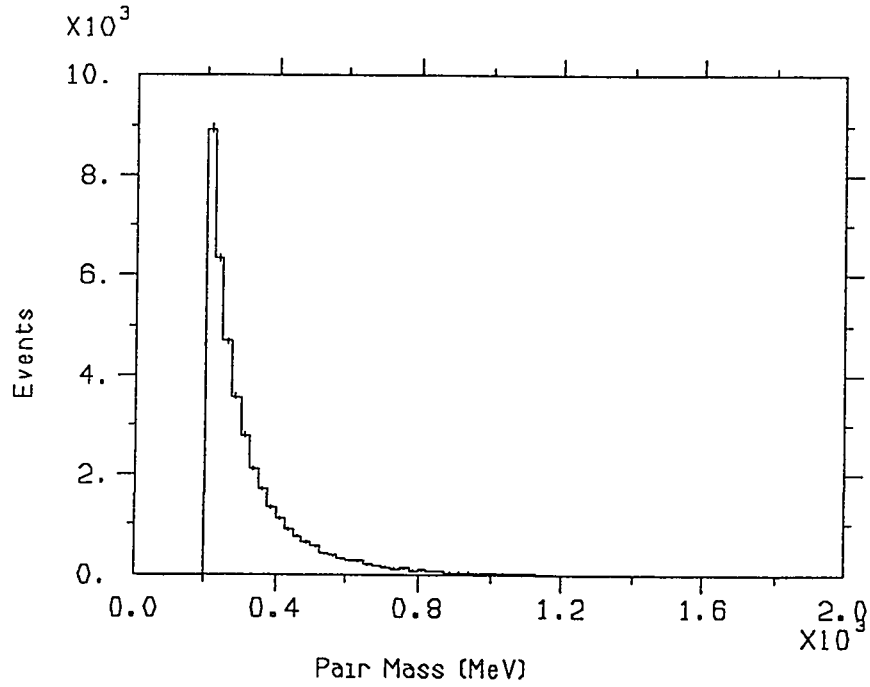


Figure 47: Invariant pair mass distribution for MC89 events.

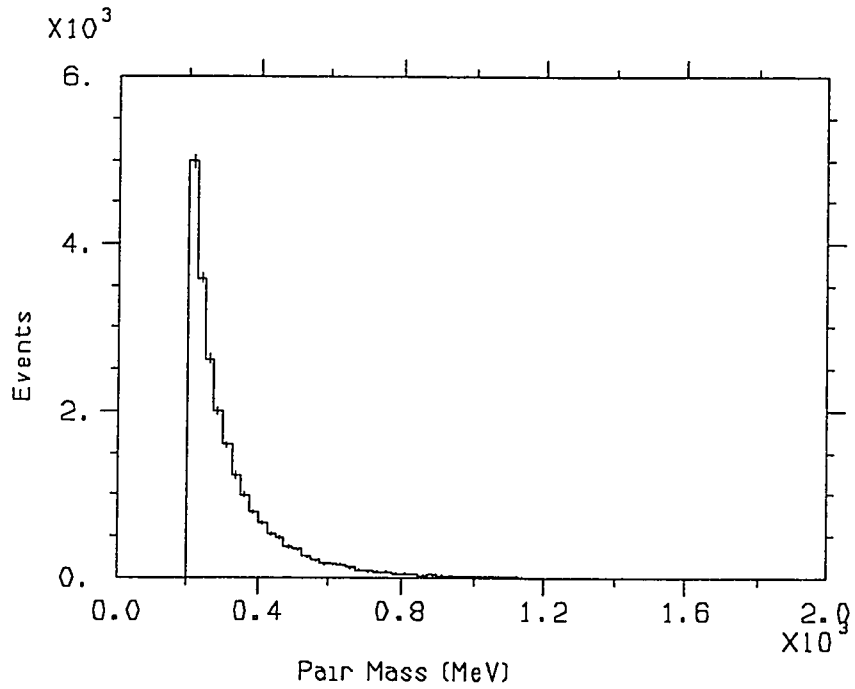


Figure 48: Invariant pair mass distribution for MC90 events.

Chapter 6

Event Selection and Analysis

This chapter presents the criteria for distinguishing the $e^+e^- \rightarrow e^+e^-e^+e^-$ events from all of the data logged by Mark II. The data sample consists of data collected from April through October 1989, and July through November 1990. For the first data run, the center-of-mass energies range from 89.2 to 93.0 GeV, as listed in Table 12. This corresponds to an integrated luminosity of $19.7 \pm 0.8 \text{ nb}^{-1}$, as listed in Table 12. For the second data run, the center-of-mass energy is 91.2 GeV, and the sample has an integrated luminosity of $10.1 \pm 0.7 \text{ nb}^{-1}$. Because the two-photon cross section is proportional to $[\ln(E_b)]^3$, the two-photon event rate changes little over the energy scan. Therefore, the total integrated luminosities are used to compare data with the QED prediction.

To select two-photon events from the total number of events logged by the Mark II detector, a set of selection cuts is necessary. The cuts should be specific enough to eliminate background events but still allow selection of a large two-photon event sample. The efficiency of this criteria is then determined using Monte Carlo events with full detector simulation.

Energy Scan Point (GeV)	Luminosity (nb ⁻¹)
89.2	0.68
90.0	0.76
90.4	2.61
90.7	1.21
91.1	4.08
91.4	4.12
91.5	1.23
92.2	3.59
92.6	0.40
93.0	1.00
Totals	19.7

Table 12: Integrated luminosity at each energy scan point for the 1989 data run.

More than 8 million triggers were logged by the Mark II detector. The first task is to separate two-photon candidate events from Z^0 decays, beam-gas interactions, and beam-beampipe interactions. In order to compare data to Monte Carlo predictions, it is also necessary to eliminate those events occurring outside the part of the detector which is accurately simulated by the Monte Carlo program.

6.1 Event topology

As described in Chapter 4, the two-photon events studied here arise from the multiperipheral diagrams. They show up in the detector as two charged tracks. The tracks have opposite charge and are back-to-back in the x - y plane. The other two of the four final state particles are emitted at small angles, escaping undetected down the beampipe. These two particles carry away most of the energy, so that the total visible energy in the detector (E_{vis}) is small compared to the center-of-mass energy, E_{cm} .

These criteria can be summarized by defining the following cuts:

C1: Only two charged tracks. Both tracks must have $|z| \leq 4$ cm and $|r| \leq 1.5$ cm, where $\{r = 0, z = 0\}$ is the interaction point (IP).

Cut **C1** reduces the number of beam-gas and beam-beampipe interactions in the event sample. A beam-gas interaction occurs when the beam particles interact with the residual gas inside the beampipe to produce particles, which then enter and trigger the detector. Beam-beampipe interactions are interactions where the beam particles interact with the actual beampipe, or with the wire flippers inside the beampipe. These events can originate at any point along the z direction. Figure 49 shows the distribution in z of events with two tracks after the r cut, for the 1989 data set. The

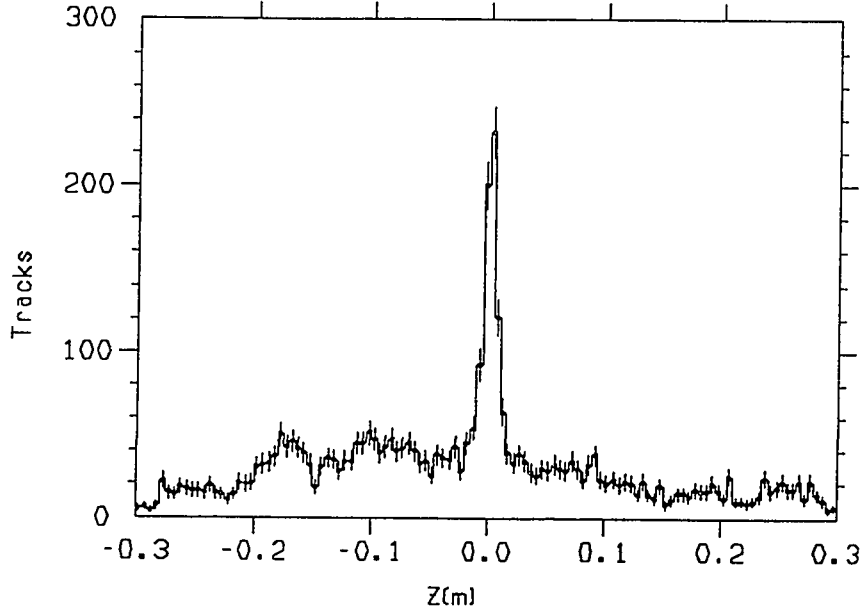


Figure 49: Distribution in z (after r cut) of all 1989 two-track events.

peaks centered at the IP include Z^0 leptonic decays as well as two-photon events. At large values of z , beam-gas and beam-beampipe interactions are evident. By requiring tracks to originate at the IP, these interactions are eliminated. Figure 50 show the distribution for the 1990 data set. For this set, cuts **C2** and **C3** were applied first (see below). A higher number of beam-beampipe interactions due to the smaller beampipe is apparent.

C2: $\sum q_i = 0$, where i is the number of tracks ($i = 2$). The two tracks should be equal and oppositely charged.

Cut **C2** also removes beam-beampipe events, which may have two tracks of the same sign.

C3: $|\cos(\Delta\phi)| > 0.8$, where $\Delta\phi$ is the angular separation of the tracks in the x - y plane. As described in chapter 4, the two tracks should be back-to-back in the x - y

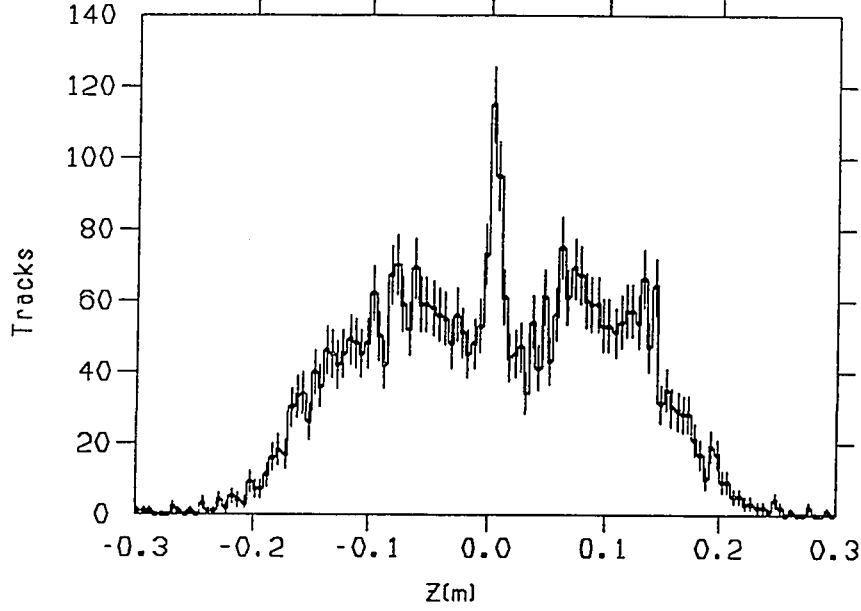


Figure 50: Distribution in z (after r cut) of all 1990 two-track events. These are the events after cuts C2-C3 are applied.

plane, or $|\cos(\Delta\phi)| \approx 1$.

C4: $E_{vis} < 0.2E_{cm}$, where E_{vis} is defined as:

$$E_{vis} = \sum \sqrt{|\vec{p}|^2} + \sum_{\text{neutral showers}} E_{\gamma}$$

Cut C4 removes all of the Z decay events (hadronic and leptonic) because these have visible energy close to the center-of-mass energy.

Therefore, cuts C1-C4 remove all of the Z^0 decay events (hadronic and leptonic) and almost all of the beam-gas and beam-beampipe events.

6.1.1 Charged track criteria

Reconstructed charged tracks must satisfy the following cuts: C5: $p_t \geq 150 \text{ MeV}/c$, where p_t is the transverse momentum of the track with respect to the z -axis; and

C6: $|\cos \theta| \leq 0.70$, where θ is the angular direction of the track at the origin, with respect to the z -axis.

Cuts **C5** and **C6** are imposed to ensure a high trigger efficiency. Particles with p_t greater than 110 MeV/c will leave the drift chamber without curling up on themselves. As stated in Section 3.2.2, in order to avoid avoid this region of reduced efficiency (see Figure 24), we require $p_t > 150$ MeV/c. As shown in Figure 22, tracking efficiency is $> 99\%$ for $|\cos \theta| \approx 0.8$; the efficiency is flat for $|\cos \theta| \leq 0.70$. This is also the solid angle coverage of the TOF system, and ensures a reliable TOF measurement for particle identification.

6.2 Particle identification

The cuts in Section 6.1 produce a sample of two-photon events of the type $e^+e^- \rightarrow e^+e^-l^+l^-$ where the l can be an electron, muon, or quark. Particle identification is used to select out the events where l is an electron.

As described in Chapter 3, dE/dx information from the drift chamber and time-of-flight information from the TOF system can be used to determine one particle type from another. For each track in a given event, the measured dE/dx value (dE/dx_{meas}) and dE/dx resolution (σ_n), for particle of type n is recorded. The probability of a track being a particular particle type n is [36]:

$$P_n = \frac{1}{\sqrt{2\pi}\sigma_n} \exp \left\{ -\frac{1}{2} \left(\frac{dE/dx_{meas} - dE/dx_{expected}}{\sigma_n} \right)^2 \right\}$$

The weight for the particle being an electron is

$$W_e = \frac{P_e}{\sum_i P_i}$$

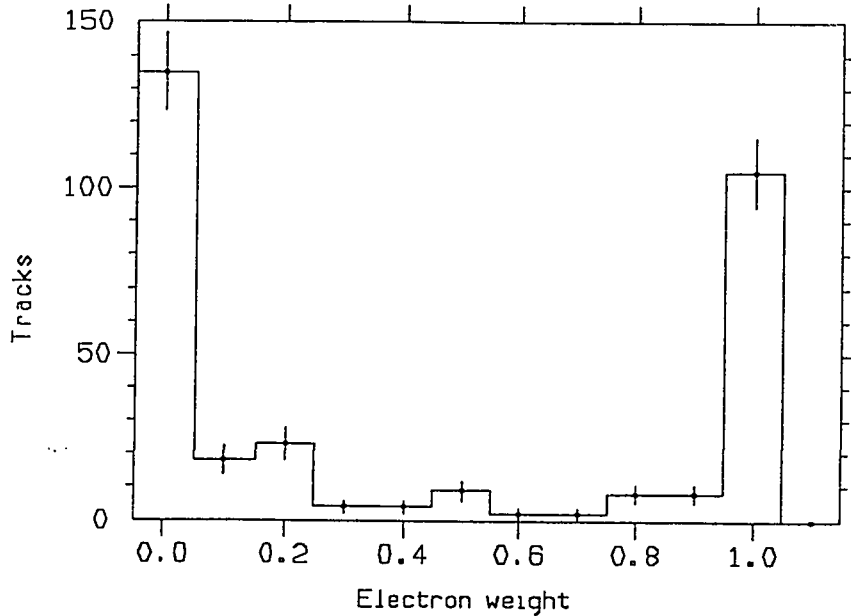


Figure 51: Electron weights for 1989 data set. These are the weights after cuts C1-C6 are imposed.

A similar formula holds for the TOF information, with the exception that the resolution, σ^{TOF} , does not depend on the particle type.

Figure 51 shows the electron probability weights for each track in the 1989 data set after cuts C1-C6. There is a peak at zero, for those particles that are not electrons (muons and pions) and a peak at one for the electrons(positrons). Figure 52 shows the weights for the 1990 data set, with similar peaks. The weights for the Monte Carlo generated events are shown in Figures 53 and 54.

To select out the $e^+e^- \rightarrow e^+e^-e^+e^-$ events, one track is required to have a weight for being an electron of 0.7 or greater; if this is satisfied, the other is required to have a weight of 0.2 or greater. Because of lepton conservation, if one is an electron, the other is assumed to be the positron. The lower limit of 0.2 is imposed to eliminate those tracks whose dE/dx values are not accurately measured (weights equal to zero).

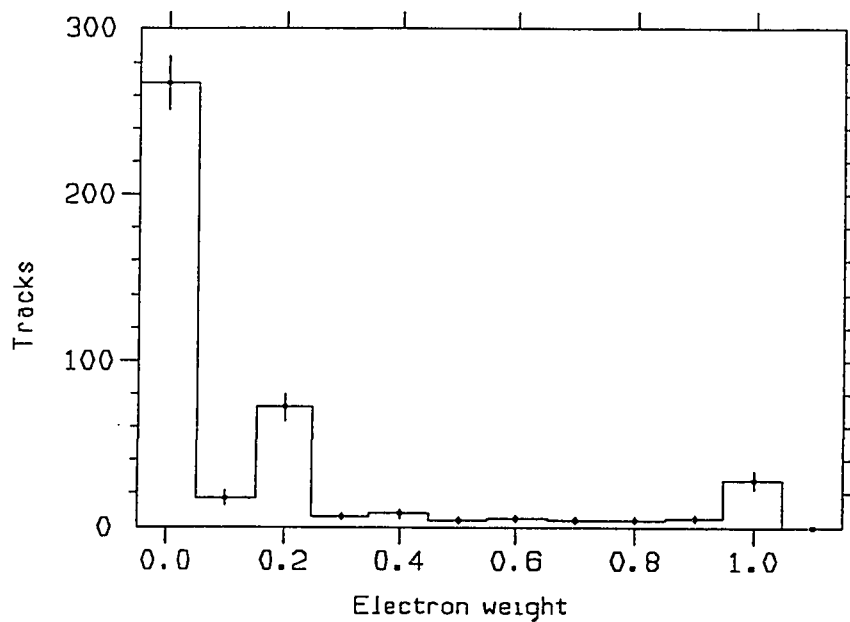


Figure 52: Electron weights for 1990 data set. These are the weights after cuts C1-C6 are imposed.

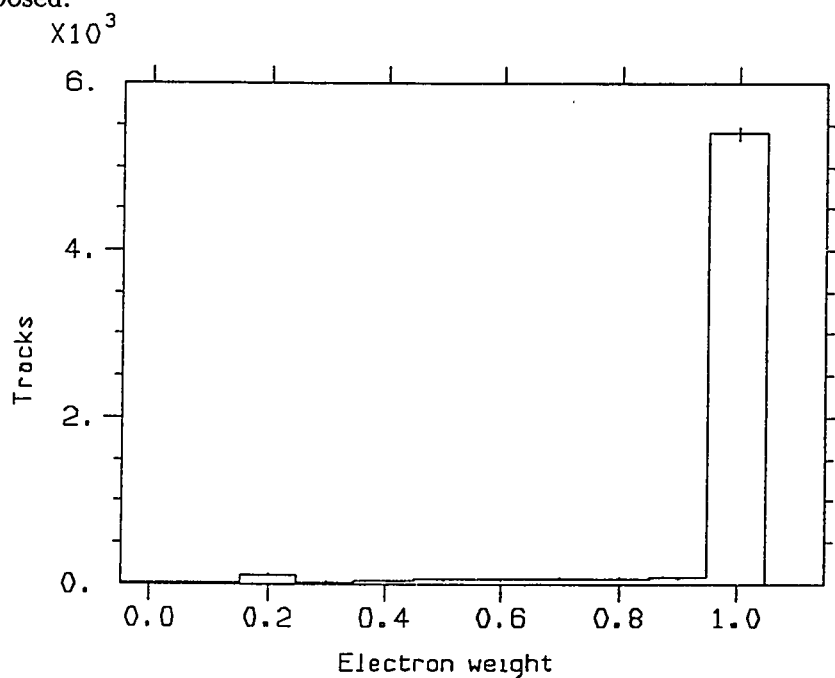


Figure 53: Electron weights for MC89 events. These are the weights after cuts C1-C6 are imposed.

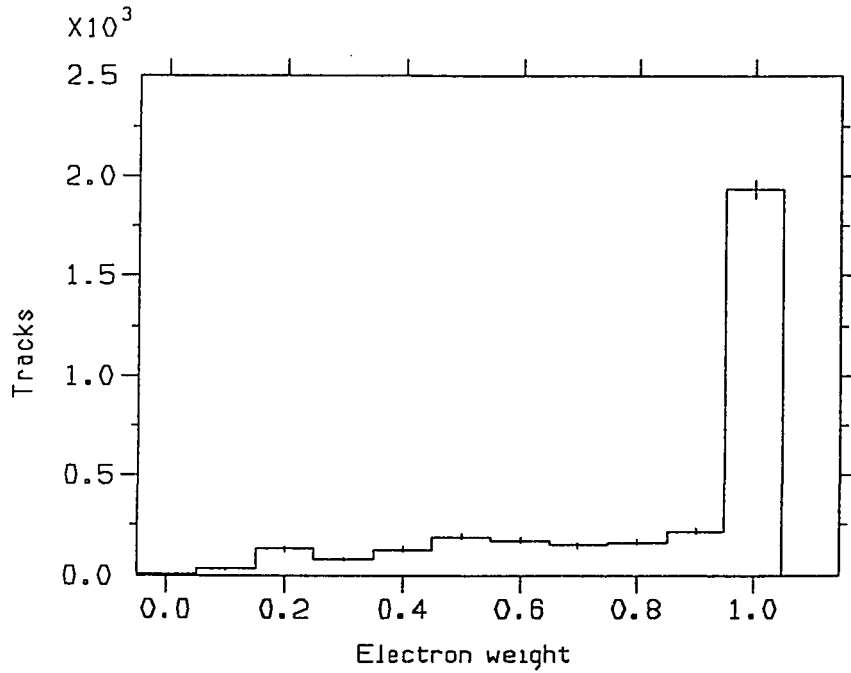


Figure 54: Electron weights for MC90 events. These are the weights after cuts C1-C6 are imposed.

Therefore, this final cut is:

$$C7: W_1 \geq 0.7 \text{ and } W_2 \geq 0.2, \text{ for tracks 1 and 2 in the event.}$$

6.3 Results after selection cuts

The effect of cuts C1-7 on the 1989 and 1990 data sets is shown in Table 13. In each row is listed the number of events surviving each cut. After all of the cuts are applied, 62 events are selected out of the 1989 data set, and 24 events are selected out of the 1990 data set.

A typical event as seen in the Mark II detector, is shown in Figure 55. All three views are depicted.

Cut	Data	Data
	1989	1990
	19.7 nb ⁻¹	10.1 nb ⁻¹
$r \leq 0.015\text{m}, z \leq 0.040\text{m}$	680	N.A.
$\sum q = 0$	515	N.A.
$ \cos(\phi_1 - \phi_2) $	445	573
$E_{vis} \leq 0.2E_{cm}$	397	546
$p_t \geq 150$	295	439
$ \cos \theta \leq 0.70$	173	251
particle ID	62	24

Table 13: The effect of selection cuts on the two data sets. The number of events in each row is the number that remains after that cut has been applied. For the 1990 data run, the numbers for the first two cuts are not available (N.A.).

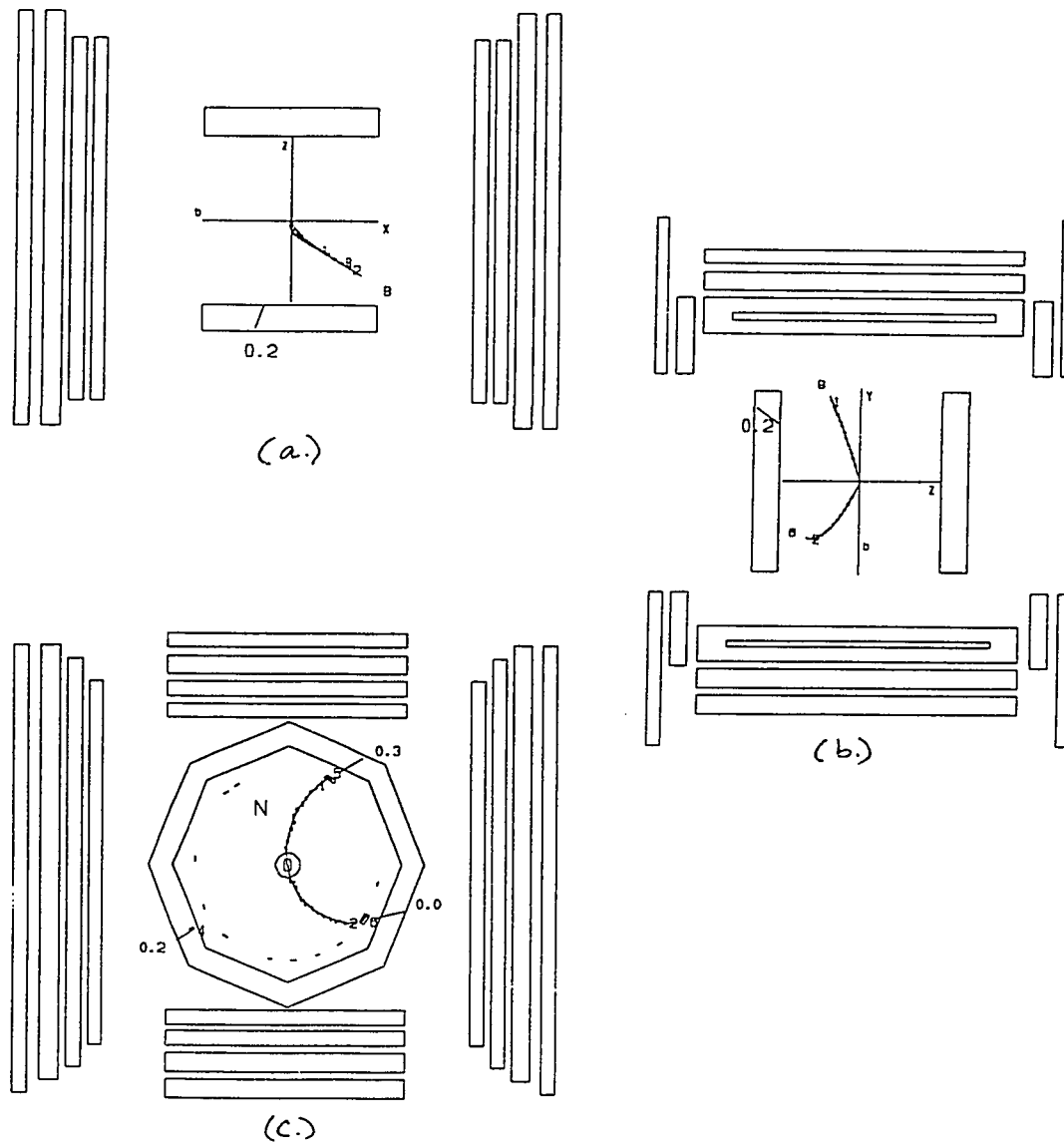


Figure 55: A typical multiperipheral two-photon event seen in the Mark II detector: (a) side view ($x-z$), (b) side view ($y-z$), (c) beam view ($x-y$).

6.4 Estimated backgrounds

The events selected are those which have a final state consisting of two oppositely charged particles which are identified as an electron and a positron. Background events will be those events from processes which result in an electron-positron pair, or events having two oppositely charged particles which are mistakenly identified as an electron and positron.

Processes which may result in an electron-positron pair are:

$$\begin{aligned} e^+e^- &\rightarrow Z^0 \rightarrow e^+e^- \\ e^+e^- &\rightarrow Z^0 \rightarrow \tau^+\tau^- \\ e^+e^- &\rightarrow e^+e^-\tau^+\tau^- \end{aligned}$$

where the taus subsequently decay into electrons and positrons (and their associated neutrinos).

Processes which result in a final state which may be misidentified as an electron-positron pair are:

$$\begin{aligned} e^+e^- &\rightarrow Z^0 \rightarrow \mu^+\mu^- \\ e^+e^- &\rightarrow Z^0 \rightarrow \tau^+\tau^- \\ e^+e^- &\rightarrow e^+e^-\mu^+\mu^- \\ e^+e^- &\rightarrow e^+e^-\pi^+\pi^- \end{aligned}$$

as well as beam-beampipe and beam-gas events. Because the SLC energy is set at the Z^0 resonance, the contribution from electron-positron annihilation via photon exchange is negligible.

6.4.1 Backgrounds from $e^+e^- \rightarrow Z^0$ processes

The energy cut (C4) is designed to eliminate events which arise from the following processes:

$$e^+e^- \rightarrow Z^0 \rightarrow e^+e^-$$

$$e^+e^- \rightarrow Z^0 \rightarrow \mu^+\mu^-$$

$$e^+e^- \rightarrow Z^0 \rightarrow \tau^+\tau^-$$

In these processes, all of the energy from the Z^0 is transferred to the two final particles. Therefore, requiring the visible energy to be less than a fifth of the Z^0 mass energy would remove these events.

The Z^0 events identified by the Mark II collaboration were sent through the criteria used to identify two-photon events; no events passed these cuts in the 1989 data set and no events passed these cuts in the 1990 data set. Therefore, the number of background events expected from these processes is less than one event for each of the data sets.

6.4.2 Backgrounds from two-photon processes

The two-photon processes which may contribute backgrounds to the $e^+e^- \rightarrow e^+e^-e^+e^-$ case are:

$$e^+e^- \rightarrow e^+e^-\mu^+\mu^-$$

$$e^+e^- \rightarrow e^+e^-\tau^+\tau^-$$

$$e^+e^- \rightarrow e^+e^-\pi^+\pi^-$$

In order to estimate the expected background, the cross sections for each of these were obtained by running the Monte Carlo with the same criteria as described in Chapter 5 (minimum scattering angle of 32° and minimum pair mass of 200 MeV.). Because the minimum angle and pair mass thresholds are lower than those used in the cuts

l	e	μ	τ
$\sigma_{ee \rightarrow e\ell\ell}$ (nb)	33.4	17.2	0.05

Table 14: Cross sections for two-photon processes as determined by Monte Carlo. Only the multiperipheral diagrams are taken into account.

on the data, the Monte Carlo cross sections will slightly overestimate the number of events expected from these processes. For the pion case, the simulated process was $e^+e^- \rightarrow e^+e^-u\bar{u}$, where u is the up quark. The quarks are then fragmented according to the Lund fragmentation scheme. As before, only the multiperipheral diagrams are included. The resulting cross sections are shown in Table 14, as well as the cross section for the $e^+e^- \rightarrow e^+e^-e^+e^-$ case.

The cross section for $e^+e^- \rightarrow e^+e^-\tau^+\tau^-$ is almost 1/1000 of the cross section for the $e^+e^- \rightarrow e^+e^-e^+e^-$ case. This implies that the background from this case will be negligible. Assuming that each of the tau pairs results in an electron-positron pair, and these are identified as such, the number of tau events is expected to be (for a given luminosity)

$$N_\tau = N_e \frac{\sigma_\tau}{\sigma_e}. \quad (101)$$

For the 62 events found after cuts C1-7 from the 1989 data set, and the 24 events found from the 1990 data set, the expected number of background events from two-photon created tau pairs which decay into electron-positron pairs is 0.09 and 0.04 respectively. Two-photon tau pairs which decay into muons or pions are removed by the particle identification cut.

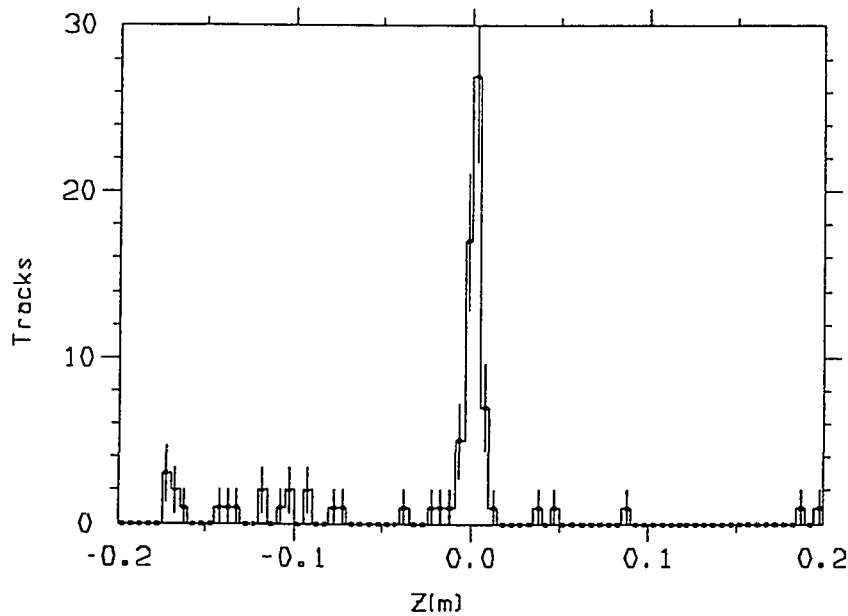


Figure 56: Distribution in z of the event vertex for the 1989 data run. The plot is made after the particle identification cut, but with no cut in z .

The remaining background processes from two-photon events (muon and pion pairs), as well as beam-beamgas and beam-beampipe events, are expected to be removed by the particle identification cut, C7. Estimations of the background from these events after cut C7 are discussed in Section 6.4.3.

6.4.3 Backgrounds from beam-beam processes

Beam-beamgas events and beam-beampipe events may be produced at any point along the beamline. Therefore, they will occur evenly distributed in the z direction. Figures 56 and 57 show the distribution in z after the particle identification cut (C7) is imposed, but without adding the vertex cut in z . There is an apparent peak centered at $z = 0$ as well as events at higher z . Comparing these figures with Figures 49 and 50 shows that the particle identification cut removes a great deal of this background.

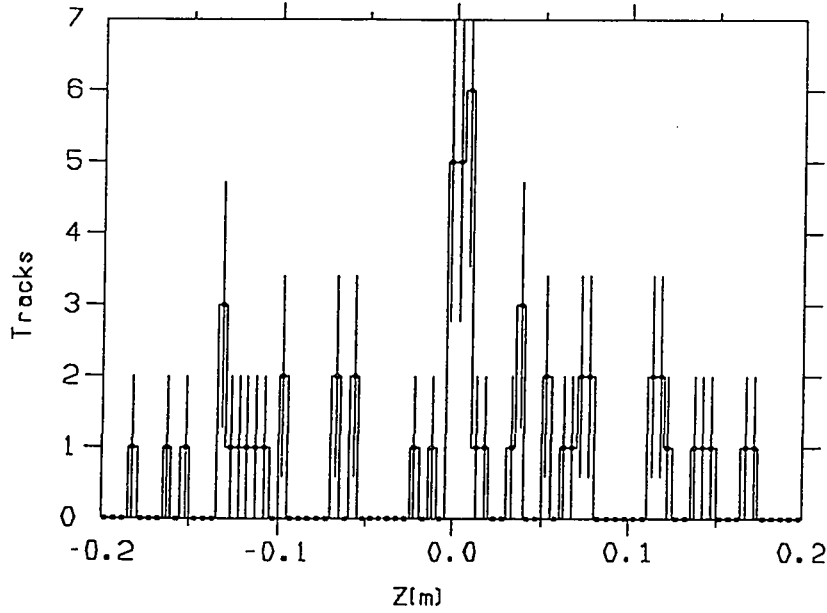


Figure 57: Distribution in z of the event vertex for the 1990 data run. The plot is made after the particle identification cut, but with no cut in z .

In order to estimate the number of background events that lie in the central peak, we look at the total transverse momentum in the event. The total transverse momentum (p_i^{tot}) is the vector sum of the transverse momentum of the two tracks in the events

$$(p_i^{tot})^2 = \left| \sum_{i=1}^2 \vec{p}_i \right|^2 \quad (102)$$

$$\vec{p}_i = p_x^i \hat{x} + p_y^i \hat{y}.$$

Because the photons are emitted approximately along the beam direction, two-photon events are expected to have zero, or almost zero, total transverse momentum. Figure 58 shows the distribution of total p_i^2 for MC89 (after cut C7 is made). If a cut is made at $p_i^2 = 0.03 \text{ GeV}^2/c^2$, approximately 7.5% of the Monte Carlo events are removed. Figure 59 shows a two-dimensional plot of the square of the total p_i versus z of the event vertex. Here, all of the events are clustered around $z = 0$. Figures 60

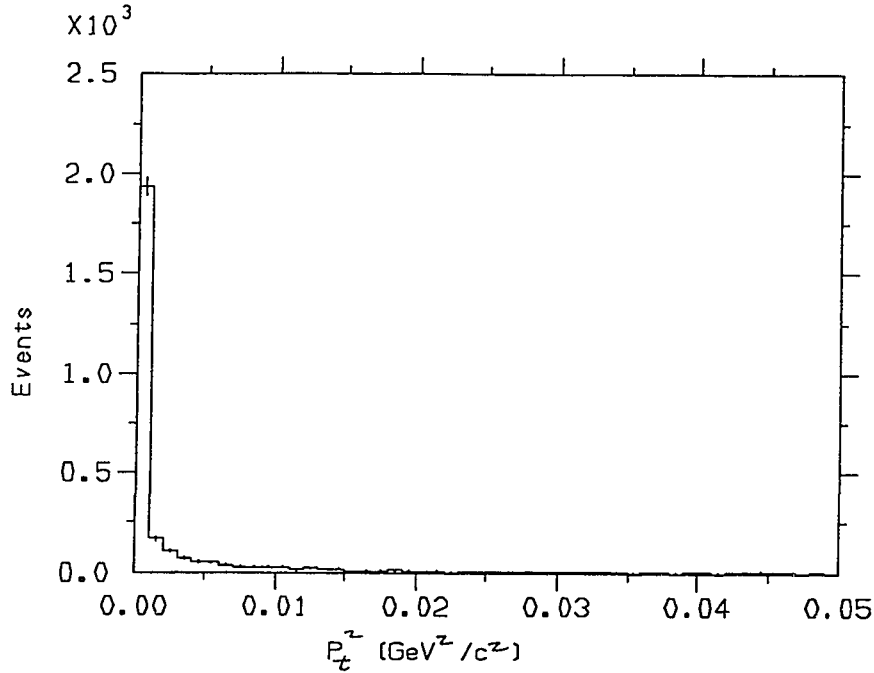


Figure 58: Distribution of total p_t^2 for MC89 after all analysis cuts are made except for the z cut.

through 63 show the same plots for the 1989 and 1990 data sets. Events at large z are clearly visible outside the central peak. If a cut is made at $p_t^2 = 0.03 \text{ GeV}^2/c^2$, then the number of background events in the central peak can be estimated by looking at the number of events which fall between $0.04 < |z| < 0.2$.

For the 1989 data set, with $p_t^2 \leq 0.03 \text{ GeV}^2/c^2$, 9 events lie in the region $0.2 \leq z < -0.04$ meters (region 1), 52 events in the region $-0.04 \leq z \leq 0.04$ (region 2), and 2 events in the region $0.04 < z \leq 0.2$ (region 3) as shown in Figure 61. The ratio of the sum of the areas on either side of the central region to area of the central region is 4:1. Therefore, the number of background events in the central region is estimated to be $(9 + 2)/4 = 2.75$, or ≈ 3 events.

For the 1990 data set, there are 7 events in region 1, 12 events in region 2, and 12 events in region 3 (see Figure 63). Therefore, the number of background events in

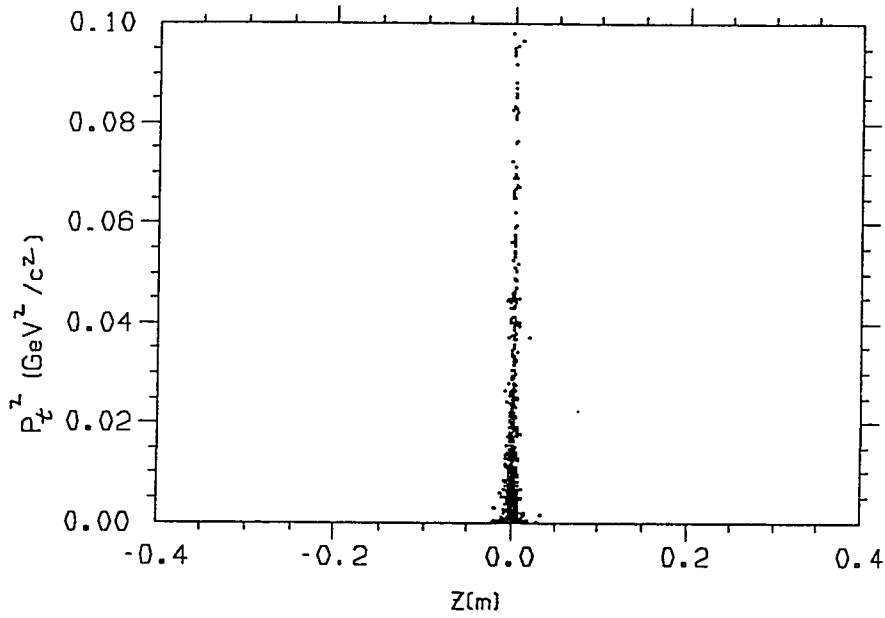


Figure 59: Two-dimensional plot of total p_t^2 and z for MC89 after all analysis cuts are made except for the z cut.

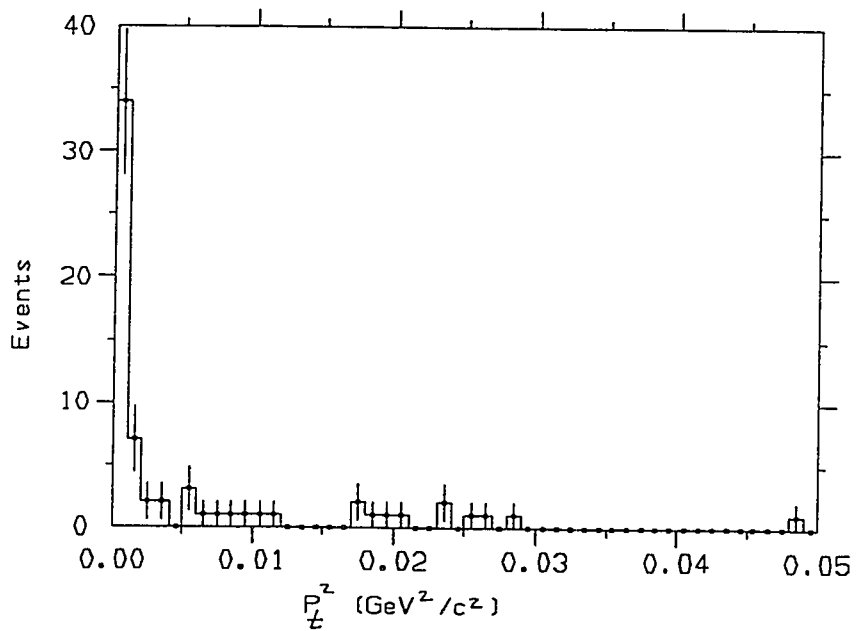


Figure 60: Distribution of total p_t^2 for the 1989 data run after all analysis cuts are made, except for the z cut.

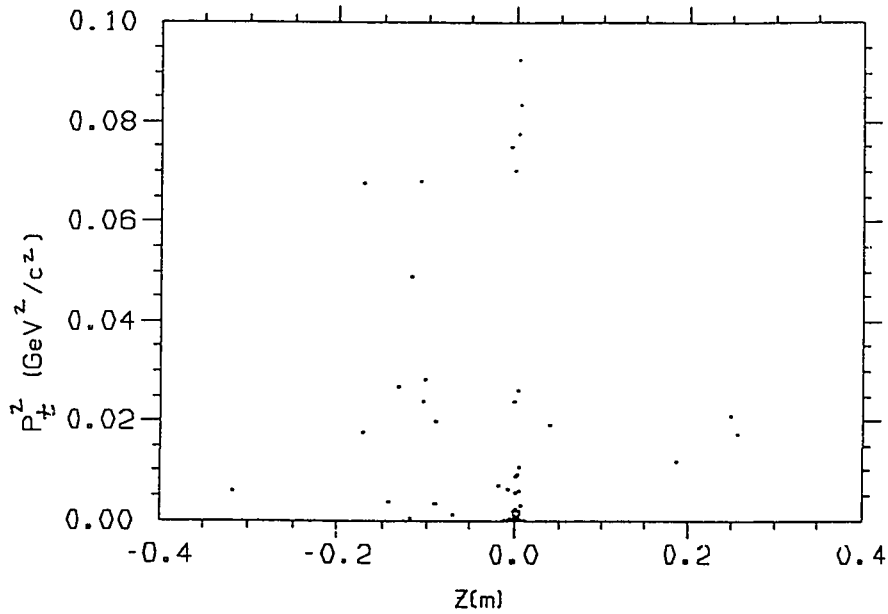


Figure 61: Two-dimensional plot of total p_t^2 and z for the 1989 data run after all analysis cuts are made, except for the z cut.

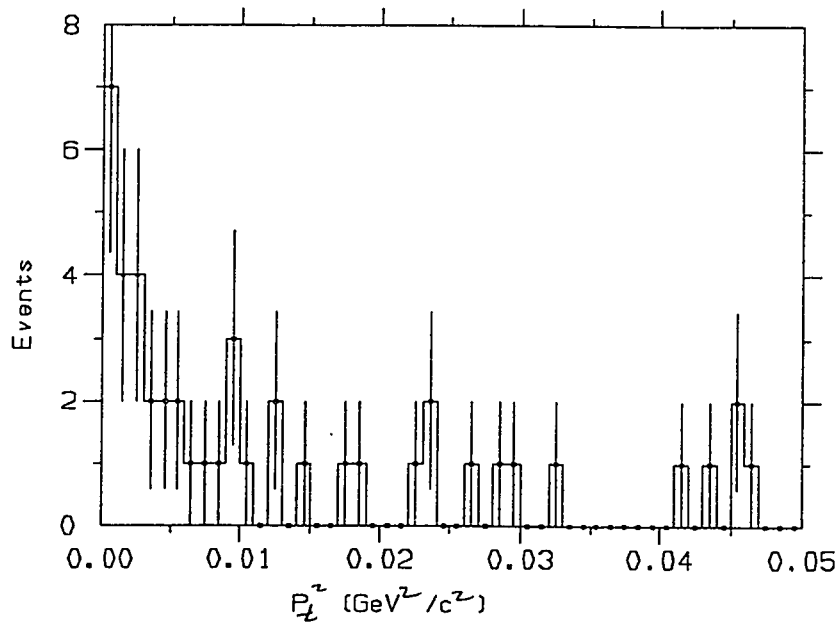


Figure 62: Distribution of total p_t^2 for the 1990 data run after all analysis cuts are made, except for the z cut.

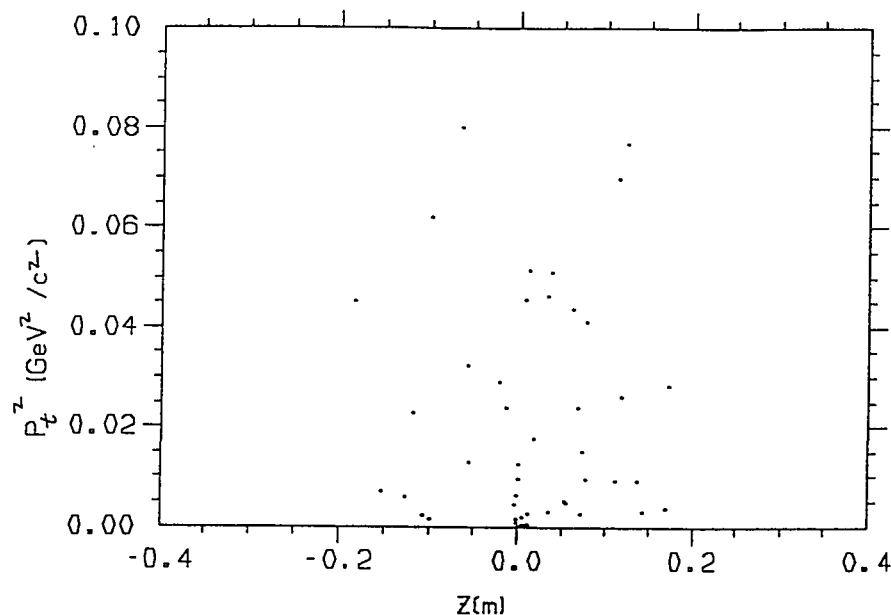


Figure 63: Two-dimensional plot of total p_t^2 and z for the 1990 data run after all analysis cuts are made except for the z cut.

the central region is estimated to be $(7+12)/4 = 4.75$, or ≈ 5 events.

6.5 Systematic errors

The data selection cuts are chosen to select out certain events based on measured quantities (momentum, time-of-flight, etc). These quantities are measured by the detector for each event, and the detector has a certain measurement resolution for each. The detector has been simulated for the Monte Carlo; by passing generated events through this simulated detector, we can predict the number of events we should see in the data. However, systematic errors arise from the finite resolution of the detector and from imperfect detector simulation.

For this study, the most significant sources of detector systematic error are the

momentum, time-of-flight, and dE/dx measurements. Because the two-photon events have low-momentum tracks, a variation in the measured momentum may determine whether the event passes the momentum cut, C5. The time-of-flight and dE/dx measurements are used to identify the particle type and therefore determine whether an event passes the particle identification criteria. To estimate the magnitude of these systematic errors, we individually shift the values and resolutions of the momentum, TOF, and dE/dx measurements by two σ , and see how many of the Monte Carlo generated events pass the cuts using the shifted values. Two σ is used to provide a conservative estimate of the errors.

From Chapter 3, Equation 64 gives the drift chamber momentum resolution as

$$\frac{\sigma(p)}{p} = \sqrt{(0.0046p)^2 + (0.019)^2},$$

with p in GeV/c. For the momentum cut-off of $p_t = 150$ MeV/c, the term due to multiple scattering dominates. Therefore, σ for $p = 150$ MeV is

$$\sigma = (.019) \times (.150) = .00285 \text{ GeV}/c$$

or 2.85 MeV/c. For the TOF system, we use errors of $\sigma = \pm 20$ ps for both the time-of-flight value and resolution. These errors were determined (see Reference [21]) using the fit for Figure 30. From Reference [21], the error in the dE/dx scale is about 2% of the dE/dx measurement. The error on the dE/dx resolution is also taken to be ± 0.02 .

To find the effect of these systematic errors, we shift the measured values by two σ for each, look at how many Monte Carlo events subsequently pass the cuts, and compare with how many pass when no shift is made. For example, cut C5 sets the criteria for the transverse momentum at $p_t \leq 150$ MeV/c. At this limit, 2923 of the MC89 events pass all of the cuts. We then set $p_t = 150 - 2\sigma = 144.3$ MeV/c.

With the value shifted, 3155 events pass, a -7.9% difference. Setting $p_t = 150 + 2\sigma$, 2710 events pass, a $+7.2\%$ difference (more events pass for the lower momentum because the two-photon spectrum peaks at lower momenta).

For the TOF and dE/dx systematic errors, we shift both the values and the corresponding resolutions. If the TOF and dE/dx measurements were all systematically high, and the corresponding resolutions were systematically low, we would have increased faith that the systematically high measurements were correct. Therefore, the greatest systematic error from these will occur if we shift the measurement values *up* by 2σ and the resolution values *down* by 2σ . This gives a systematic error for the TOF of 1.5% and a systematic error for the dE/dx of 3.6% .

Another source of systematic error is the error on the measured luminosities. For the data run in 1989, the integrated luminosity is

$$\int \mathcal{L}^{89} dt = 19.7 \pm 0.8 \quad \text{nb}^{-1} \quad (103)$$

(a 4.1% error). For the data run in 1990, the integrated luminosity is

$$\int \mathcal{L}^{90} dt = 10.1 \pm 0.7 \quad \text{nb}^{-1} \quad (104)$$

(a 6.9% error).

The total systematic error from all causes is calculated by summing in quadrature the various contributions, giving a systematic error of 9.7% for the 1989 data run and 11.1% for the 1990 data run. Table 15 lists the different contributions to the total systematic error.

Source	Error
Momentum resolution	-7.9%, +7.2%
Time-of-flight	+1.5%
dE/dx	+3.6%
Luminosity (1989)	$\pm 4.1\%$
Luminosity (1990)	$\pm 6.9\%$
Total (1989)	9.7%
Total (1990)	11.1%

Table 15: The different contributions to the total systematic error.

6.6 Monte Carlo event selection and comparison with data

The Monte Carlo generated events were sent through a detector simulator and then through the same set of cuts as the data. Two sets of Monte Carlo events (MC89 and MC90) were generated in order to see the effects of the vertex detectors on the detector simulation. For the comparison with the data, 25000 events from MC89 and 18000 events from MC90 were used. The effects of cuts **C1-7** are shown in Table 16 for the two Monte Carlo sets. The number of events listed next to the appropriate cut are those events remaining after that cut has been applied. The luminosities of the Monte Carlo event sets are greater than the Mark II luminosities of 19.7 nb^{-1} for 1989 and 10.1 nb^{-1} for 1990. The number of expected signal events from Monte Carlo, when scaled to the respective luminosities, is 76.9 ± 1.4 for 1989 data, and 25.3 ± 0.7 for 1990. These errors arise from Monte Carlo statistics. In the 1989 data set, 62 events are observed, and 24 are observed in the 1990 data set. Including statistical and systematic errors, and the error due to background events, the results are $62 \pm 7.9 \pm 6.0 - 3.1$ for the 1989 data set and $24 \pm 4.9 \pm 2.7 - 5.0$ for the 1990 data set, where the first error is the statistical error, the second is the systematic error, and the third is the number of background events.

The invariant pair mass distributions are shown in Figures 64 and 65.

6.7 Summary

The production of the two-photon process, $e^+e^- \rightarrow e^+e^-e^+e^-$, in the case where only two of the final state particles is observed in the SLC data and is presented here.

Cut	MC	MC
	89	90
	748.9 nb ⁻¹	539.2 nb ⁻¹
	25000	18000
$r \leq 0.015\text{m}, z \leq 0.040\text{m}$	10697	5675
$\sum q = 0$	10695	5668
$ \cos(\phi_1 - \phi_2) $	9699	5097
$E_{vis} \leq 0.2E_{cm}$	9698	5096
$p_t \geq 150$	5781	3077
$ \cos \theta \leq 0.70$	2946	1612
particle ID	2923	1350

Table 16: The results of cuts C1-7 on Monte Carlo data.

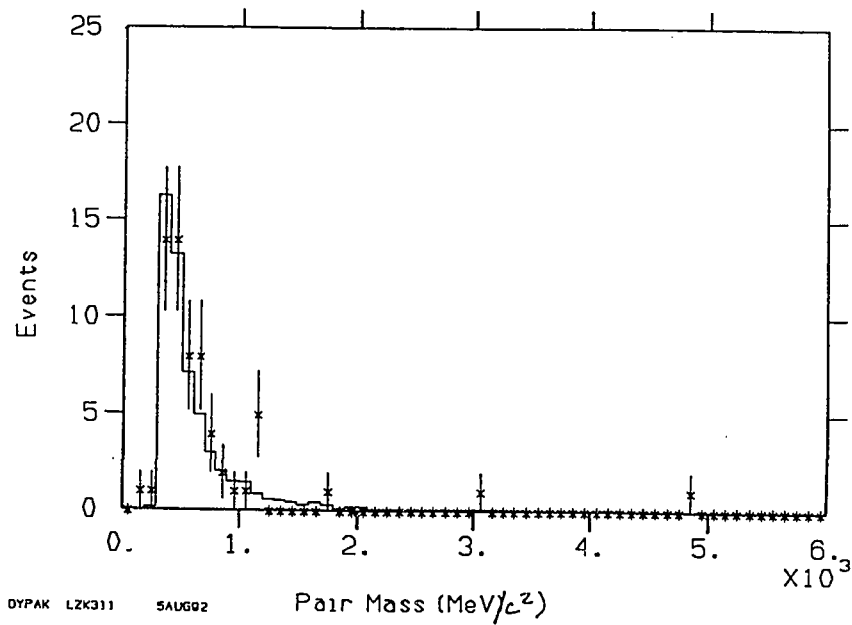


Figure 64: Invariant pair mass distribution for 1989 data (points). Histogram is the theoretical prediction from Monte Carlo.

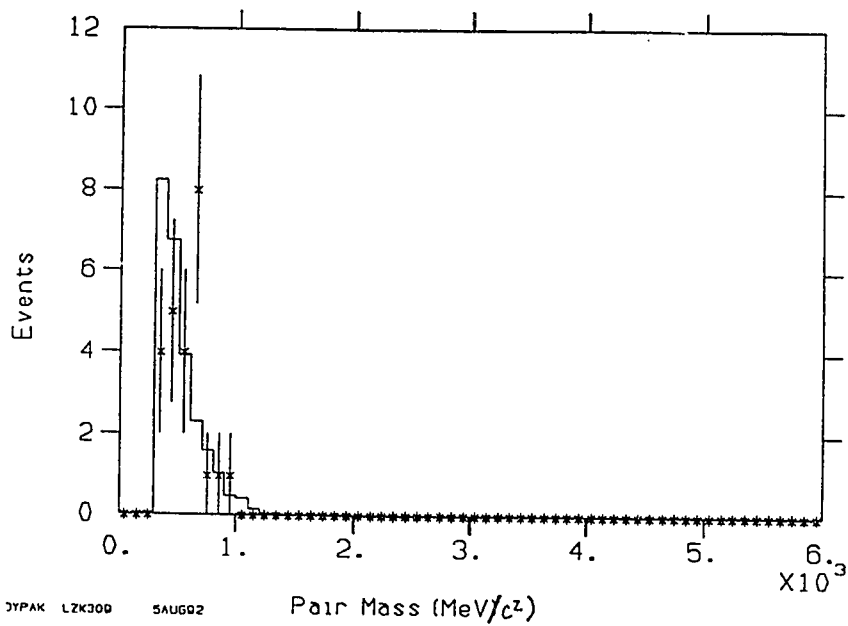


Figure 65: Invariant pair mass distribution for 1990 data (points). Histogram is the theoretical prediction from Monte Carlo.

The measurement is shown to be in agreement with the theoretical prediction from QED. For this analysis, the observed electron and positron are required to have an invariant pair mass greater than $300 \text{ MeV}/c^2$. For integrated luminosities of 19.7 nb^{-1} and 10.1 nb^{-1} in the Mark II data runs at the SLC, $62 \pm 7.9 \pm 6.0 -3.1$ and $24 \pm 4.9 \pm 2.7 -5.0$ are observed in the respective runs (the first error is statistical, the second is systematic, and the third is the background events). Given the statistics, these are in agreement with the 76.9 ± 1.4 and 25.3 ± 0.7 events predicted by Monte Carlo.

Chapter 7

Conclusions

For integrated luminosities of 19.7 nb^{-1} and 10.1 nb^{-1} in the Mark II data runs at the SLC, $62 \pm 7.9 \pm 6.0 -3.1$ and $24 \pm 4.9 \pm 2.7 -5.0$ events from the untagged two-photon process $e^+e^- \rightarrow e^+e^-e^+e^-$ are observed in the data. The first error is statistical and the second is systematic. Given the statistics, this measurement is consistent with the QED theoretical prediction. More statistics would greatly improve not only the statistical error, but also the systematic error. The largest systematic error arises from the error on the integrated luminosities. Increasing the Bhabha events for the luminosity measurements would decrease this portion of the systematic error. Also, if there were more statistics to begin with, a higher p_t cut ($p_t > 2 \text{ GeV}$) might be used to decrease the systematic error from the momentum resolution to the three to five percent level.

Higher integrated luminosities would also allow for the study of those two-photon processes with smaller cross sections: $e^+e^- \rightarrow e^+e^-\tau^+\tau^-$, $e^+e^- \rightarrow l^+l^-l^+l^-$ where $l = \mu$ or $l = \tau$, and $e^+e^- \rightarrow e^+e^-q\bar{q}$ where q is the bottom quark. The $e^+e^- \rightarrow \mu^+\mu^-\mu^+\mu^-$ cross section has been observed only in the CELLO [37], Mark II, and

HRS detectors [38]. At LEP, where the integrated luminosities are high, the four LEP collaborations have studied the reaction $e^+e^- \rightarrow \gamma\gamma$ directly [39, 40, 42, 41] and have observed good agreement with QED; however, studies on the processes listed above may still prove to be worthwhile. Evidence has been presented for an anomalously large cross section for charm quarks (inclusive D^* mesons) by TASSO [43], but was not confirmed by CELLO [44] or TPC/ $\gamma\gamma$ [45]. The collaborations at TRISTAN (AMY and TOPAZ) have studied the $e^+e^- \rightarrow e^+e^-\mu^+\mu^-$ at center-of-mass energies from 52 GeV to 61.4 GeV and these first results are shown to be in agreement with QED [4, 46]. However, the processes listed above are still untapped areas, and the possibility of something unexpected occurring is not at all remote.

Appendix A

Experimental Acceptance Function

A study of the influence of experimental constraints on the two-prong final states of two-photon processes has been done by A. Courau [8]. The procedure is outlined here for the case $e^+e^- \rightarrow e^+e^-e^+e^-$ for relativistic electrons. In this limit, the differential cross section is given by

$$\frac{d^2\sigma}{dWd\beta} \sim \frac{1}{1-\beta^2} \frac{1}{W^3} \ln^2\left(\frac{E_b}{m_e}\right) \ln\left(\frac{W}{2m_e}\right) \quad (105)$$

or equivalently,

$$\frac{d^2\sigma}{dWdy} \sim \frac{1}{W^3} \ln^2\left(\frac{E_b}{m_e}\right) \ln\left(\frac{W}{2m_e}\right) \quad (106)$$

where W is the final state e^+e^- invariant mass, β is the velocity of the pair in the lab frame, and y is the rapidity of the pair in the lab frame.

Integrating over the whole phase space ($0 < \beta < \frac{4E_b^2 - W^2}{4E_b^2 + W^2}$ or $0 < y < \ln[\frac{2E_b}{W}]$), to find the total cross section gives

$$\sigma_{tot} \sim \frac{1}{4m_e^2} \ln^3\left(\frac{E_b}{m_e}\right) \quad (107)$$

as discussed in Section 4.5 (compare Equation 95, with $l = e$).

However, the central detector may have a limited acceptance in the polar angle of either of the final state electron: $\psi \leq \theta \leq \pi - \psi$, where ψ is the polar angle cut-off. This means that there is an acceptance function for β (or y) which depends on ψ ; it decreases as β increases, and becomes zero for $\beta \geq \cos \psi$ (or $y \geq \ln[\cot \psi/2]$). For the pair production of two relativistic bodies, when Ω_L is the acceptance in the laboratory (defined by $0 \leq \phi \leq 2\pi$, $\psi \leq \theta \leq \pi - \psi$), and β is the velocity of the pair in the laboratory ($\vec{\beta}$ being parallel to the incident directions which define the ψ angle), the acceptance function, ε , is given by

$$\varepsilon = \frac{1}{\sigma} \int_{\Omega_L} \frac{d\sigma}{d\Omega} = \frac{2}{\sigma} \int_0^{x_0} \frac{d\sigma}{dx} dx \quad (108)$$

where $x = \cos \theta^*$ (θ^* is the polar angle of the particles in their center-of-mass system) and the upper limit, x_0 is given by

$$x_0 = \frac{\cos \psi - \beta}{1 - \beta \cos \psi} \quad (109)$$

(this arises from the condition $\beta \leq \cos \psi$).

For relativistic lepton pair production, where $\cos \psi < 1$ (implying that $x_0 < 1$), an ε can be defined by the expression

$$\int_{\Omega_L} \frac{d\sigma}{d\Omega} = \frac{2\pi\alpha^2}{W^2} \varepsilon. \quad (110)$$

Here, ε is not the acceptance as defined before (because the total cross section is not $2\pi\alpha^2/W^2$), but contains an additional W dependence when integrated up to $x = 1$. However, this additional dependence disappears for relativistic particles when integrated up to x_0 (< 1). Integration gives

$$\varepsilon(\beta, \psi) = 2 \int_0^{x_0} \frac{1+x^2}{1-x^2} dx = 2(\ln[\frac{1+x_0}{1-x_0}] - x_0) \quad (111)$$

with $\beta \leq \beta_{max}$; $\beta_{max} = \cos \psi$.

Integrating by the rapidity y , instead of the velocity β ($\beta = \tanh y$) gives

$$\varepsilon(y, \psi) = 4(y_{max} - y) - 2 \tanh(y_{max} - y) \quad (112)$$

with $y \leq y_{max}$; $y_{max} = -\ln(\tan \psi/2)$.

Combining this expression for ε with the factor $d\beta/(1 - \beta^2)$ in the cross section, and integrating over β gives

$$\int_0^{\beta_{max}} \varepsilon(\beta, \psi) \frac{d\beta}{1 - \beta^2} = \int_0^{y_{max}} \varepsilon(y, \psi) dy \quad (113)$$

$$= 2\{\ln^2[\tan(\psi/2)] + \ln(\sin \psi)\} \equiv f(\psi) \quad (114)$$

(Another factor of 2 appears due to the symmetry of the velocity range ($0 \leq \beta \leq \cos \psi$) with respect to the beam directions). Upon integrating over W , the total cross section becomes

$$\sigma = \int_{W_0}^{2E_b} f(\psi) \frac{dW}{W^3} \quad (115)$$

$$\sim f(\psi) \frac{1}{W_0^2} \quad (116)$$

where W_0 is the effective mass threshold for observing the final pair in the detector. This threshold is usually set by the trigger of the detector; typically, the detector is set to trigger on tracks with momenta greater than a momentum p_0 . This gives an effective mass threshold of $W_0 \geq 2\sqrt{p_0^2 + m_e^2} \gg 2m_e$.

Bibliography

- [1] F.A. Berends, P.A. Daverveldt and R. Kleiss, *Comp. Phys. Comm.* 40 (1986) 285.
F.A. Berends, P.A. Daverveldt and R. Kleiss, *Nucl. Phys.* B253 (1985) 441.
F.A. Berends, P.A. Daverveldt and R. Kleiss, *Phys. Lett.* B148 (1984) 489.
- [2] M. Perl, SLAC-PUB-4165, December 1986.
- [3] Mark J Collaboration, DESY-85-073 (1985)
JADE Collaboration, *Z Phys.* C30 (1986) 545
ASP Collaboration, SLAC-337 (1989).
- [4] S. K. Kim, *et al.*, *Phys. Lett.* B223 (1989) 476.
- [5] J.D. Bjorken and S.D. Drell, *Relativistic Quantum Mechanics*, McGraw-Hill (1964).
- [6] F. Mandl and G. Shaw, *Quantum Field Theory*, J. Wiley and Sons (1984).
- [7] S. Brodsky, T. Kinoshita, and H. Terazawa, *Phys. Rev.* D4 (1971) 1532.
- [8] A. Courau, "Production of Lepton Pairs in $\gamma\gamma$ Collisions", *Proceedings of the Fourth International Colloquium on Photon-Photon Interactions*, ed. G.W. London, World Scientific, Singapore (1981).

- [9] F. Dydak, CERN-PPE/91-14, January 1991.
- [10] R.N. Cahn, Phys. Rev. D36 (1987) 2666.
- [11] C. Quigg, *Gauge Theories of the Strong, Weak, and Electromagnetic Interactions*, The Benjamin/Cummings Publishing Company (1983).
- [12] B. Richter *et al.*, SLAC-PUB-4367, *1987 Lepton and Photon Symposium*. SLAC-229, *Conceptual SLC Design Report*, June 1980.
- [13] G. S. Abrams *et al.*, Nucl. Instr. and Meth. A281 (1989) 55.
- [14] G. Bowden *et al.*, Nucl. Instr. and Meth. A278 (1989) 664.
- [15] L. Labarga *et al.*, SLAC-PUB-5158, December 1989.
- [16] J. P. Alexander *et al.*, Nucl. Instr. and Meth. A283 (1989) 519.
- [17] D. Durrett *et al.*, SLAC-PUB-5259, May 1990.
- [18] D. Bernstein *et al.*, IEEE Trans. Nucl. Sci. NS-33 (1986) 86.
- [19] J. Perl *et al.*, Nucl. Instr. and Meth. A252 (1986) 616.
- [20] D. Schaile *et al.*, Nucl. Instr. and Meth. A242 (1986) 247.
- [21] E. Soderstrom, Ph.D. Thesis, RX-1322 (CAL-TECH), October 1990, 80.
- [22] M. Petradza *et al.*, Mark II-SLC Note #164 (1989), unpublished.
- [23] J. Nash, Ph.D. Thesis, SLAC-356 January 1990, 63.
- [24] R. Aleksan *et al.*, *Proceedings of the International Conference on the Impact of Digital Microelectronics and Microprocessors on Particle Physics*, World Scientific (1988) 38.

- [25] H. Brafman, *et al.*, SLAC-PUB-2033, October 1977
T. Himel, Ph.D. Thesis, SLAC-223, October 1979.
- [26] D.J. Nelson, *et al.*, IEEE Trans. Nucl. Sci. NS-28 (1981) 336.
- [27] J. Kent, *et al.*, SLAC-PUB-4922, March 1989
M. Levi, *et al.*, SLAC-PUB-5110, March 1989
- [28] R.J. VanKooten, Ph.D. Thesis, SLAC-367 June 1990, 44.
- [29] Ch. Berger and W. Wagner, Phys. Rep. 136 (1987) 1.
- [30] H. Euler and B. Kockel, Naturwissenschaften 23 (1935) 246.
- [31] L. Landau and E. Lifshitz, Phys. Z. Soviet Union 6 (1934) 244.
- [32] E.J. Williams, Det Kgl. Danske Videnskab. Selskab. Mat.-Fys. M ed. XIII (1935)
4.
- [33] H. Kolanoski and P. Zerwas, "Two-Photon Physics", *High Energy Electron-Positron Physics*, eds. A. Ali and P. Söding, World Scientific, Singapore (1988).
- [34] V.M. Budnev *et al.*, Phys. Rep. 15 (1975) 181.
- [35] H. Kolanoski, *Two-Photon Physics at e^+e^- Storage Rings*, Springer-Verlag (1984).
- [36] G. Feldman *ed.*, *Proceedings of the Third Mark II Workshop on SLC Physics*, SLAC-Report-315, July 1987, 1.
- [37] CELLO Collab., Z. Phys. C43 (1989) 1.
- [38] A. Petradza, *et al.*, Phys. Rev. D42 (1990) 2180.

- [39] ALEPH Collab., D. Decamp, *et al.*, CERN-PPE/91-149 (1991).
- [40] DELPHI Collab., P. Abreu *et al.*, Phys. Lett B268 (1991) 296.
- [41] OPAL Collab., M. Akrawy *et al.*, Phys. Lett B257 (1991) 531.
- [42] L3 Collab., B. Adeva *et al.*, Phys. Lett. B250 (1990) 183.
- [43] TASSO Collab., Z. Phys. C47 (1990) 499.
- [44] H.J.Behrend *et al.*, Z. Phys. C51 (1991) 365.
- [45] M. Alston-Garnjost *et al.*, Phys. Lett. B252 (1990) 499.
- [46] TOPAZ Collab., Phys. Lett. B279 (1992) 422.
- [47] F. Halzen and A.D. Martin, *Quarks and Leptons*, J. Wiley and Sons (1984).